

**DEVELOPMENT AND CHARACTERIZATION OF  
METAL INJECTION MOULDED COMPONENTS  
IN IMPROVING RESISTANCE TO HIGH-  
TEMPERATURE WEAR AND  
OXIDATION**

Thesis

Submitted in partial fulfilment of the requirements for the degree of

**DOCTOR OF PHILOSOPHY**

by

**VEERESH NAYAK C**



DEPARTMENT OF MECHANICAL ENGINEERING  
NATIONAL INSTITUTE OF TECHNOLOGY KARNATAKA,  
SURATHKAL, MANGALORE – 575025

DECEMBER, 2018



## DECLARATION

I hereby declare that the Research Thesis entitled “**Development and Characterization of Metal Injection Moulded Components in Improving Resistance to High Temperature Wear and Oxidation**” which is being submitted to the **National Institute of Technology Karnataka, Surathkal** in partial fulfilment of the requirements for the award of the Degree of **Doctor of Philosophy in Mechanical Engineering** is a *bonafide report of the research work carried out by me*. The material contained in this Research Thesis has not been submitted to any other Universities or Institutes for the award of any degree.

Register Number: **138006ME13F17**

Name of the Research Scholar: **VEERESH NAYAK C**

Signature of the Research Scholar:

Department of Mechanical Engineering

Place: NITK-Surathkal

Date:

## **CERTIFICATE**

This is to certify that the Research Thesis entitled “**Development and Characterization of Metal Injection Moulded Components in Improving Resistance to High Temperature Wear and Oxidation**” submitted by **Mr. VEERESH NAYAK C. (Register Number: 138006ME13F17)** as the record of the research work carried out by him, *is accepted as the Research Thesis submission* in partial fulfilment of the requirements for the award of the Degree of **Doctor of Philosophy.**

### **Research Guides**

**Dr. M. R. Ramesh**

Research Guide

**Prof. Vijay Desai**

Research Co-Guide

**Chairman – DRPC**

**Date:**

## ACKNOWLEDGEMENTS

It is my great pleasure to express my heartfelt gratitude to my research supervisors **Dr. M. R. Ramesh**, Associate Professor and **Prof. Vijay Desai**, Professor Department of Mechanical Engineering, National Institute of Technology Karnataka, Surathkal, Mangalore, for their exemplary guidance and encouragement throughout my research work. Their encouragement and valuable suggestions have increased my knowledge level which led to the completion of my research work and is demonstrated through this thesis.

The author wishes to record his deep sense of gratitude to **Prof. Narendranath S**, The Head, Department of Mechanical Engineering and all the faculty members, technical and administrative staffs of the Mechanical Engineering, National Institute of Technology Karnataka, Surathkal for their help, as and when needed.

The author is highly thankful to **Prof. Prasad Krishna**, **Prof. Gangadharan K V**, Department of Mechanical Engineering, **Prof. K Rajendra Udupa**, **Dr. Udaya Bhat K**, The Head, Department of Metallurgical, and Materials Engineering. The author wishes to record his deep sense of gratitude to **Dr. Sudip Kumar Samanta** Principal Scientist, CSIR -Central Mechanical Engineering Research Institute for his support and interaction in extending metal injection moulding facility. **Dr. Nagahanumaiah** Director, Central Manufacturing Technology Institute (CMTI) Bangalore for his support and interaction during experimentation. The author wishes to record his deep sense of gratitude to **Dr. N Balashanmugam** Joint Director, Central Manufacturing Technology Institute (CMTI) Bangalore, for his support and interaction in extending characterization facility.

The author is highly obliged to **Prof. Katta Venkataramana**, professor Dept. of Civil Engineering, National Institute of Technology Karnataka, Surathkal. A deep sense of gratitude is acknowledged to **Mr. T K Rathod** Instructor, Govt. Tool Room and Training centre Kanakapura, **Mr Prakash Sarangamath**, GT&TC Kudalasangama. Instructors and friends from Govt. Tool Room and Training centre Kudalasangama, who was kind enough to encourage pursuing Ph.D.

The author is highly thankful to RPAC members **Dr. Suresha S N**, Dept. of Civil Engineering and **Dr. D Chakradhar, Prof. Prasad Krishna** Dept. of Mechanical Engineering and DRPC members **Dr. Sathyabhama A, Dr. Gnanasekaran Dr. Sharnappa Joladarashi, Dr.Ranjith M and Dr. Jeyaraj P** Dept. of Mechanical Engineering.

The author wishes to thank his seniors Dr. Manjunath Patel, Dr. Muralidhar Avvari, Dr. Manjaiah M, Dr. Arun Kumar Shettigar, Dr. Raghavendra, Dr. Vignesh, Dr. Shivaprasad for their constant help and encouragement during the entire process of this research work. Author also wishes to thank his friends especially to Dr. Gajanan Anne Mr.Nithin H S, Dr.Gopi K R, Dr. Mahantayya Matapathi, Dr. Jayavardhana, Mr.Prashantha B, Mr. Thippeswamy, Dr.Venkataesh Lambani, Mr. Ramesh Babu, Mr. Ashrith H. S, Mr. Pradeep V Badiger, Dr. Hargovind Soni, Dr. Hemanth K, Mr.Vasu, Dr.Suhas, Mr.Anil Kadam, Mr.Mallikarjun, Mr.Rakesh R, Mr.Madagonda B, Mr.Parashuram C, Mr.Praveen, Mr.Ramesh, Dr.Madhusudhan, Ms. Pooja Mr.Shivram. Mr. Sangamesh Mr. Abdulrajak Buradi Mr. Durgaprasad, Mr.Subba Rao, Mr.Suresh, Mr. Vinay Varghese, and all the research scholars of Dept. of Mechanical and Metallurgical and Materials Engineering for their everlasting support.

I am thankful to my Son Keerthan Nayak C whose smiling face is the main source of inspiration during the execution of this work. I am also thankful to my wife Asha for her moral support, inspiration, and patience during a tough period. I am really thankful Mr.R Bheemayya Nayak and Rajoli family for their moral support and encouragement to start this research. At this stage of life, I am deeply indebted to my parents late. Bheemaraya Nayak C and Mrs. Bhimakka who stood by my side all the time. I am also thankful to my family members Anjaneya Nayak C, Pranavi, Thirumal Nayak C, Virupakshamma, Dullaya, Karthik Nayak K Without their strong support it would be impossible for me to transform my dream into reality. Finally, it is my great pleasure to complete this acknowledgement with the love and support received from my father-in-law Mr. Gurudath and mother-in-law Mrs. Laxmi.

*(VEERESH NAYAK C)*

## ABSTRACT

Metal injection moulding (MIM) is a near-net shape manufacturing technology for producing intricate parts, cost-effectively. MIM comprises combined techniques of plastic injection moulding and powder metallurgy. A wax-based binder system consisting of paraffin wax (PW), low-density polyethylene (LDPE), polyethylene glycol (PEG-600) and stearic acid is established for MIM of powder systems of Cr<sub>3</sub>C<sub>2</sub>-NiCr (30% Wt.) +NiCrSiB (70% Wt.), SS316L (70% Wt.) +WC-CrC-Ni (30% Wt.) and Tool Steel. The excellence of the MIM product depends on feedstock characteristics, process parameters of the injection moulding stage as well as debinding and sintering stage. Injection stage is most important as many defects such as phase separation, weld line, voids etc. may occur during injection stage due to improper selection of injection moulding parameters and these defects cannot be repaired in the subsequent debinding and sintering stages. The feedstock was characterized by rheological properties at different temperatures. Injection temperature was determined by the rheological investigation of the feedstock having the 56 % powder loading and 44% binder by volume. The solvent debinding temperature is optimized and defect-free MIM component is obtained at a temperature of 48°C. Sintering process was carried out with the temperature cycle in the range of 1150–1200 °C under hydrogen purged atmosphere. The sintering density achieved was 96%. The MIM components showed good and acceptable shrinkage in linear dimensions.

Material behaviour at elevated temperature is becoming an increasing technological importance. Components working at higher temperatures like in land-based gas turbines, power generation boiler tubes, hot sections of aero engine, gas and steam turbine, propulsion bearings, materials processing, and internal combustion engines are subjected to surface friction, wear, oxidation conditions. Service conditions of such components in elevated temperature environments may compromise their mechanical properties resulting in a reduced life cycle. Components working in such adverse conditions demand suitable components processed through near net shape techniques. The proposed MIM compacts are investigated for their resistance to wear and oxidation under laboratory conditions.

Three types of MIM specimens namely Cr<sub>3</sub>C<sub>2</sub>-NiCr+NiCrSiB, SS316L+WC-CrC-Ni, and Tool Steel are characterized using Scanning Electron Microscope (SEM), Energy Dispersive Spectroscopy (EDS) and X-ray diffraction (XRD). Further, microstructure and mechanical properties were characterized to evaluate their potential for high-temperature application.

Dry sliding wear behaviour of MIM specimens are evaluated using a high-temperature pin on disc tribometer. The SS316L+WC-CrC-Ni and Tool Steel MIM specimens displayed a lower coefficient of friction and wear rate in comparison with Cr<sub>3</sub>C<sub>2</sub>-NiCr+NiCrSiB. Excellent wear resistance of the MIM specimens is attributed to the solid lubricants effect. Based on the wear rate data, the relative wear resistance of the MIM specimens under dry sliding conditions is arranged in the following sequence:

$$(\text{Tool Steel}) > (\text{SS316L+WC-CrC-Ni}) > (\text{Cr}_3\text{C}_2\text{-NiCr+NiCrSiB})$$

Higher wear resistance of MIM Tool Steel specimens is attributed to the high hardness of Cr<sub>3</sub>Ni<sub>2</sub> phase formed during the sintering process.

Thermo cyclic oxidation behaviour of MIM specimens was carried out at 700 °C for 20 cycles. Each cycle consisted of heating at 700 °C for 1 hour, followed by 20 minutes of cooling in the air. The thermogravimetric technique is used to approximate the oxidation kinetics of MIM specimens. The Cr<sub>3</sub>C<sub>2</sub>-NiCr+NiCrSiB and SS316L+WC-CrC-Ni MIM specimens reported lower weight gain as compared to the Tool steel. Cr<sub>3</sub>C<sub>2</sub>-NiCr+NiCrSiB MIM specimens registered less weight gain as compared to SS316L+WC-CrC-Ni which is attributed to the excellent oxidation resistance of NiCrSiB and formation of NiCrO<sub>4</sub> along with NiO and Cr<sub>2</sub>O<sub>3</sub> oxides on the surface of MIM specimens.

In the present study, the powders of Cr<sub>3</sub>C<sub>2</sub>-NiCr+NiCrSiB, SS316L+WC-CrC-Ni, and Tool Steel are successfully metal injection moulded and sintered to achieve 96% density. Developed MIM components exhibit resistance to high-temperature wear and oxidation which is suitable for components subjected to elevated temperature service conditions.

**Keywords:** *Metal injection moulding; Binder; Debinding; Sintering; Oxidation; Wear; Elevated temperature.*



## TABLE OF CONTENTS

<b>DECLARATION</b> .....	<b>i</b>
<b>CERTIFICATE</b> .....	<b>ii</b>
<b>Acknowledgements</b> .....	<b>iii</b>
<b>ABSTRACT</b> .....	<b>v</b>
<b>TABLE OF CONTENTS</b> .....	<b>vii</b>
<b>LIST OF TABLES</b> .....	<b>xi</b>
<b>LIST OF FIGURES</b> .....	<b>xiii</b>
<b>NOMENCLATURE</b> .....	<b>xix</b>
<b>1. INTRODUCTION</b> .....	<b>1</b>
1.1 LITERATURE SURVEY .....	4
1.2 Powder, binder and feedstock attributes .....	8
1.3 Powder particle shape and size .....	9
1.4 Selection of Binders .....	10
1.5 Moulding Tool for MIM .....	16
1.6 Injection moulding stage of MIM .....	18
1.7 Debinding stage of MIM.....	20
1.8 Sintering stage of MIM.....	22
1.9 Problems and defects related to the injection stage of MIM .....	26
1.10 Summary .....	28
1.11 Objectives of the research work.....	28
1.12 Organization of the thesis .....	29
<b>2 EXPERIMENTATION</b> .....	<b>31</b>
2.1 Powder particle size and Shape.....	31
2.2 Feedstock preparation .....	31
2.3 DSC studies of feedstock .....	34
2.4 Viscosity of feedstock.....	34
2.5 Thermogravimetry analysis (TGA) of binder and feedstock.....	35

2.6	Injection moulding .....	35
2.7	Debinding MIM samples .....	37
2.8	Conventional Sintering .....	37
2.9	Microwave sintering .....	38
2.10	Density measurement of the feedstock powder .....	39
2.11	Density measurement of sintered compact .....	40
2.12	Microstructural characterization .....	40
2.13	Phase analysis using X-ray diffractometer (XRD) .....	42
2.14	Microhardness of sintered MIM composites .....	43
2.15	Tensile strength test .....	44
2.16	Cyclic oxidation test .....	44
2.17	Sliding wear test.....	45
2.18	Summary .....	46
<b>3</b>	<b>RESULTS AND DISCUSSION .....</b>	<b>47</b>
3.1	Particle size and shape .....	47
3.2	Viscosity of Feedstock .....	50
3.3	Differential scanning calorimetry (DSC).....	53
3.4	Thermogravimetric analysis (TGA).....	56
3.5	Measurement of density of the feedstock .....	58
3.6	Debinding.....	59
3.7	Conventional Sintering .....	66
3.8	Microwave sintering of MIM specimen .....	68
3.9	Density, Microhardness and Tensile Strength .....	70
3.10	Wear Behaviour of Sintered MIM compacts .....	72
3.10.1	Cr <sub>3</sub> C <sub>2</sub> -NiCr+NiCrSiB.....	72
3.10.2	SS316L+WC-CrC -Ni.....	78
3.10.3	Tool Steel.....	83
3.11	Oxidation Studies.....	88
3.11.1	Visual observations .....	88
3.11.2	Thermogravimetric behaviour .....	89
3.11.3	XRD analysis .....	91

3.11.4	cross-sectional and Surface analysis of scale.....	93
3.12	Summary .....	99
<b>4</b>	<b>CONCLUSIONS .....</b>	<b>101</b>
	<b>FUTURE WORK.....</b>	<b>103</b>
	<b>REFERENCES.....</b>	<b>105</b>
	<b>LIST OF PUBLICATIONS AND CONFERENCES .....</b>	<b>117</b>
	<b>BIO-DATA.....</b>	<b>121</b>



## LIST OF TABLES

Table 1.1 Different binder systems for MIM feedstock .....	12
Table 1.2 Debinding methods used for MIM feedstock .....	13
Table 2.1 Material system chemical composition.....	31
Table 2.2 The binder composition .....	32
Table 2.3 Feedstock composition for material system SS316L+WC-CrC-Ni.....	32
Table 2.4 Composition of the feedstock for material system NiCrSiB+ Cr <sub>3</sub> C <sub>2</sub> -NiCr .	33
Table 2.5 Feedstock composition of Tool Steel.....	33
Table 3.1 Particle size distributions in (μm).....	49
Table 3.2 Density measurement of binder and feedstock .....	59
Table 3.3 Mechanical properties of the Conventional sintered MIM specimens .....	71
Table 3.4 Linear shrinkage of conventional sintered MIM samples .....	72



## LIST OF FIGURES

Figure 1.1 Different processes cost vs. the shape complexity (Kong 2013).....	4
Figure 1.2 Schematic representation of MIM process (Sidambe 2014) .....	6
Figure 1.3 Powder-binder mixture .....	9
Figure 1.4 Viscosity of typical PIM feedstock .....	16
Figure 1.5 Schematic diagram of an injection mould for MIM.....	17
Figure 1.6 Schematic diagram of an Injection moulding.....	19
Figure 1.7 Removal of binder through the pores during thermal debinding by saturation .....	22
Figure 1.8 Powder particle sintering a) two particles are in point contact before sintering, b) particles bound together by neck formation during sintering.....	23
Figure 1.9 Mass transport mechanism during sintering.....	23
Figure 1.10 Microstructure of the compact at various stages of sintering (a) debound stage (b) Initial stage (c) intermediate stage (d) final stage .....	25
Figure 2.1 Binders for preparation of the feedstock .....	32
Figure 2.2 Sigma blade mixer a)Sigma blade mixer with temperature unit b) Mixing chamber.....	33
Figure 2.3 Rotational rheometer a) open chamber b) plate .....	34
Figure 2.4 Injection mould inserts with a) Reference part & parting Surface b) cavity, c) wireframe model of the core cavity .....	35
Figure 2.5 Injection mould used for fabrication. ....	36
Figure 2.6 Debinding furnace a) Drying oven b) Thermal debinding furnace .....	37
Figure 2.7 Sintering furnace .....	38
Figure 2.8 Experimental setup of microwave sintering furnace a) Line diagram b) Microwave furnace .....	39

Figure 2.9 Pycnometer .....	40
Figure 2.10 Optical microscope.....	41
Figure 2.11 Scanning electron microscope.....	42
Figure 2.12 X-ray diffraction.....	43
Figure 2.13 Microhardness testing machine.....	43
Figure 2.14 Tensometer .....	44
Figure 2.15 Tubular furnace.....	45
Figure 2.16 (a) Pin on disc tribometer setup (b) schematic representation of the test setup.....	46
Figure 3.1 Metal particle distribution graph a) SS316L ,b) WC-CrC-Ni, c) Cr <sub>3</sub> C <sub>2</sub> -NiCr, d)Tool Steel e) NiCrSiB.....	48
Figure 3.2 SEM micrograph of powder material system 1 a) Cr <sub>3</sub> C <sub>2</sub> -NiCr b) NiCrSiB c) Cr <sub>3</sub> C <sub>2</sub> -NiCr + NiCrSiB.....	49
Figure 3.3 SEM micrograph of powder material system 2 a) SS316L b) WC-CrC-Ni c) SS316L + WC-CrC-Ni .....	50
Figure 3.4 SEM micrograph of powder material system 3 a) Tool Steel .....	50
Figure 3.5 The relation between the viscosity of SS316L+WC-CrC-Ni feedstock and shear rate.....	51
Figure 3.6 The relation between the viscosity of Cr <sub>3</sub> C <sub>2</sub> -NiCr+NiCrSiB feedstock and shear rate.....	52
Figure 3.7 The relation between the viscosity of Tool Steel T-15feedstock and shear rate.....	53
Figure 3.8 DSC plots for the binder.....	54
Figure 3.9 DSC plots for Cr <sub>3</sub> C <sub>2</sub> -NiCr+NiCrSiB feedstock.....	54
Figure 3.10 DSC plots for SS316L+WC-CrC-Ni Feedstock.....	55
Figure 3.11 DSC plots for Tool Steel T-15 Feedstock .....	55



Figure 3.12 TGA Curves for Cr <sub>3</sub> C <sub>2</sub> -NiCr+NiCrSiB feedstock.....	57
Figure 3.13 TGA Curves for SS316L+WC-CrC-Ni feedstock.....	58
Figure 3.14 TGA Curves for tool steel feedstock.....	58
Figure 3.15 Effect of debinding temperature on the weight loss of MIM compact immersed in n-hexane for various extractive times. ....	60
Figure 3.16 Shows the cracks and sagging on compact after debinding. ....	60
Figure 3.17 Defect-free solvent debonded compact at 48° C. ....	61
Figure 3.18 Micrograph of injection moulded green compact before debinding. ....	61
Figure 3.19 SEM Micrograph of the green compact after solvent debinding at 48 °C for 5 hours.....	62
Figure 3.20 shows the SEM Micrograph of a specimen after thermal debinding. a) SS316L+WC-CrC-Ni b)Cr <sub>3</sub> C <sub>2</sub> -NiCr+NiCrSiB c) Tool Steel –T 15 .....	63
Figure 3.21 Weight reduction of green compact during thermal debinding at different temperatures.....	64
Figure 3.22 Weight reduction of green compact during thermal debinding at a different holding period.....	65
Figure 3.23 Thermal debinding cycle.....	65
Figure 3.24 Photograph of thermal debound specimen.....	66
Figure 3.25 Sintering cycle.....	67
Figure 3.26 Tensile specimen sintered at 1200 °C.....	67
Figure 3.27 Micrograph of the conventionally sintered specimen a) SS316L+WC-CrC-Ni b)Cr <sub>3</sub> C <sub>2</sub> -NiCr+NiCrSiB c) Tool Steel T-15.....	68
Figure 3.28 Micrograph of the microwave sintered specimen a) SS316L+WC-CrC-Ni b)Cr <sub>3</sub> C <sub>2</sub> -NiCr+NiCrSiB c) Tool Steel T-15.....	69
Figure 3.29 Microhardness indentation on a) SS316L+WC-CrC-Ni b) Cr <sub>3</sub> C <sub>2</sub> -NiCr+NiCrSiB, c) Tool Steel –T 15 .....	70

Figure 3.30 (a) Plot of friction coefficient with sliding distance at room temperature and SEM of worn surface of the Cr<sub>3</sub>C<sub>2</sub>-NiCr+NiCrSiB composite specimen at room temperature under varying loads of (b) 10 N and (c) 30 N (d) 40 N ..... 73

Figure 3.31 (a) Plot of friction coefficient with sliding distance at 200°C and SEM of worn surface of the Cr<sub>3</sub>C<sub>2</sub>-NiCr+NiCrSiB composite specimen at 200°C under varying loads of (b) 10 N and (c) 30 N (d) 40 N..... 74

Figure 3.32 (a) Plot of friction coefficient with sliding distance at 400 °C and SEM of worn surface of the Cr<sub>3</sub>C<sub>2</sub>-NiCr+NiCrSiB composite specimen at 400 °C under varying loads of (b) 10 N and (c) 30 N (d) 40 N..... 74

Figure 3.33 (a) Plot of friction coefficient with sliding distance at 600 °C and SEM of worn surface of the Cr<sub>3</sub>C<sub>2</sub>-NiCr+NiCrSiB composite specimen at 600 °C under varying loads of (b) 10 N and (c) 30 N (d) 40 N..... 75

Figure 3.34 XRD pattern of the worn surface of Cr<sub>3</sub>C<sub>2</sub>-NiCr+NiCrSiB at a) room temperature, b) 400 and c) 600 °C. .... 76

Figure 3.35 Frictional coefficient and wear rate of Cr<sub>3</sub>C<sub>2</sub>-NiCr+NiCrSiB (a) Frictional coefficient v/s Temperature (b) Wear rate v/s Temperature ..... 77

Figure 3.36 (a) Plot of friction coefficient with sliding distance at room temperature and SEM of worn surface of the SS316L+WC CrC-Ni composite specimen at room temperature under varying loads of (b) 10 N and (c) 30 N (d) 40 N ..... 79

Figure 3.37 (a) Plot of friction coefficient with sliding distance at 200°C and SEM of worn surface of the SS316L+WC CrC-Ni composite specimen at 200°C under varying loads of (b) 10 N and (c) 30 N (d) 40 N..... 79

Figure 3.38 (a) Plot of friction coefficient with sliding distance at 400°C and SEM of worn surface of the SS316L+WC CrC-Ni composite specimen at 400°C under varying loads of (b) 10 N and (c) 30 N (d) 40 N..... 80

Figure 3.39 (a) Plot of friction coefficient with sliding distance at 600°C and SEM of worn surface of the SS316L+WC CrC-Ni composite specimen at 600°C under varying loads of (b) 10 N and (c) 30 N (d) 40 N..... 80

Figure 3.40 XRD pattern of the worn surface of SS316L+WC-CrC-Ni at a) room temperature, b) 400 and c) 600 °C.....	81
Figure 3.41 Frictional coefficient and wear rate of SS316L+WC-CrC-Ni with (a) Frictional coefficient v/s Temperature (b) Wear rate v/s Temperature .....	82
Figure 3.42 (a) Plot of friction coefficient with sliding distance at room temperature and SEM of worn surface of the Tool Steel specimen at room temperature under varying loads of (b) 10 N and (c) 30 N (d) 40 N.....	84
Figure 3.43 (a) Plot of friction coefficient with sliding distance at 200 °C and SEM of worn surface of the Tool Steel specimen at 200 °C under varying loads of (b) 10 N and (c) 30 N (d) 40 N.....	84
Figure 3.44 (a) Plot of friction coefficient with sliding distance at 400 °C and SEM of worn surface of the Tool Steel specimen at 400 °C under varying loads of (b) 10 N and (c) 30 N (d) 40 N.....	85
Figure 3.45 (a) Plot of friction coefficient with sliding distance at 600 °C and SEM of worn surface of the Tool Steel specimen at 600 °C under varying loads of (b) 10 N and (c) 30 N (d) 40 N.....	85
Figure 3.46 XRD pattern of worn out Tool Steel at a) room temperature, b) 400 and c) 600 °C.....	86
Figure 3.47 Frictional coefficient and wear rate of Tool steel with (a) Frictional coefficient v/s Temperature (b) Wear rate v/s Temperature .....	87
Figure 3.48 Camera photographs of a) Cr <sub>3</sub> C <sub>2</sub> -NiCr+NiCrSiB, b) SS316L+WC-CrC-Ni and c) Tool Steel MIM samples subjected to cyclic oxidation at 700 °C in air for 50 cycles.....	88
Figure 3.49 Plot of oxidation cycles (a) weight gain per unit area (b) square of weight gain per unit area.....	89
Figure 3.50 Plot of oxidation cycles (a) weight gain per unit area (b) square of weight gain per unit area.....	90
Figure 3.51 XRD pattern of Cr <sub>3</sub> C <sub>2</sub> -NiCr+NiCrSiB at 700 °C.....	91

Figure 3.52 XRD pattern of SS316L+WC-CrC-Ni at 700 °C. ....	92
Figure 3.53 XRD pattern of Tool Steel MIM samples oxidized at 700 °C. ....	92
Figure 3.54 Oxidised MIM material system cross section a) Cr <sub>3</sub> C <sub>2</sub> -NiCr+NiCrSiB b) SS316L+WC-CrC-Ni c) Tool Steel.....	93
Figure 3.55 Surface morphology and EDS analysis of oxidized Cr <sub>3</sub> C <sub>2</sub> -NiCr+NiCrSiB MIM sample at 700 °C.....	94
Figure 3.56 X-ray mapping of oxidized Cr <sub>3</sub> C <sub>2</sub> -NiCr+NiCrSiB at 700 °C.....	95
Figure 3.57 Micrograph of surface morphology and EDS analysis of oxidized SS316L+WC-CrC+Ni at 700 °C.....	96
Figure 3.58 X-ray mapping of oxidized SS316L+WC-CrC+Ni at 700 °C.....	96
Figure 3.59 Micrograph of surface morphology and EDS analysis of oxidized Tool Steel at 700 °C. ....	97
Figure 3.60 X-ray mapping of oxidized Tool Steel at 700 °C. ....	98

## NOMENCLATURE

MIM: Metal Injection Moulding

PIM: Powder Injection Moulding

PW: Paraffin Wax

PEG: Polyethylene glycol

SA: Stearic Acid

LDPE: Low-Density Polyethylene

DSC: Differential Scanning Calorimetry

TGA: Thermogravimetry Analysis

XRD: X-ray Diffraction

SEM: Scanning Electron Microscope

EDS: Energy Dispersive Spectroscopy

ASTM: American Society for Testing and Materials

Cr: Chromium

Cr<sub>3</sub>C<sub>2</sub>: Chromium Carbide

Cr<sub>2</sub>O<sub>3</sub>: Chromium Oxide

Co: Cobalt

COF: Coefficient of Friction

Ni: Nickel

NiO: Nickel Oxide

UTS: Ultimate Tensile Strength

WC: Tungsten Carbide

Al<sub>2</sub>O<sub>3</sub>: Aluminium Oxide

WO<sub>3</sub>: Tungsten Oxide



## **CHAPTER 1**

### **1. INTRODUCTION**

Modern industry requires the production of various components in large quantities. Many of them have complicated shapes and small sizes. Selection of a proper production method for such components is a difficult task. Traditional machining is expensive. Components produced near net shape methods like casting often have low tolerances and unsatisfactory quality of surface finish. Some types of components can be efficiently produced by methods of powder metallurgy. But conventional powder metallurgy is applicable for production of relatively simple shapes. Isostatic pressing ensures very high-quality products, but it is a low productive and expensive technology. The real breakthrough among the near net shape techniques became the metal injection moulding (MIM) process, capable of producing high-performance and complex shaped metal parts and mass production of near net shape components, avoiding the machining step and saving resources up to about 20–50 % of the final cost (Melli et al. 2015). The process has developed from the injection moulding approach used for forming plastics products.

MIM process includes mixing binder with fine metal powders to produce a feedstock. The developed feedstock is moulded to form the green parts by utilizing the conventional injection moulding machines. The appropriate choice of the ratio of powder to the binder and mixing methods decides the success or failure of metal injection moulded parts (Aggarwal et al. 2006, Li et al. 2007). The binder assists to provide better flowability and formability with fine metal powders during moulding and are removed at a later stage to produce high-dense parts. The solvent extraction method is used to remove binder subjected to heat exposed the green part to form an open porous in the brown part. The overall success of the process to manufacture high-quality parts are dependent primarily on appropriate control of processing steps, choice of starting material, powder, and binder type and its proportion. Binder acts as a temporary vehicle to powder and also provides the fluidity which necessary for moulding (Shahbudin et al. 2017). The maximum solid fraction of the mixture has strong influences on moulding, the green strength of the mould part and the properties

of the final products. Properties of processed products can also be manipulated using careful control of processing and raw material parameters. Feedstock, a mixture of metal powder and the binder has to be homogeneously mixed. The surface of the powder is completely wet and covered by the binder material, resulting in potential interaction during mixing. This could be chemically and physically interaction, which would result in the formation of new species and the development of attractive or repulsive forces (Romano et al. 2006). In the MIM process, the debinding is the most critical step which uses sintering condition that ensures pore-free structure possess better mechanical properties. Typically, the binder removal could open up pore channels that allow extracting at a faster rate of higher boiling point parts. The backbone is the small portion of residual binder in the parts, which handle the parts when it is transferred to a sintering furnace (Imgrund et al. 2007).

Thermal removal of the residual binder is the initial step in the sintering process to open the pore channels in the part. Sintering process defines the particle densification subjected to heat, which helps the atomic movements either by solid state diffusion or due to the formation of a liquid phase wetting the particle surface. The part shrinks to their final dimensions by eliminating porosity during the sintering process. Machining and other secondary manufacturing operations are optional to enhance the properties of the parts. MIM process manufacture parts with a wide variety of materials thus provide interesting tribological properties, which may not be manufactured efficiently with other processes (Jisa et al. 2014).

Powder metallurgy (P/M) techniques may be favourable for near net-shaped manufacturing of  $\text{Cr}_3\text{C}_2\text{-NiCr+NiCrSiB}$ ,  $\text{SS316L+WC-CrC-Ni}$ , and Tool steel alloys reducing tool wear and material loss to a minimum. Additionally, constraints like segregation and extensive grain growth of the P/M techniques can be avoided, from metal injection moulding. The various traditional methods for fabrication of metal components are presently using in the industry are press sintering, casting, and machining etc. The major disadvantage of the traditional process is as the shape complexity increases the unit cost also drastically increases. MIM is particularly attractive for near-net-shaped production of components with complex geometries. Metal injection moulding process has the potential for producing an interacted shape



with close tolerance, and good mechanical properties at a lower cost, over conventional metal making technologies (Ma et al., 2014).

The distinguished features of the MIM process are the ability to provide complex shaped parts with highly precise dimension tolerances and properties, and relatively higher production rates. The biggest advantages of this MIM process poses high sintered density, ability to manufacture intricate shape with better mechanical and surface integrity in comparison with other traditional powder metallurgy compacts (Jamaludin et al. 2009).

A typical application of powder metallurgy parts are gun and armament parts, food and beverage parts, medical and dental devices, computer, machinery and office parts. Rocker arm, turbocharger, cooling nozzle, and fuel injector parts are manufactured for automotive applications with the help of the MIM process.

MIM offers design flexibility and complexity at low unit cost as shown in Figure 1.1 The MIM process is a near net shape process and which do not demand secondary machining operations for the production of geometrically complex parts, as like conventional metal powder process does (Abolhasani et al.2009).

Metallic matrix composites (MMCs) was given much attention and used widely in the machinery industry over several years due to their outstanding mechanical and thermal properties (Ho et al., 2008). The tribological properties of part surfaces namely wear, frictional force at room and elevated temperature pose a serious problem in many engineered parts of aircraft, automobile and metallurgical industries. Tungsten carbide based composites have shown an outstanding performance in different industrial areas (Kaur et al., 2011). These composites use carbide particles reinforced in a metallic matrix to obtain the desirable higher hardness and toughness metallic properties. Carbide based composite typically poses distinguished applications in both abrasive and oxidizing environments. These composites exhibit high hardness and different wear behaviours. However, till date, not much research efforts reported in detail with regard to their fabrication by metal injection moulding. From the literature, it is found that further research is still needed to investigate the development of a suitable binder for MIM and which may be fabricated for laboratory or in actual industrial conditions.

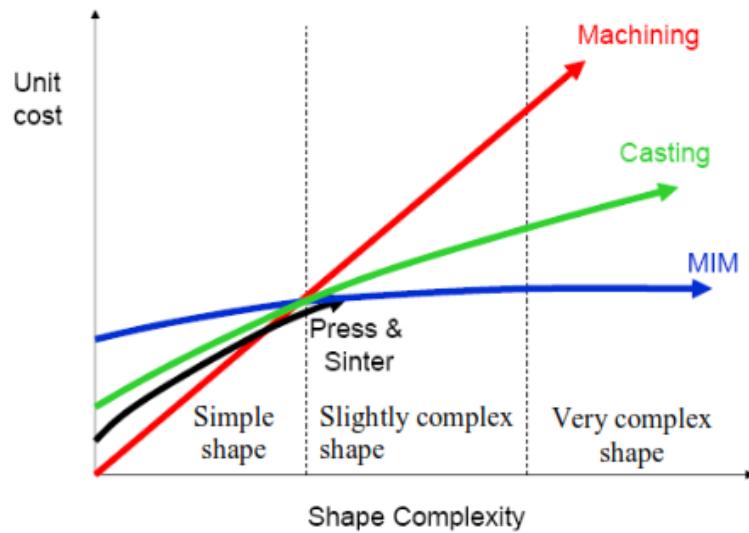


Figure 1.1 Different processes cost vs. the shape complexity (Kong 2013)

The current investigation includes fabrication of  $\text{Cr}_3\text{C}_2\text{-NiCr+NiCrSiB}$ ,  $\text{SS316L+WC-CrC-Ni}$ , and Tool steel heat-resistant composite through metal injection moulding (MIM) process. The composites are characterized with respect to mechanical and microstructure. The high-temperature wear and oxidation properties are evaluated.

## 1.1 LITERATURE SURVEY

MIM is one among the newly developed net shape manufacturing process which are capable enough to manufacture small and intricate shaped parts with the help of metal powders in large quantities. This process uses the hybrid manufacturing technologies by combining the desirable features of conventional powder metallurgy and plastic injection moulding processes. The plastic parts processed through plastic injection moulding are widely used in engineering industry due to their inherent characteristics to manufacture highly complex shaped parts at lower cost. However, the plastic parts pose inferior properties in comparison with structural metallic or ceramic materials. On the other hand, metals or ceramics which are available in powder form can be processed through conventional powder metallurgy to manufacture components but with poor shape complexity. Metal injection moulding overcomes the material limitation of plastic injection moulding and shapes complexity of conventional powder metallurgy thereby a new range of components is produced which were previously

restricted to polymers only. The advantages of MIM over the other manufacturing processes lies with combined attributes, such as it overcomes property limitations of plastic injection moulding, shape complexity limitations of conventional powder metallurgy, low production rate limitation of slip casting, the high production cost of machining and defects in investment casting. The main advantage of MIM is the economical production of complex components out of high-performance materials in large quantities. Variety of materials such as stainless steel, nickel base alloys, nickel-molybdenum steel, titanium, tool steel, tungsten heavy alloys, zirconium, silicon carbide, alumina are being presently processed through PIM (German 1990, Liu et al. 2000, Zauner 2006, Liu et al. 2005, Oh et al. 2003, Scott Weil et al. 2006). The application area of MIM includes automobile, aerospace, medical, electronics, consumer products, sports, armaments etc. (Dehghan-Manshadi et al. 2017) and some of the components manufactured through MIM includes wrist watch case and wrist watch band, lock mechanism, teeth straightening bracket, needle valve, I.C. engine valves, medical implants, turbine wheel, core for investment cast turbine rotor blade etc. (German 1990, Ikeda et al. 2014, Martin et al. 2013, Kuebler and Blugan 2011)

Figure 1.2 shows the schematic diagram of the whole MIM process. Mixing or feedstock preparation, injection moulding, debinding, and sintering are the four major steps in the MIM process. Everything in MIM begins with the preparation of feedstock or mixing of fine powders (metal or ceramic) with a binder. Very frequently binders used in MIM is thermoplastic base (Karataş et al., 2008, Scott Weil et al. 2006, Dobrzański et al. 2006) which melts on heating and solidifies as it cools but water base, thermosetting resin base and other types of binders are also used (Thavanayagam and Swan 2018) (Porter 2003) (Hayat et al. 2015). The binder coats the powder particles upon which the powder particles reach the vicinity of the mould cavity during the injection moulding stage. The metal powders alone cannot be injected which are mixed with high viscosity binder, thus provide a better viscosity suitable for the mouldable range. In general, mixing of metal powders and binders are carried out in a sigma blade mixer or z-blade mixer or by twin screw extruder subjected to heating above the binder melting temperature, wherein the powder particles are uniformly coated and dispersed. The prepared mixture of metal powder and the binder is referred to as feedstock. Ease

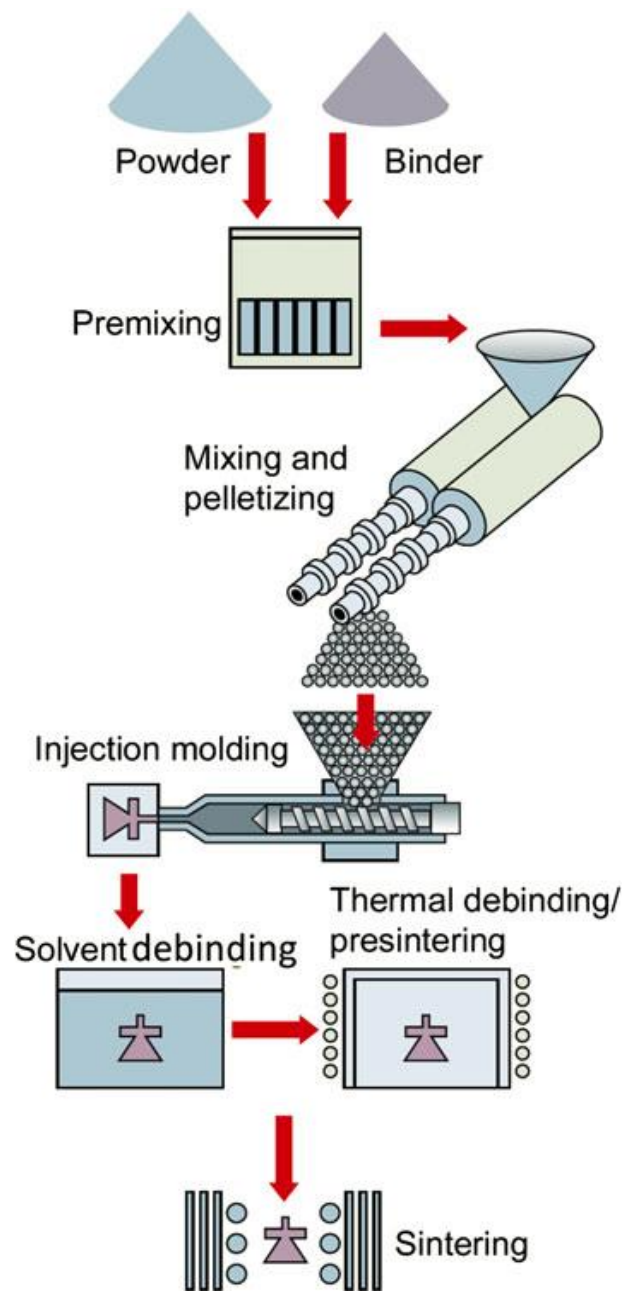


Figure 1.2 Schematic representation of MIM process (Sidambe 2014)

of feeding the feedstock to injection moulding machine is done with the help of preparing small pellets. The pelletized feedstock is supplied with ease into the injection moulding machine during injection moulding stage. Then the feedstock melts inside the barrel subjected to thermal treatment, and the molten feedstock is carried away by the helix of the rotating screw inside the barrel to the front of the screw tip, which is often similar to that of plastic injection moulding technique. At the forward stroke of the screw, the molten feedstock is injected inside the mould with high injection pressure

and temperature through the nozzle. Molten feedstock completely fills the mould cavity and imparts the desired component shape.

After ensuring complete solidification of the molten feedstock inside the mould, which imparts the desired shape as per mould cavity and the part is ejected out from the mould. The part obtained during this stage is referred as green compact. The role of the binder is over after successful completion of injection stage.

The binder is removed from the green compact during the debinding stage. Debinding is a very delicate process as a binder is removed without distorting the shape of the green compact. Debinding process depends on binder design. Binder can be removed by immersing the green compact in a solvent or liquid called solvent debinding or by degradation of the binder by heating the compact to sufficiently high temperature. After removal of the binder, the compact becomes porous and difficult to handle.

The green compact retains its shape by the interparticle friction among the powder particles after removal of the binder. The last and final stage of MIM is sintering. The structural integrity of the compact is developed in this stage. Sintering is essentially a thermal treatment process. The rebound compact is heated to below melting temperature of powder. The part subjected to thermal treatment develops a strong intermetallic bonding action between the particles contact surface as a result of neck formation similar to that of conventional powder metallurgy process. It must be mentioned here that both metal and ceramic powders are processed through MIM. When metal powder is processed, the process is specifically called Metal Injection Moulding (MIM) and when the ceramic powder is processed, it is called Ceramic Injection Moulding (CIM). Though MIM and CIM are quite similar there is a certain difference in processing metal powders and ceramic powders (Liu and Tseng 1998, Nor et al. 2013).

Because of the unique advantages of MIM such as high sintered density (around 97% of theoretical), high surface finish and good dimensional control (0.3- 0.4%), better or comparable mechanical properties, automatic production line, low manufacturing cost, wide range of material processing and minimum wastage (Dimitri et al. 2017, Daudt et al. 2017, Kate et al. 2014) manufacturing industry all over the world is showing keen interest on MIM. Frequently, manufacturers opt for MIM route for their new products. The worldwide status report on MIM shows that cumulative shipments of MIM product through

2016 was estimated globally at \$1900 Million, Asia is around \$914 million, India is \$125 million. It shows a promising growth of the MIM industry in the near future BCC Research (for Global, Asia numbers).

## **1.2 Powder, binder and feedstock attributes**

MIM feedstock is a balanced mixture of powder and binder. Therefore, it is necessary to determine the proper composition of feedstock. Binder is used in MIM to carry the powder particles by reducing its viscosity. The amount of binder depends on powder particle packing as the void spaces between the powder's particles should be completely filled to provide mouldable viscosity. There can arise three possible situations for a powder-binder mixture as shown in Figure 1.3. The powder volume fraction at which the binder is just sufficient to completely fill the void spaces among the powder particles as well as to form a layer on powder particle surface and powder particles be in point contact with each other as shown in Figure 1.3 (a) are called critical powder loading. When the powder loading is much lower than the critical powder loading as shown in Figure 1.3 (b), there is an excessive amount of binder in the feedstock which is not acceptable. Excessive binder content can cause powder binder separation (Thian et al. 2002) during moulding, resulting in anisotropic shrinkage during sintering and causing greater dimensional shrinkage during sintering which makes the dimensional tolerance control very difficult. Besides, due to the absence of inter particles friction among the powder particles compact shape made of feedstock with excessive binder content cannot be retained during debinding. On the other hand, when powder loading exceeds the critical powder loading, binder content becomes insufficient and the voids form in the feedstock as shown in Figure 1.3 (c). Higher powder loading above the critical loading increases the viscosity so high, that moulding becomes very difficult (Atre et al. 2007, Ibrahim et al. 2009). Therefore, it is very important to determine the critical powder loading for the formation of feedstock.

Quality of feedstock depends on powder and binder characteristics (Liu et al. 2003, Suri et al. 2003). The powder particle characteristics those are important to MIM are powder packing density, particle shape, and size. Among the above, powder packing density is the most important as it dictates the amount of binder content in the feedstock. The packing density of powder indicates the amount of void space that exist among the powder particles and which are required to be filled by the binder.

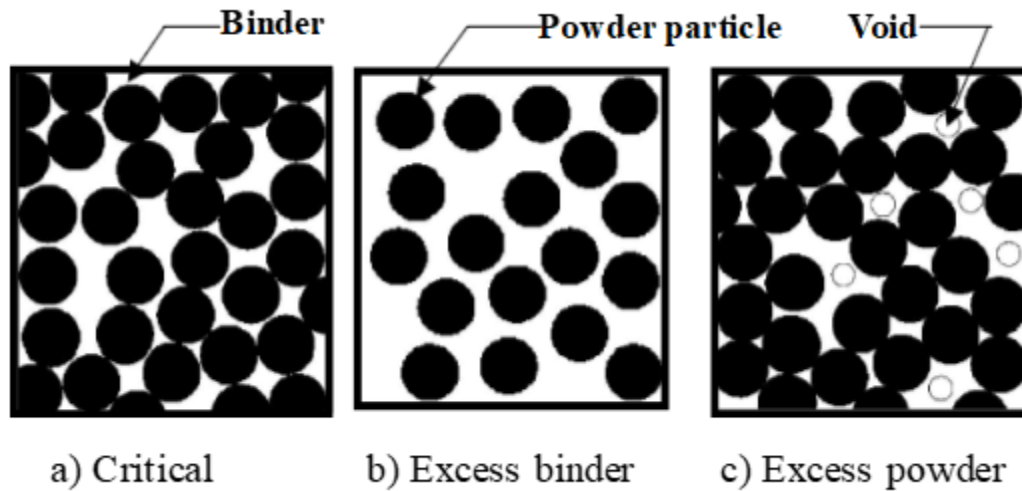


Figure 1.3 Powder-binder mixture

If packing density decreases, amount of binder requirement will be high and which is not desirable as high binder content causes separation of powder and binder during injection moulding. Moreover, high binder content causes compact slumping during debinding and excessive shrinkage occurs during sintering which makes difficult to achieve tight dimensional control (Kong et al. 2012). Therefore, it is desirable to have a high packing density powder for MIM processing. In MIM application, packing density varies from 0.3 to 0.8 of theoretical density, with a typical value of 0.6 (Kong et al. 2012).

### 1.3 Powder particle shape and size

Powder particle shape and size are very important for successful MIM. Powder particle shape has an influence on interparticle friction among the powder particles. As the particle shape becomes irregular than spherical, interparticle friction increases. Interparticle friction influences packing density, mixing, debinding, sintering and viscosity of feedstock which in turn affects injection moulding. Irregular shape particles decrease the powder packing density and require more mixing time to attain homogeneity due to greater interparticle friction. Irregular shape particles increase the viscosity of feedstock requiring high injection pressure during injection moulding. However, powder particles having irregular shape are advantageous during debinding. During debinding, as the binder leaves the compact, the shape of the compact is

retained by the interparticle friction of the particles. As interparticle friction is greater among the irregular shape powder than a spherical shape, irregular shape powder is desirable for debinding. Since powder packing density is low for irregular shape powder, more densification is needed to compensate for the poor initial packing. Powder particle size influences the packing density(Liu et al. 2005, Ferri 2010). A particle with a narrow size distribution or mono size powder does not improve the packing density but large particle size distribution improves the packing density substantially. For maximizing the packing density, wide size distribution powder is used where large particles form the skeleton and small particles fill the pores between the large particles(Suri et al. 2005). It can be seen that particle characteristics are in conflict but always higher packing density is desirable.

#### **1.4 Selection of Binders**

Though binder in MIM serves as a carrier for the powder particles and its role is finished after moulding, the formulation of the binder is most important for successful MIM processing. Binder must be designed in such a way that it provides sufficient fluidity maintaining mouldable viscosity during injection moulding and at the same time binder leaves the compact without disturbing the compact. Moreover, a decomposition product of the binder must be non-corrosive. Different types of binders can be designed for MIM such as thermoplastic, thermosetting, water-based binder, inorganic compounds etc. but thermoplastic base binders are widely used which melt on heating and solidify upon cooling. Therefore, the emphasis is given here on the thermoplastic base binder. Table 1.1 and

Table 1.2 shows some related studies in the field of binders and debinding for MIM.

Generally, multicomponent (more than one constituent) binder is designed in view of easy binder removal during debinding. One component of the binder is removed first creating open pores for subsequent removal of the other components of the binder by evaporation without generating an internal vapour pressure that might cause compact distortion or failure. It is desirable to have low binder viscosity. Since thermoplastic polymer viscosity and debinding time increases with chain length (Li et al. 2005), it is common to have low molecular weight short chain polymer as a binder material. Wax,



due to its low molecular weight, short chain and thermoplastic behaviour are widely used in MIM processing than any other material. To design multicomponent binder wax along with other polymers such as polyethylene glycol (PEG), Low-density polyethylene (LDPE), along with surfactant such as stearic acid (SA) which are partially insoluble with each other are mixed together. Besides the powder and binder characteristics, the viscosity of feedstock, which relates shear stress to shear strain, has a very important effect in MIM processing as it influences the injection moulding stage for the uniform filling of feedstock in the mould.

Table 1.1 Different binder systems for MIM feedstock

Reference	Binders Used	Remarks
Fox et al. 1992	Polyvinyl acetate (PVA) + Water, Ethylene vinyl acetate (EVA) + Paraffin Wax (PW)and Polyacrylonitrile (PAN) + EVA + High-Density Polyethylene (HDPE)	A water-soluble binder system consisting of PVA was found to be unsuitable for MIM, as the viscosity was too high and the surface finish of the micro-components was poor. In the case of the PW + EVA binder system, thermal de-binding caused slumping problems. A binder system comprising PAN + EVA + HDPE proved to be suitable for use due to easy flowability in the microcavities and easy de-binding of the binder at a later stage.
Fox et al. 1990	Cellulose acetate butyrate (CAB) and poly(ethylene glycol)(PEG)	This blend exhibited low enough viscosity to make homogeneous feedstock for MIM. Shape maintenance during the extraction of the binder by water was excellent, and the final sintered parts had excellent dimensional stability ( $\pm 0.3\%$ ) and a high sintered density over 98%. Also, the injection cycle time was comparable to that of commonly used wax-based feedstock.
Jinyan et al. 2009	Paraffin wax (PW) + HDPE	The mould filling behaviour was better than other binders used in previously mentioned studies; however, the shrinkage in the part was fairly high. It was also found out that less temperature of

Reference	Binders Used	Remarks
		debinding increase the bending strength which is very important in the technological lines producing tools by the $\mu$ PIM method.
Ahn et al.2009 Dehghan et al. 2017	PW + PEG + Low Density Polyethylene (LDPE) + Polypropylene (PP)	Good flowability in microcavities and good shape Retention was found. However, the shrinkage in the final Sintered part was high.

Table 1.2 Debinding methods used for MIM feedstock

Reference	Debinding process	Summary
Almanar et al. 2011	Single-step thermal debinding at 800 °C was carried out for 150 minutes.	The binders used were PEG and CAB. No residue of PEG was found at 420 °C. Complete removal of CAB/PEG binders was observed at 800 °C with lots of sink marks on the final part. These sink marks are due to the higher debinding temperatures and short time of exposures.

Reference	Debinding process	Summary
(German 2017)	Multiple-step debinding was conducted at 650 °C for 90 minutes.	In this study PVA, EVA, PW and PAN were the binder systems used. The binder removal was conducted in stages, such that after every stage the shape of the part is retained by another binder. It was observed that removal of PW shows the maximum amount of change in the dimension of the part. This method was found to be expensive compared to the single-step thermal debinding method.
(Dobrzański et al. 2006)	Thermal debinding under an inert atmosphere.	This study involved the use of PW as a binder. The inert atmosphere was helpful to increase the evaporation of PW at slower rates to maintain the dimensions of the final part. The final part was found to have fairly high density compared to other thermal debinding methods.
(L. Liu et al. 2005)	Multiple-step debinding combined with an inert atmosphere.	PAN and LDPE were the binders used in this study. Removal of LDPE was attainable at 320 °C while the temperature was raised to 450 °C to remove PAN. The inert atmosphere helps the removal of binder slowly, maintaining the dimension of the final part. The final part was found to have the highest density compared to other thermal debinding methods.

The viscosity of Newtonian fluids such as water and other low molecular weight liquids is constant and does not depend on shear rate but depends on temperature. Newtonian fluids follow the Newtonian law of viscosity which states that shear stress is related to shear strain rate via a constant called Newtonian viscosity. Most polymeric materials (Davies et al. 2008, Thavanayagam et al. 2018, L. Liu et al. 2005, Li et al. 2007, Reddy et al. 2000, Khakbiz et al. 2005) do not follow Newton's law of viscosity. The viscosity of these fluids decreases with increasing rate of deformation or shear rate as well as with the increase in temperature. This phenomenon of decreasing viscosity with increasing rate of deformation is called as pseudoplastic or shear thinning behaviour. This viscosity is called non-Newtonian viscosity and various models such as Power Law Model, Carreau Model, Bird-Carreau-Yasuda Model, Cross-Williamson Model etc. are available in the literature to describe the pseudoplastic behaviour (Khairur et al. 2011, Albolhasani et al. 2009). Among the above non-Newtonian viscosity models, Power Law Model proposed by Ostwald and de Waale is the most frequently used two-parameter model for engineering applications (Thavanayagam et al. 2014, Agote et al. 2001) for its simplicity compared to other models. The Power Law Model of viscosity states that,

$$\mu = m(T)\dot{\gamma}^{n-1}$$

Where  $\mu$  is the viscosity,  $m$  is the consistency index which may include temperature dependence of viscosity and  $n$  is the Power Law index. For shear thinning or pseudoplastic fluid, the parameter  $n$  is less than 1 and  $n$  is greater than 1 for dilatants or shear thickening fluids. When  $n$  becomes 1, the constant Newtonian viscosity is achieved through this model. Since MIM feedstock exhibits shear thinning behaviour i.e. as the shear strain rate increases, viscosity decreases (Huang et al. 2003, Khakbiz et al. 2005), generally injection moulding is carried out between 100-1000 s<sup>-1</sup> shear strain rate (Ibrahim et al. 2009) where mouldable viscosity prevails at the moulding temperature. A sketch of typical viscosity variation with shear strain rate and temperature is shown in Figure 1.4. The viscosity is measured using a rheometer. Generally, two types of rheometers are used for viscosity such as cone and disc

rheometer and capillary rheometer. Cone and disc rheometer system are limited to very low shear rate applications(Mizerakova 2013).

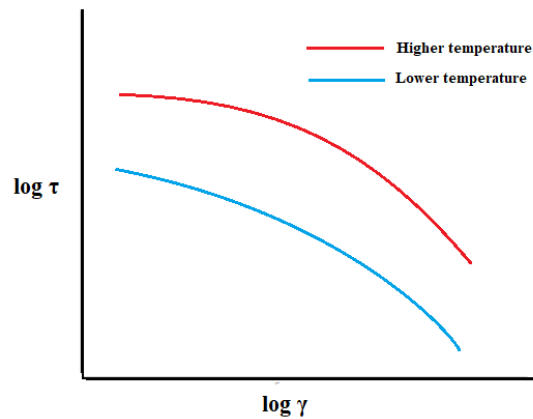


Figure 1.4 Viscosity of typical PIM feedstock

The viscosity is measured using a rheometer. Generally, two types of rheometers are used for viscosity such as cone and disc rheometer and capillary rheometer. Cone and disc rheometer system are limited to very low shear rate applications(Mizerakova 2013). On the other hand, capillary rheometer is used for high shear rate applications such as in injection moulding. Literature review shows that viscosity of polymers, MIM binders and feedstock for injection moulding applications are measured using capillary rheometer(Huang et al. 2003; Reddy et al. 2000; Liu et al. 2005; Sulong et al. 2013). Thermal properties such as specific heat and thermal conductivity of feedstock are also important. They affect the cooling time of the compact during injection moulding. Generally, the specific heat of feedstock is quite low compared to that of binder and due to the presence of powder, the thermal conductivity of feedstock is several times higher than the binder (Bilovol et al. 2000).

## 1.5 Moulding Tool for MIM

In the injection moulding stage of MIM, the feedstock is heated till it attains sufficient fluidity and forced into the mould to produce components of the desired shape. The success of the MIM depends on the quality of green compacts coming out from mould which in turn depends on efficient mould design and quality of the mould construction. A mould is designed based on the factors such as component shape, size, weight,

number of components required, dimensional tolerances, surface roughness etc. A schematic diagram of the injection mould is shown in Figure 1.5.

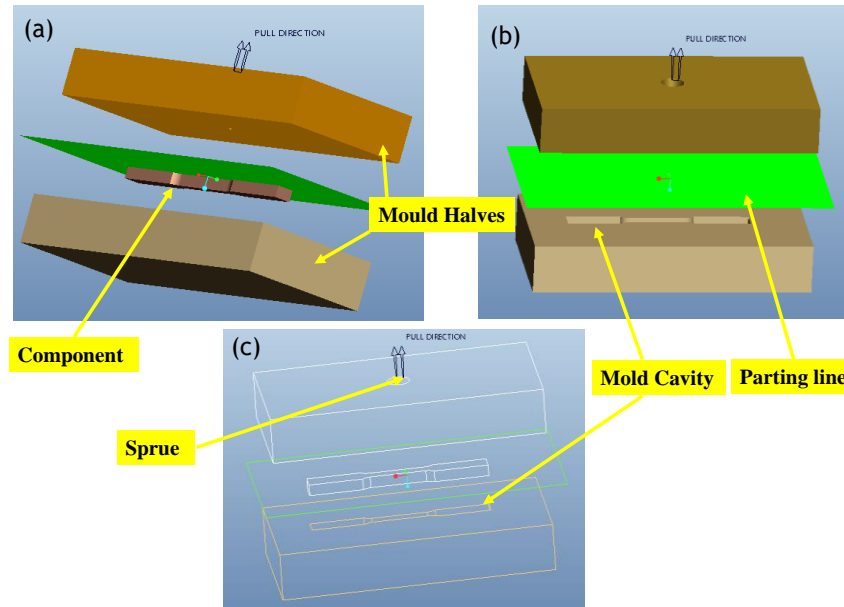


Figure 1.5 Schematic diagram of an injection mould for MIM

Mould is made of two halves and cavity i.e. the shape of the component is cut in the mould where feedstock is injected into the shape of the components. The feedstock is injected into the mould cavity from the nozzle through a delivery system which itself is also a part of the mould. The delivery system includes sprue, runner and in-gate as shown in Figure 1.5. The design of the delivery system affects the moulding parameters such as injection pressure required to push the feedstock into the cavity, temperature drop, filling time. Sprue provides the path for molten feedstock to flow from the nozzle to the runner. Sprue cross-section is circular and slight taper is provided for easy removal from the mould. Too small diameter nozzle increases filling time and introduces strains in the material being moulded. Moreover, air entrapment may occur. The runner of the delivery system carries the molten feedstock to the in-gate. The smaller the cross-section of the runner, the greater the pressure requirement, the temperature drops and the longer the mould filling time. Therefore, a larger cross-sectional area with smaller runner length is desirable for shorter filling time, less injection pressure and less temperature drop. For easy removal from the mould, wherever it is possible, the runner should be placed in the ejector half of the mould. The

in-gate is the smallest cross section in the delivery system that restricts the flow of molten feedstock into the mould cavity. After filling of the cavity, the feedstock in the in-gate area solidifies first compared to the other portion of the delivery system and full mould cavity under pressure solidifies completely over a certain time period while injection screw moves back to prepare itself for next injection cycle. Because of early solidification at the gate area, molten feedstock under pressure in the mould cavity cannot come out through the delivery system when the injection pressure is withdrawn by backward movement of the screw. The cross-section of the in-gate may be rectangular, round, fan or fin type (Handbook of Injection metal Moulding, 2012). Since MIM components are small and requirements are huge, generally multi-cavity moulds are prepared so that in a single injection cycle many components may be produced to increase the productivity. As components shrink after sintering, the mould cavity is made oversized to compensate for the shrinkage upon sintering. The mould is fitted with properly distributed ejector pins to eject out the moulded green compacts smoothly after completion of the cooling stage. Among the two halves of the mould, locating pins are fitted in the movable half and locating pin holes are drilled in the fixed half. For controlling the mould temperature thereby heat flux flow from the feedstock to the mould wall, a cold/hot fluid is circulated through the channels inside the mould. The fluid is heated or cooled in a chamber outside the mould and then pumped through the channels. Usually, water or oil is used as mould heating/cooling fluid and hardened tool steel is used as the mould material.

## **1.6 Injection moulding stage of MIM**

The injection moulding stage of MIM is similar to that of conventional plastic injection moulding. It is essentially melting of feedstock and filling of molten feedstock into the mould. A schematic diagram of injection moulding is shown in Figure 1.6. The pelletized feedstock is feed into the hopper. Due to rotational movement of the screw, the feedstock is carried towards the nozzle and at the same time, as it passes through the heated barrel, it melts. Molten feedstock accumulates in front of the screw tip. The molten feedstock is injected into a clamped mould with sufficient injection speed and pressure during the forward movement of the screw generated by the exertion of hydraulic pressure on the ram, as mould temperature is lower than the molten feedstock



temperature, volumetric contraction of the feedstock in the mould cavity occurs with reduction in feedstock temperature. This volumetric contraction is compensated through the further supply of molten feedstock by maintaining a follow-up or holding pressure for sufficient time after filling the cavity. When the in-gate is solidified, this follows up pressure is withdrawn. After solidification of the feedstock inside the mould, the mould opens to eject out the green compact (component) from the mould and the cycle repeats. Heat content and viscosity of the feedstock varies in this stage, as it moves through the externally heated barrel and the mould (Handbook of Metal Injection Moulding, 2012). The sequence of the injection moulding cycle from beginning to end is as follows: Closing of mould halves Filling of the mould cavity by forwarding movement of screw Packing or holding pressure phase Cooling or solidification of feedstock inside the mould cavity Opening of mould halves Ejection of green compact from the mould cavity. Quality of green compact depends on various process parameters(Ibrahim et al.2010,(Kim et al. 2014) such as pressure, temperature, the viscosity of feedstock etc. in injection stage and one of the important parameters is injection speed or rate of mould filling (Bilovol et al. 2006).

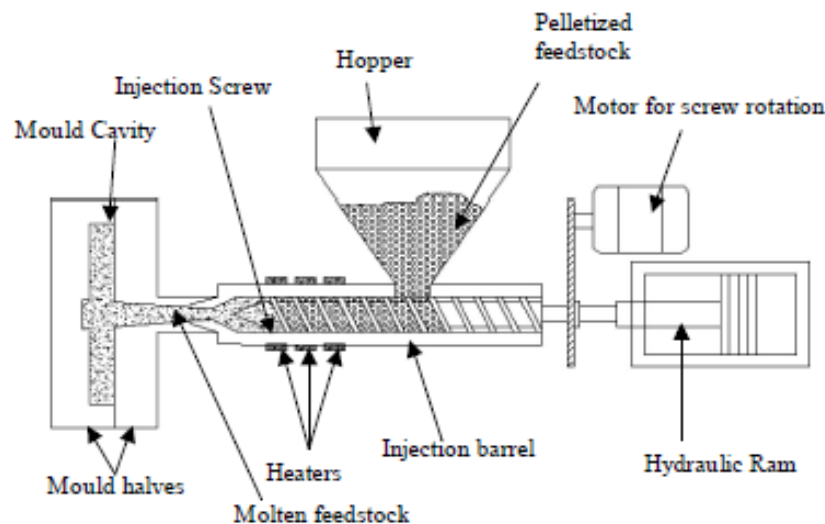


Figure 1.6 Schematic diagram of an Injection moulding

The injection rate depends on the machine setting. At the beginning of injection, as molten feedstock enters into the mould, it does not face any resistance and therefore injection pressure is slow at the beginning. But as the feedstock continuously fills the

mould cavity, it encounters increasing resistance and therefore injection pressure gradually increases towards the end of mould filling. A low viscous melt at high injection speed when flows through the in-gate, jets out to strike the distant wall opposite and turns backwards. Otherwise, flow, the front of the feedstock melts advances inside the mould cavity uniformly if the wall thickness is uniform and in the case on non-uniform wall thickness melt flow front advances more towards thicker section than a thinner section. High injection speed leads to free jets causing matt surface in the green compact. On the other hand, very low injection speed causes the gramophone effect t on the compact surface especially with high viscosity (Handbook of Metal Injection Moulding, 2012). The feedstock can be injected in both, constant injection speed as well as variable injection speed. Variable injection speed can be used for injecting components with variable cross sections to maintain the constant flow front velocity (Bilovol et al. 2006). The switchover from the filling phase to follow up or holding pressure phase should take place smoothly. Sometimes, switch over from filling phase to packing phase does not occur at the same instant in each cycle. This may be attributed to change in viscosity of feedstock caused by temperature variation. This problem is solved by reducing the injection speed prior to the switchover. As mentioned above, volumetric contraction is compensated by allowing more feedstock to flow in the packing or holding phase till the in-gate freezes. This transfer of feedstock flow should be as minimum as possible as reverse flow may take place due to overpacking. Overpacking makes ejection difficult and a longer cycle time (Handbook of Metal Injection Moulding, 2012).

## **1.7 Debinding stage of MIM**

In Metal injection moulding (MIM) process, the binder is mixed with metal powder and molten binder carries the powder particle to the vicinity of the mould during injection moulding stage. Thereby, the binder in MIM acts as a carrier and after completion of the injection stage, the role of the binder is finished. It is necessary to drive out the binder from the injection moulded green compact, as the aim of the MIM process is to manufacture metallic/ceramic component out of the metal/ceramic powder. The technique to remove the binder from the green compact is called the debinding process. Debinding is a very delicate process as binder should be removed without distorting the

shape of the green compact and after removal of the binder compact shape should be preserved through the interparticle friction of the powder particles. Generally, defects (Thian et al. 2001, Shengjie et al. 2002) such as compact shape distortion, compact cracking and swelling are associated with improper debinding and these defects cannot be corrected during sintering. Debinding or removal of binder depends on the binder design. Generally, multi-component binder system is designed for MIM (Matula et al. 2008, Dobrzański et al. 2006, Gerling et al. 2006, Shibo et al. 2006) where binder components are removed progressively in different steps. The debinding technique can be broadly categorized as solvent debinding and Thermal debinding. In solvent debinding technique, some of the binder components are dissolved when the green moulded compact is exposed to a suitable fluid. In this technique, an open pore structure is created (German 1990) which can be used to remove the rest of the binder components by evaporation. Solvent debinding can be carried out in three different ways: by immersing the compact in a solvent or by pressuring the solvent to exceed a critical condition or by heating the compact in the presence of a solvent or its vapour. In the thermal debinding technique, the binder is removed by thermal degradation or evaporation or by liquid extraction (wicking). When the compact is heated to a temperature high enough above the degradation temperature of binder components, thermal degradation of the binder components starts and they are removed from the compact in gaseous form by diffusion or permeation. In liquid extraction, the compact is placed on the porous substrate and heated such that viscosity of binder becomes very low thereby under gravitational force it comes out of the compact in liquid form and sucked into the pores of wicking substrate. At the end of injection moulding, as a binder is solidified, it holds the powder particle in place by providing a mechanical interlocking and thereby shape of the compact is maintained with required handling strength. As the binder leaves the compact, void spaces or pores are created in the interparticle spaces. After removal of the binder, the green compact becomes porous and pores are interconnected. The compact becomes fragile until sintered. Figure 1.7 shows the pore structure formed during debinding through which binder permeates to the surface of the Compact.

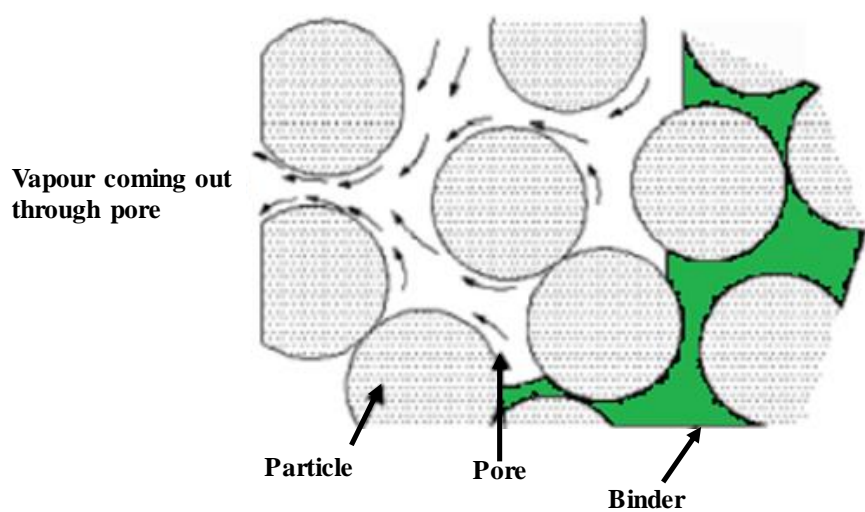


Figure 1.7 Removal of binder through the pores during thermal debinding by saturation

## 1.8 Sintering stage of MIM

Sintering is the last stage of MIM processing. The structural integrity of porous debound compact results from sintering. Sintering is essentially a thermal treatment process by which loose powder particles are bound together into a coherent solid mass. Due to mass flow, the neck grows at the contact points among the particles that cause the bonding between the particles (Liu et al. 2011) as shown in Figure 1.8. The mass flow occurs by atomic motions that act to eliminate the high surface energy associated with un-sintered powder particles. Mass is transferred by the motions of the atoms and thereby, bonding between the particles can occur either in a solid state or in the liquid phase. The mass transfer becomes faster with the increase in temperature as atomic motion scales up with the melting temperature of the respective metal/ceramic. Therefore, MIM compacts are sintered at a temperature near the melting point of the respective metal/ceramic to induce faster sintering. Mass flow mechanisms during sintering are broadly classified into two types: mass flow via surface transport mechanism and mass flow via volume transport mechanism. Figure 1.9 shows the mass flow path by the atomic motion of the atoms during sintering. In surface transport mechanism, mass flow originates and terminates at the particle surface. Neck grows at the point of particle contact but without changing any particle spacing thereby no densification occurs in the surface transport mechanism.

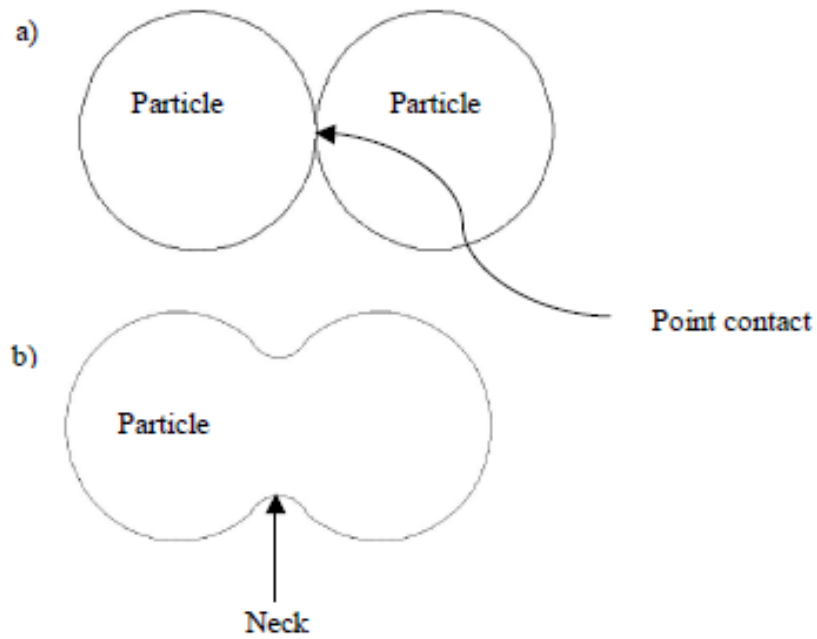


Figure 1.8 Powder particle sintering a) two particles are in point contact before sintering, b) particles bound together by neck formation during sintering

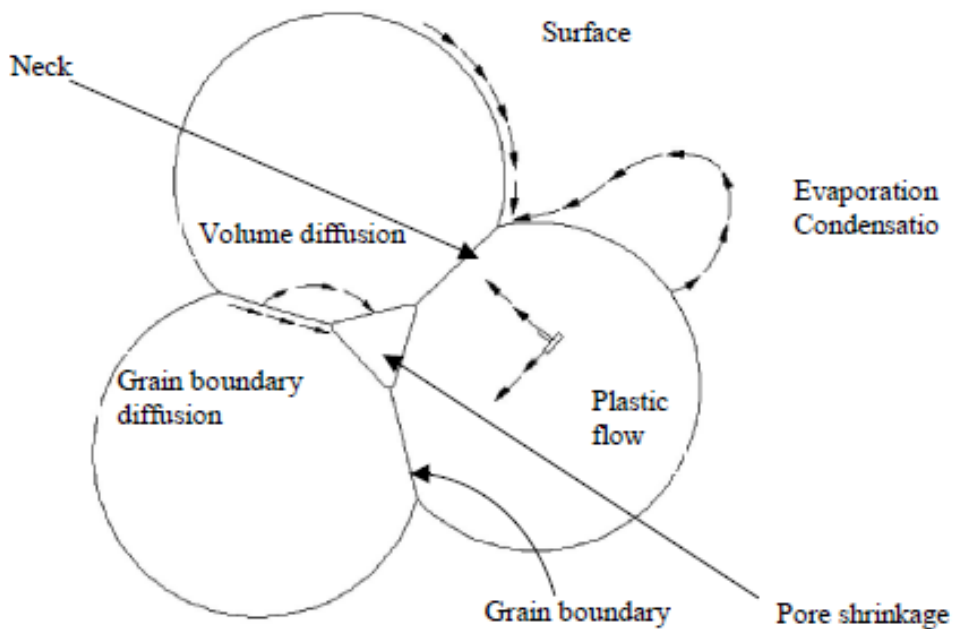


Figure 1.9 Mass transport mechanism during sintering

Mass flow occurs via surface transport mechanism by surface diffusion, condensation evaporation, and diffusion adhesion. But surface diffusion and condensation

evaporation are pre-dominant factors. On the other hand, in the bulk transport mechanism, mass is transported from the interior of the particles to the neck. Densification and shrinkage occur in the compact due to the flow of mass from the interior of the particles to the neck. Mass flow occurs via bulk transport mechanism by plastic flow, viscous flow, volume diffusion and grain boundary diffusion. Viscous flow is associated with amorphous material and plastic flow does not have much importance in MIM (German 1990). Grain boundary diffusion and volume diffusion are important in bulk transport mechanism. Pores are considered as an accumulation of void spaces as shown in Figure 1.9. Atoms move along the grain boundary to continuously amass in the pores thereby densification occurs by eliminating pores. Grain growth phenomenon is a common problem in sintering as grains enlarge reducing the desirable grain boundary area necessary for sintering (Pan-wei 2009). Therefore, grain structure must be controlled for better mechanical properties in the sintered specimen.

Sintering takes place in three stages as shown in Figure 1.10. In the initial stage, as the debound specimen is a heated neck formation start at the contact point of the powder particles. In this stage, compact strengthening occurs without densification or shrinkage and surface transport mechanism plays the dominant role to occur mass flow in this initial stage of sintering (Loh et al. 2001).

In the intermediate stage, as the temperature increases, the neck grows faster with considerable densification and shrinkage in the compact. Densification causes the elimination of pores but pore structure in this stage becomes cylindrical and smooth. Grain growth occurs at the last portion of the intermediate stage. At the elevated temperature, cylindrical pores break down into isolated spherical pores and separated from the grain boundaries. The creation of isolated pores indicates the beginning of the final sintering stage.

The rate of sintering or densification slows down as grain growth continues in this final stage too as pores are not effective to resist grain growth. But grain size is important for better mechanical properties such as tensile strength, hardness. The gases filled in the spherical pores limit the maximum densification.

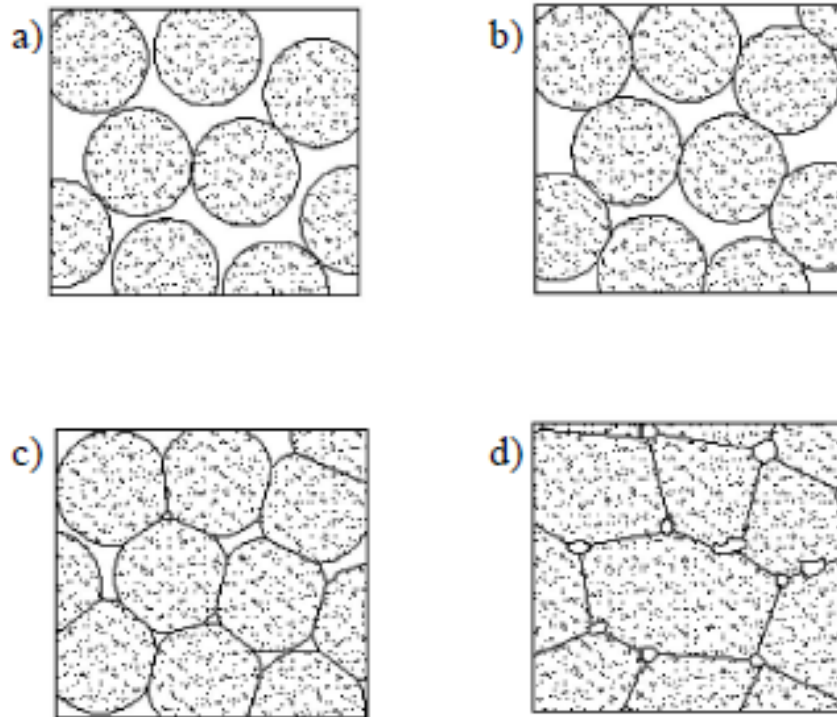


Figure 1.10 Microstructure of the compact at various stages of sintering (a) debound stage (b) Initial stage (c) intermediate stage (d) final stage

Therefore, sintering is measured by compact density which increases by the elimination of pores. To improve densification thereby properties of sintered compact, one of the three approaches can be used. These are phase stabilization, activated sintering and liquid phase sintering. In the phase stabilization technique, some phases are stabilized during sintering whose volume diffusivity is higher than other phases by the addition of some phase stabilizing materials. For example, during sintering of iron, due to higher volume diffusivity of the ferrite phase, the ferrite phase is stabilized for higher densification by addition of phosphorous or silicon. Inactivated sintering, an additive is added in the powder to increase the sintering speed by lowering sintering temperature. During sintering, the additive forms a lower melting point phase by dispersing to the interparticle contact point. As additive melts at a lower temperature it generates a path for higher diffusion so that sintering speed increases and sintering is carried out at a lower temperature. Similar to the activated sintering, when mixed powders are sintered, one component forms a liquid phase due to the difference in melting temperature. The

solid particles are surrounded by the liquid phase thereby a shortcut higher diffusivity path is created which accelerates sintering. This process is called liquid phase sintering. For liquid phase sintering, solid phase must be soluble in the liquid phase. The formation of the liquid phase is much higher in the case of liquid phase sintering compared to that of activated sintering. Therefore, a suitable sintering cycle needs to be designed for maximum density and better mechanical properties.

## **1.9 Problems and defects related to the injection stage of MIM**

Defects occurred in any stage cannot be repaired in the subsequent stages of MIM rather the defects become more prominent in subsequent stages causing rejection of components. Therefore, care should be taken in each stage of MIM. Among all other stages, the injection stage of MIM is most important. The shape of the green compact is formed in the injection stage and quality of sintered PIM components depends on the quality of the green compact formed in the injection stage. In spite of good understanding of basic injection cycle of MIM many defects(Liu et al. 2005) such as weld line, cracks, warpage, powder binder segregation, poor surface finish, parting line flash, jetting, voids, short shot, over packing etc. may occur in the green compact (Bilovol 2003). The above defects occur mainly due to the selection of improper process parameters. Injection stage is the most critical stage of PIM as the flow of the feedstock during filling of the mould cavity is determined by the interplay of numerous process parameters such as injection speed, feedstock temperature, mould temperature, injection pressure, packing or holding pressure, filling time etc. Residual stresses in the green compact are related to the shear and thermal condition experienced by the feedstock during the injection stage. Generally, MIM components are very small and complex and variation of cross sections are very common along the flow length. Therefore, flow front advances very fast at small cross sections and becomes slow at larger cross sections for a constant injection speed. Variable injection speed may be used but for small components, it is not so suitable due to the inertia of the injection moulding machine. As a result, feedstock experiences considerable acceleration and deceleration along the flow length. Moreover, viscous heating caused by friction between two adjacent feedstock layer causes local overheating (Bilovol et al.2000) and thin section solidifies faster than the thick section causing nonuniform temperature



distribution in the compact. This non-uniform temperature or unbalanced cooling induce residual stresses as with some binders stress relaxation time is much larger than the cooling time and a primary cause of compact warpage (Bilovol et al. 2000, Porter 2003). During mould filling as the thickness of the frozen layer of feedstock adjacent to the mould cavity wall increases, fountain flow of the feedstock may occur along the mould wall. Since the thermal conductivity of feedstock is much higher than that of thermoplastics, feedstock cools rapidly adjacent to the wall and this induces a large thermal stress and causes compact cracking. The above thermal stresses can be minimized by increasing the mould temperature and by increasing the injection speed. The problem with jetting occurs when feedstock enters into a mould cavity with larger thickness through a relatively smaller in-gate at high injection speed (Mori et al. 1997, Chan et al. 1978). This problem may be arrested by increasing viscosity of feedstock and decreasing the injection speed or increasing the cross-sectional area of the in-gate. Weld lines are formed where the feedstock streams re-join when feedstock flows around a core in the mould cavity or during injection through multiple in-gate. The weld lines in the compact may be eliminated by decreasing the viscosity of the feedstock by increasing mould and melt temperature thereby, allowing the streams to fuse properly with each other. Sometimes it is not possible to completely eliminate the weld line defect and, in that case, gate locations should be such that the weld line occurs in the unimportant part of the compact. Since MIM components are complicated, the flow direction of the feedstock changes frequently during mould filling. Sharp and frequent changes in flow direction increase flow resistance and thereby increasing the injection pressure required to push the feedstock into the mould cavity. Moreover, it causes separation of powder and binder in the feedstock. There is a large difference in densities between binder and powders, especially metal powders. Due to the higher density of the powder particle, they move with higher momentum and continue to flow along a straight path and when flow direction changes sharply, they accumulate unevenly in the mould cavity and introduce density gradients in the compact (Heldele et al. 2006, Banhart 2001). The density gradient in the compact causes strong anisotropy in the feedstock (You et al. 2012) and uneven shrinkage upon sintering (Gelin et al. 2010) (Shivashankar et al. 2013). The problems and defects in the injection stage may be eliminated or reduced by optimizing process parameters including mould design.

Processing window of MIM is very narrow as parameters contradict with another such as feedstock should be filled very fast to avoid short shot or premature solidification thereby increasing the injection speed but it is to be injected in such a way that excessive shear strain rate does not develop. Since there is the interplay of various process parameters, analytical optimization of the complex shape components is very difficult. The optimization can be done by trial and error technique but lots of time is required to standardize a single product and it costs dearly for expensive feedstock. Moreover, if the mould design is to be changed during trial and error technique, it involves lots of time as well as huge cost. Besides that, trial and error technique does not provide science-based insight about the injection stage to prevent similar problems in other products.

### **1.10 Summary**

A brief introduction is given to metal injection moulding and post-processing stages of MIM. A detailed literature survey is carried out on debinding, moulding and sintering process. From the existing literature, it is clear that nickel and chromium based material has not explored well as material for high-temperature wear, and oxidation resistant through metal injection moulding process. Hence, present work deals with the development of binders and sintering for composite materials consist of metallic, carbides, for elevated temperature applications. The gaps of the literature in the metal injection moulding process is identified. The aims and objectives of the present work are explained. The methodology followed to fulfil the said objectives is described. The chapter ends with the layout of the thesis.

### **1.11 Objectives of the research work**

1. Design and characterization of the binder system and feedstock for the MIM process. Following are the material systems.
  - a) Tool Steel (T-15)
  - b) SS316L (70%) +WC-CrC-Ni (30%)
  - c) NiCrSiB (70%) +Cr<sub>3</sub>C<sub>2</sub>-NiCr (30%)
2. Development of near-net-shape defect free metal injection moulding samples.

3. Sintering of MIM samples through conventional sintering and microwave sintering techniques.
4. Characterisation of Sintered MIM samples with respect to microstructure, physical and mechanical properties.
5. Evaluation of high-temperature wear behaviour of MIM samples under varying load, and temperature.
6. Evaluation of cyclic oxidation behaviour of MIM samples at 700°C.
7. Evaluating the mechanism of wear and oxidation using the combined technique of XRD, SEM, and EDAX.

## **1.12 Organization of the thesis**

The present work consists of five chapters and is summarized as follows:

**Chapter 1**, Contains introductory remarks on metal injection moulding application and advantages. Also presents a critical review of the published literature relevant to the present study. A literature review on metal injection moulding, feedstock formulation, factors influencing on the preparation of feedstock, moulding, debinding and sintering characteristics of the composite specimen and mechanical and tribology properties of MIM composite are presented. The objectives of the proposed research work are outlined after studying the detailed literature review and identified gap.

**Chapter 2**, Description of the experimental equipment's used, and various steps employed for fabrication of metal injection moulding components. Mixing of metal powder with binders and different debinding methods, moulding parameters details, and sintering conditions, characterization techniques used for analysis of microstructural features, mechanical properties and tribological behaviour of the MIM composites used in the present work.

**Chapter 3**, Chapter five deals with results and discussion of the work, and is divided into four sections. First section contains the characterization of powder, binder and feedstock. Second section contains different sintering methods. Section three contains mechanical characterization and fourth section contains wear and oxidation test results for three systems

MIM material systems.

Material system 1:  $\text{Cr}_3\text{C}_2$ -NiCr+NiCrSiB composites.

Material system 2: SS316L+WC-CrC-Ni composites.

Material System 3: Tool Steel T-15.

**Chapter 4**, Deals with concluding remarks of the investigation and future work.

## CHAPTER 2

### 2 EXPERIMENTATION

*This chapter explains the methodology of research work, material systems, description of all the fabrication and measuring equipment's, and experimental procedure used in the present work.*

#### 2.1 Powder particle size and Shape

The feedstock powder particle size and its distribution pattern were investigated using a particle size analyser (Make: HRLD, USA and model: 8000A) at 34° C and the dispersion medium used is ethylene glycol 50%. Powder particle shape was analysed through SEM. (Make JSM -6380LA, JEOL).

#### 2.2 Feedstock preparation

The metallic powders used in the study are 1) SS316L (70%) +WC-CrC-Ni (30%) 2) NiCrSiB (70%)+Cr<sub>3</sub>C<sub>2</sub>-NiCr(30%) 3) Tool Steel. The chemical composition of a material system is given in Table 2.1.

Table 2.1 Material system chemical composition

Material System	Cr	Ni	C	B	Si	Mo	Mn	W	Co	V	Fe
NiCrSiB	14.5	73.3	0.6	3	4.3	-		-	-		4.3
Cr <sub>3</sub> C <sub>2</sub> -NiCr	60.5	30	9.5	-	-	-		-	-		-
SS316L	16.7	10.4	2.5	-	1.0	2.6	0.8	-	-		66
WC-CrC-Ni	21	6	5	-	-	-	-	68	-		-
Tool steel	4	-	1.6	-	0.3	0.7	0.3	12	5	4.90	71.2

Low-Density Polyethylene (LDPE), Polyethylene Glycol 600(PEG 600), Stearic Acid (SA), and Paraffin Wax (PW) are the major constituents of thermoplastic binder. Figure

2.1 shows the images of binders for preparation of feedstock. The feedstock is prepared with 56 % powder loading and 44% binder by volume. In Table 2.2 to Table 2.5 the corresponding composition of the binder and feedstock by weight percentage of its ingredients is given.



Figure 2.1 Binders for preparation of the feedstock

Table 2.2 The binder composition

Sl. No.	Type of the ingredients	Wt. (%)
1	PW (Loba Chemie Pvt.Ltd.)	52.0
2	PEG 600 (Loba Chemie Pvt.Ltd.)	10.0
3	LDPE (Indian petrochemical corp. Ltd.)	35.0
4	SA (Loba Chemie Pvt.Ltd.)	3.0

Table 2.3 Feedstock composition for material system SS316L+WC-CrC-Ni

Sl. No.	Type of the ingredients	Wt. (%)
1	SS316L (70%) +WC-CrC-Ni (30%)	81
2	PW	9.8
3	PEG 600	1.9
4	LDPE	6.65
5	SA	0.57

Table 2.4 Composition of the feedstock for material system NiCrSiB+ Cr<sub>3</sub>C<sub>2</sub>-NiCr

Sl. No.	Type of the ingredients	Wt. (%)
1	NiCrSiB (70%) + Cr <sub>3</sub> C <sub>2</sub> - NiCr (30%)	86
2	PW	7.28
3	PEG 600	1.4
4	LDPE	4.9
5	SA	0.42

Table 2.5 Feedstock composition of Tool Steel

Sl. No.	Type of the ingredients	Wt. (%)
1	Tool Steel (Grade: T-15)	92
2	PW	4.16
3	PEG 600	0.8
4	LDPE	2.8
5	SA	0.24

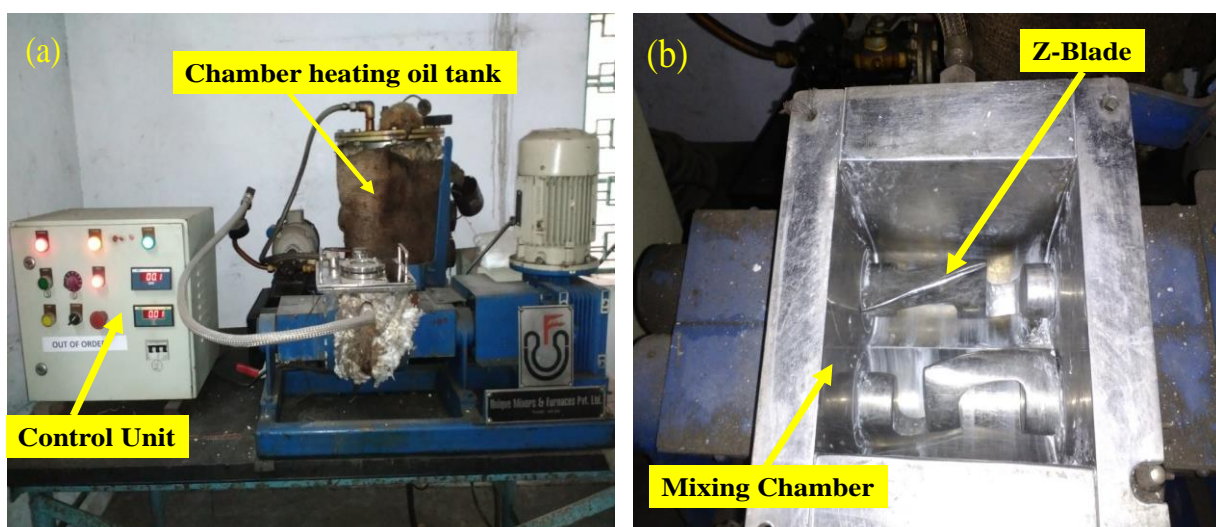


Figure 2.2 Sigma blade mixer a)Sigma blade mixer with temperature unit b) Mixing chamber

The feedstock has been prepared as per the composition specified (Table 2.3 to Table 2.5) in a sigma blade mixer as shown in Figure 2.2 (Make: Unique Mixers & Furnaces-

Thane, Capacity: 1 Lt) at 135°C for 90 minutes at 35 rpm. The prepared semi-solid feedstock viscous feedstock obtained after mixing thoroughly has been taken out and allowed to cool at room temperature. Note that the feedstock becomes hard and solid when it is subjected to room temperature. Later, it is then pelletized to feed in the injection moulding machine.

### 2.3 DSC studies of feedstock

The thermal properties (i.e. melting range and solidification range) of the feedstock has been determined by utilizing Pyris Diamond DSC (HICHAN-2510). The temperature has been maintained in the ranges of 40 to 240 °C with a constant heating rate of 10 °C/min and cooling has been carried out at a rate of 10°C/min in an helium gas atmosphere.

### 2.4 Viscosity of feedstock

The viscosities of feedstock are measured using a rotational rheometer (MCR501 Anton Paar, Austria).

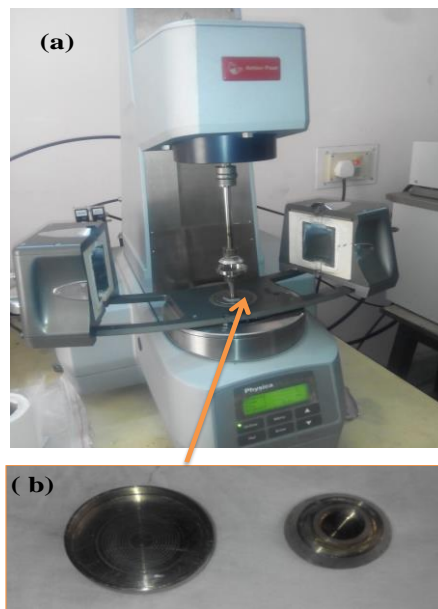


Figure 2.3 Rotational rheometer a) open chamber b) plate

The images of the rotational rheometer are shown in Figure 2.3. Rheological characteristic was developed at three different temperatures in the range 210–230 °C in 2 °C steps on the rotational rheometer.



## 2.5 Thermogravimetry analysis (TGA) of binder and feedstock

The binder system behaviour with regard to temperature is investigated by thermogravimetry analysis (TGA). The TGA of feedstock is conducted within the temperature range of 50-600 °C by utilizing Pyris Diamond TG/DTA system (Perkin Elmer Instrument, USA) maintained at a constant heating rate of 10 °C/min.

## 2.6 Injection moulding

The mould tool is designed initially by using modelling software (Pro/Engineer Wildfire 5.0), the models are shown in Figure 2.4(a-c).

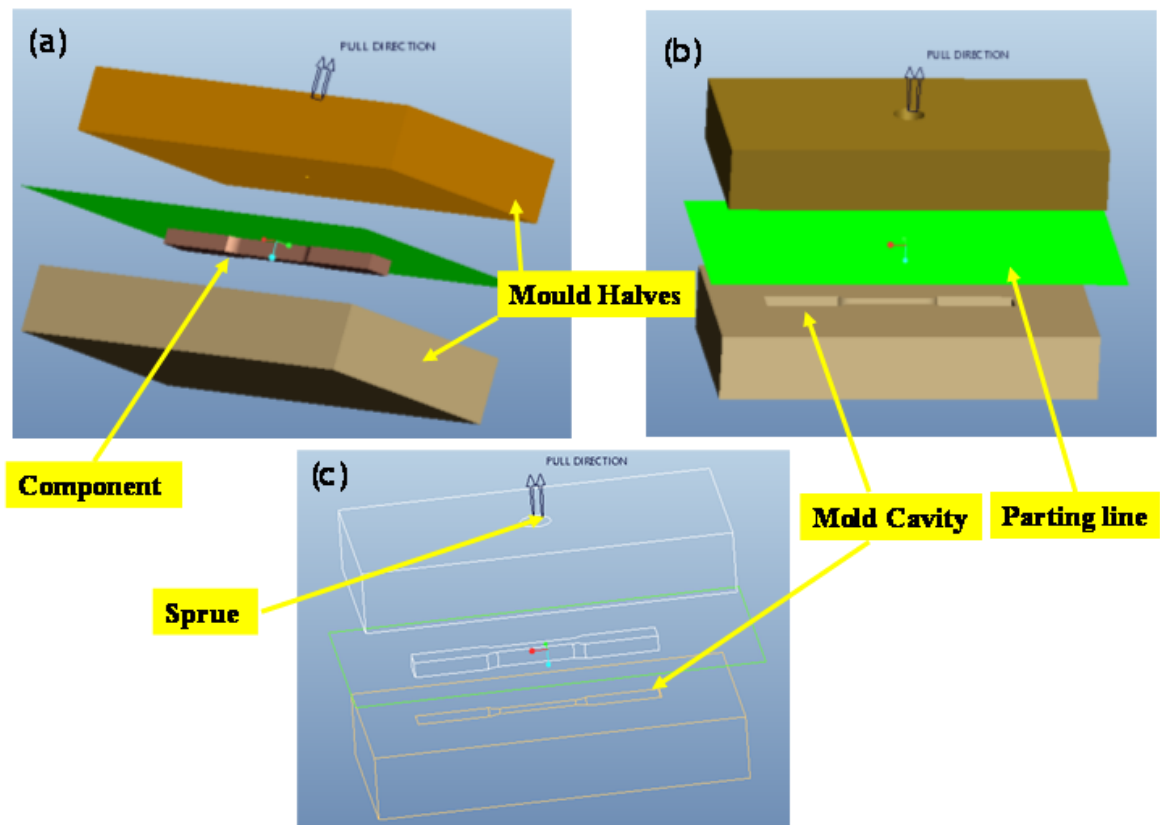


Figure 2.4 Injection mould inserts with a) Reference part & parting Surface b) cavity, c) wireframe model of the core cavity

The Pro/E models are converted to Initial Graphics Exchange Specification (IGES) models for the machining by CNC machine. The injection moulding is carried out using

a 150-ton injection moulding machine (Make: DGP Windsor- India, Model No. DIGI Micro 150H).

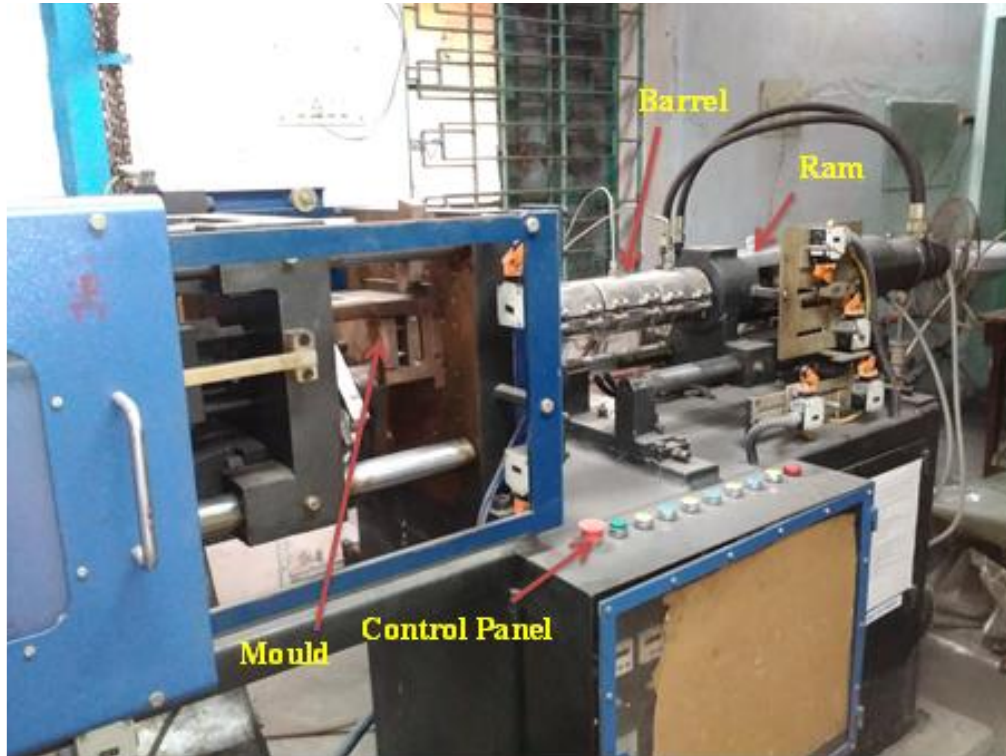


Figure 2.5 Injection mould used for fabrication.

A standard injection mould for tensile specimen shape cavity with ejection system was fabricated as shown in Figure 2.5 with mould wall thickness of 35mm bottom and top plate. The injection pressure was measured by a pressure sensor in the range 0 -100 bar, (Make: GEMS-UK, Model: 1200BGC4001A3UA) installed in the hydraulic line, which pushes the injection screw inside the barrel. A standard 40 mm diameter screw and barrel assembly was used for injection moulding. Multiple injection speed was used to inject the feedstock into the mould. In the first set, injection speed is set to 5% of the maximum injection speed of 138 cc/s (6.9 cc/s). Subsequently, the total injection time of 4s is adapted for an injection speed of 7.5 % of 138 cc/s (10.35cc/s). The injection speed of 15% of the maximum injection speed (20.7 cc/s) is adopted for rest of the injection time at an injection temperature of 190° C, 200° C and 210°C.

After several trials, the parameters selected for defect-free tensile specimens are injection speed of 41.4cc/s, injection time 3.7s and feedstock velocity 5.85m/s at injection machine barrel temperature 210 °C, 220 °C and 230 °C.

## 2.7 Debinding MIM samples

Debinding of the injection moulded specimen was carried out in two stages. The solvent debinding stage was carried out by immersing the moulded specimen in n-hexane ( $C_6H_{14}$ ) bath and heating the bath below the melting temperature of PW, where most of PEG-600, PW and SA are removed by dissolving in n-hexane. In the second stage, thermal debonding was carried out to remove the remaining PEG-600, PW, SA, and LDPE from the moulded specimen. Solvent debinding was carried out in a drying oven at different temperatures and time durations. After solvent debinding, the specimens are taken out of n-hexane and dried for 2 hours at  $40^\circ C$  in a drying oven as shown in Figure 2.6 (DASS and Co-Howrah). Subsequently, thermal debinding was carried out in a tube type furnace (Make: DASS and Co- Howrah, Model No.: EN120 QT) at different holding times and temperatures in a Hydrogen atmosphere with a heating rate of  $1^\circ C/min$ .



Figure 2.6 Debinding furnace a) Drying oven b) Thermal debinding furnace

## 2.8 Conventional Sintering

Conventional sintering of the debonded MIM specimens is carried out in a tube type furnace as shown in Figure 2.7 (Make: Naskar & Co. Howrah, India) under a hydrogen

atmosphere. The specimens are heated to a temperature of 1200 °C at a heating rate of 1-5 °C/min followed by soaking at that temperature for 30 minutes. The samples are cooled to 200 °C at a cooling rate of 5°C/min and then cooled to room temperature through furnace cooling.



Figure 2.7 Sintering furnace

## 2.9 Microwave sintering

The sintering process is carried out using microwave furnace (V.B ceramics, Chennai, India). Figure 2.8(a-b) show the line diagram of the microwave furnace and setup of microwave sintering process. Vacuum pump controls the air present inside the chamber, and also different inlets of the gas. In the present work, argon gas is utilized and to be ionized. The microwave energy is set within the range between 0.1 and 3 kW.

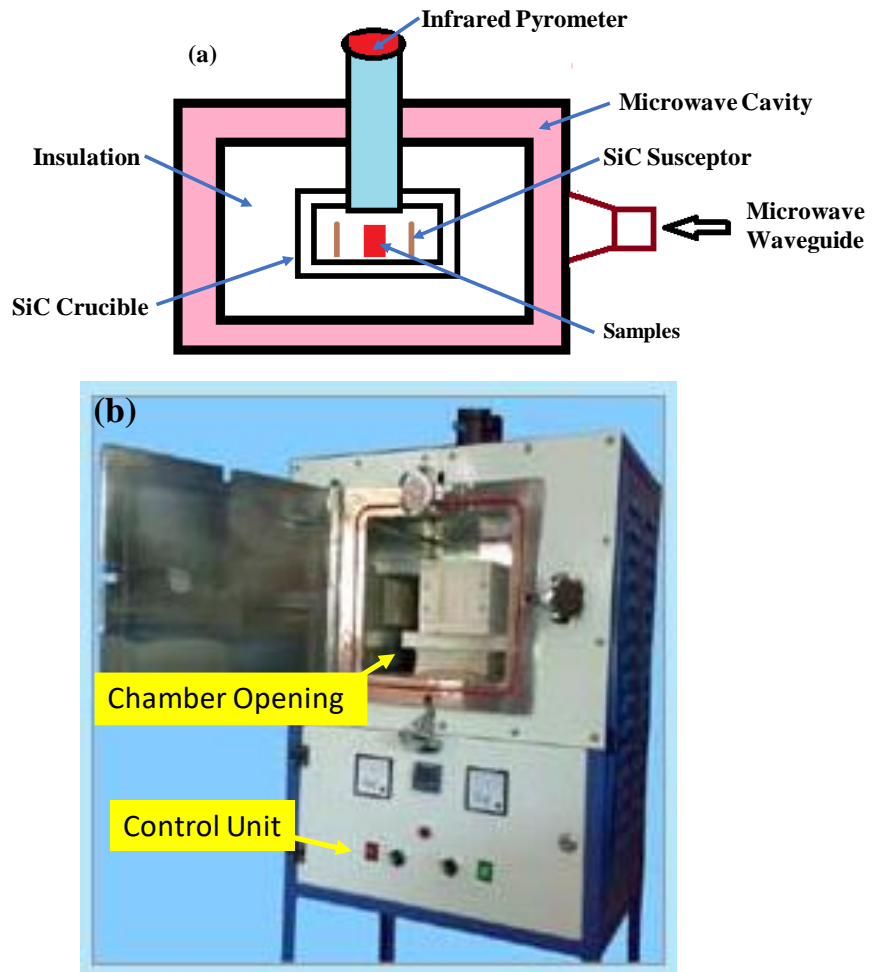


Figure 2.8 Experimental setup of microwave sintering furnace a) Line diagram  
b) Microwave furnace

## 2.10 Density measurement of the feedstock powder

The density of the feedstock powder was measured by water immersion method using pycnometer in accordance with American Standard for Testing of Materials (ASTM) C-135-03. The pycnometer used to measure sample weight in air and water is shown in Figure 2.9. The density of the feedstock powder is calculated using equation 1

$$\rho = \frac{(W-p)}{(w_1-p)-(w_2-w)} \quad \text{Equation 1}$$

p = weight of the stoppered pycnometer in g.

W = weight of the stoppered pycnometer and feedstock powder in g.

$W_1$  = weight of the stoppered pycnometer filled with water in g.

$W_2$  = weight of the stoppered pycnometer, feedstock powder, and water in g.



Figure 2.9 Pycnometer

## 2.11 Density measurement of sintered compact

The density of sintered MIM composite was measured in accordance with Archimedes principle. The test samples were weighed in air and in underwater using physical weighing balance. The density of the samples was calculated using Equation 2.

$$Density = \frac{Mass\ in\ air}{(Mass\ in\ air - Mass\ in\ water)} \times Specific\ gravity\ of\ water$$

Equation 2

## 2.12 Microstructural characterization

Study of the material behaviour is very much essential in metallurgical and material science because the crystallographic structure defines the properties of the material. Microstructural analysis of MIM processed samples are carried out to study the dimensional changes, sintering quality, and grain refinement. All the samples were sectioned along the cross-sectional direction. Metallographic specimens were cold mounted with the help of acrylic powder and resins. The specimens were polished up to 2000 grit SiC paper and final polishing was done with the help of cloth using 0.25

$\mu\text{m}$  diamond paste. For the microstructure analysis, chemical etching was performed in order to visualize grain boundaries. Polished samples were etched with acetic-picric solution (4.2 gm picric acid, 70 ml ethanol, 20 ml of glacial acetic acid and 20 ml of distilled water) solution and then dried in hot air. The following characterization techniques were used for observing the microstructures and evaluate the size of the grains and its orientation.

- Optical Microscope (OM)
- Scanning Electron Microscopy (SEM)

The optical microscopy of the MIM processed composite samples was carried out using an optical microscope with an image analysing software (BIOVIS materials plus) designed mainly for physical and metallographic applications. The optical microscope is as shown in Figure 2.10. Grain size measurements are done using liner intercept method

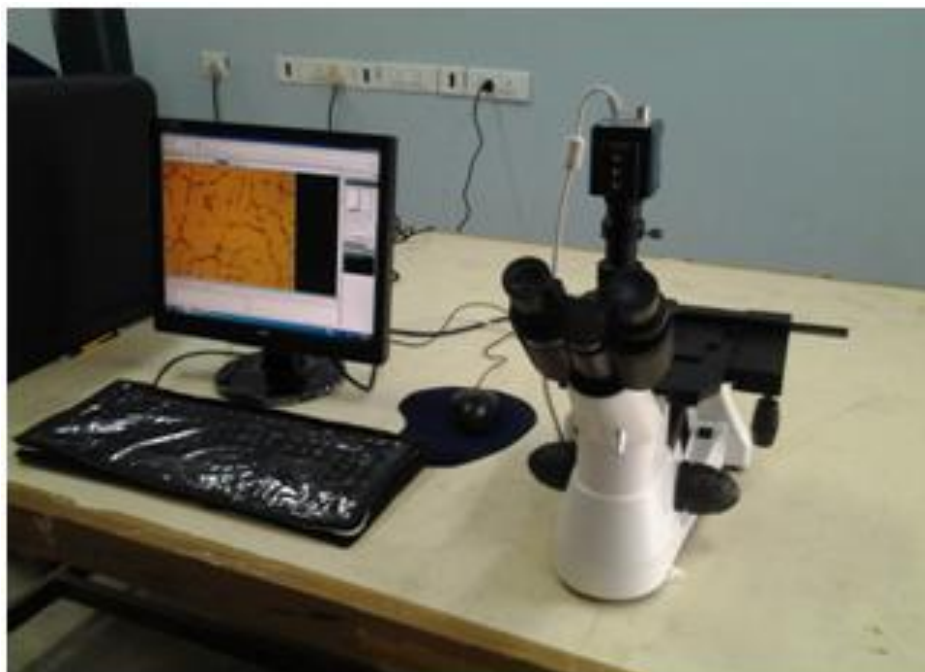


Figure 2.10 Optical microscope.

Scanning electron microscope (SEM) makes use of interactions between a high energy electron beam and a specimen to obtain topographic and microstructural information from the specimen. When an accelerated beam of electrons impinges upon the prepared

surface of the specimen, a variety of signals are produced. Secondary electrons are generally used for imaging and observation of topographical features on the surface.



Figure 2.11 Scanning electron microscope.

In the present study, the microstructural characterization was performed using a scanning electron microscope fitted (JEOL JSM- 6380LA; USA) with an energy dispersive spectrometer (EDS) as shown in Figure 2.11. EDS is used to carry out quantitative and qualitative elemental analysis.

### **2.13 Phase analysis using X-ray diffractometer (XRD)**

XRD.(JEOL, JDX-@P-XRD; USA) shown in Figure 2.12 was used to find the crystal structures and phase analysis of the MIM processed composites. The phase analysis was carried out in the cross-sectional direction so that all the area of the composites is exposed to the X-ray analysis. XRD analysis was carried out with the angle range of  $20^{\circ} \leq 2\theta \leq 95^{\circ}$  in steps of  $2^{\circ}$ /minute.





Figure 2.12 X-ray diffraction.

## 2.14 Microhardness of sintered MIM composites

Hardness is defined as the ability of a material to resist permanent indentation when in contact with an indenter under load.

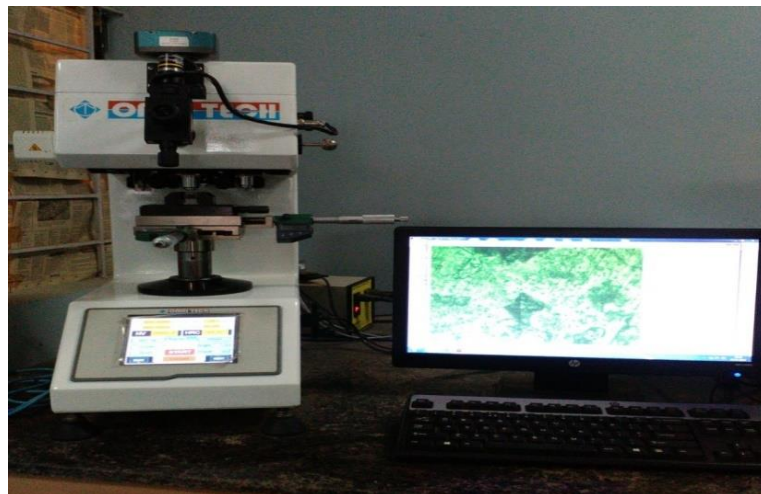


Figure 2.13 Microhardness testing machine.

Cross-sectional hardness in the MIM composites was measured by micro-indentation using the Vickers's microhardness testing machine (Omni-tech, Maharashtra, India) as shown in Figure 2.13. Initially, samples were polished and microhardness of the

samples was measured by imposing a load of 10 gm for a dwell time of 11 sec. A minimum of 10 indentations was taken throughout the surface to meet statistical reliability. The average microhardness was calculated and the error is expressed as the standard deviation of the total data set.

## 2.15 Tensile strength test

The tensile test was carried out using Tensometer (Tinius Olsen, Noida, India) as shown in Figure 2.14. according to ASTM E8 M standard at room temperature.

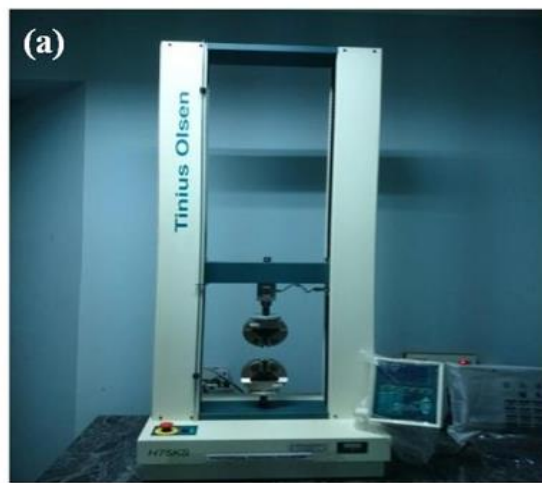


Figure 2.14 Tensometer

All the specimens were defect free MIM sintered compacts and are prepared as per standard gage length, the radius of fillet, length, and width. The thickness, width and gauge length of each specimen was measured before and after the tensile test. Fractured surface was analysed using electron microscope to investigate the type of fracture.

## 2.16 Cyclic oxidation test

Cyclic oxidation tests were carried out on sintered MIM samples at 700 °C for 50 cycles using tubular furnace (Heatron Industrial Heaters, Mangalore, India) as shown in Figure 2.15. Prior to the test, the surface area of the sample is measured. Each cycle consists of 1 hour of heating at 700 °C followed by cooling at ambient temperature for 20 minutes. Weight change is recorded for each cycle by electronic balance having a sensitivity of 0.01 mg. cyclic oxidation is conducted to simulate actual conditions in the real time application (frequent power failures).

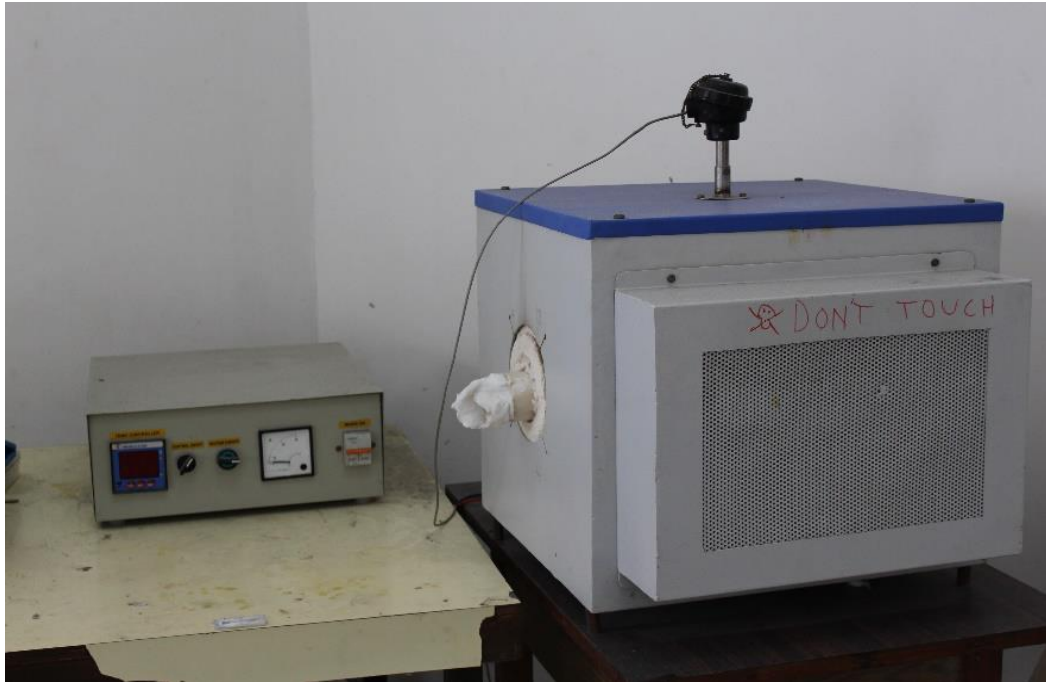


Figure 2.15 Tubular furnace.

## 2.17 Sliding wear test

Figure 2.16 (a) shows high-temperature pin on disc tribometer (TR-20LE-PHM 400-CHM 600, Ducom Instruments Pvt Ltd, Bangalore, India) used for friction and wear measurements. The test is conducted under dry conditions as per (ASTM G99-05) standard. Alumina disc is used as the counter body. Schematic representation of the test setup is presented in Figure 2.16 (b). Sliding wear tests are conducted with the normal loads of 10, 30 and 40N at sliding velocity of 1 m/s with a constant sliding distance of 3000 m. The test temperatures chosen are 200, 400, 600 °C. A computer-aided data acquisition system is utilized to concurrently record both height loss (using inbuilt displacement transducer) and frictional force. Friction coefficient is computed by dividing the frictional force by normal load. Wear rate is calculated by converting the height loss into volume loss using the pin cross section area and expressed in terms of  $\text{mm}^3/\text{m}$  (Manakari et al. 2015). Subsequent to wear test, the worn surfaces are observed through SEM. Results of the tests envisaged here are elaborately discussed in the section to follow.

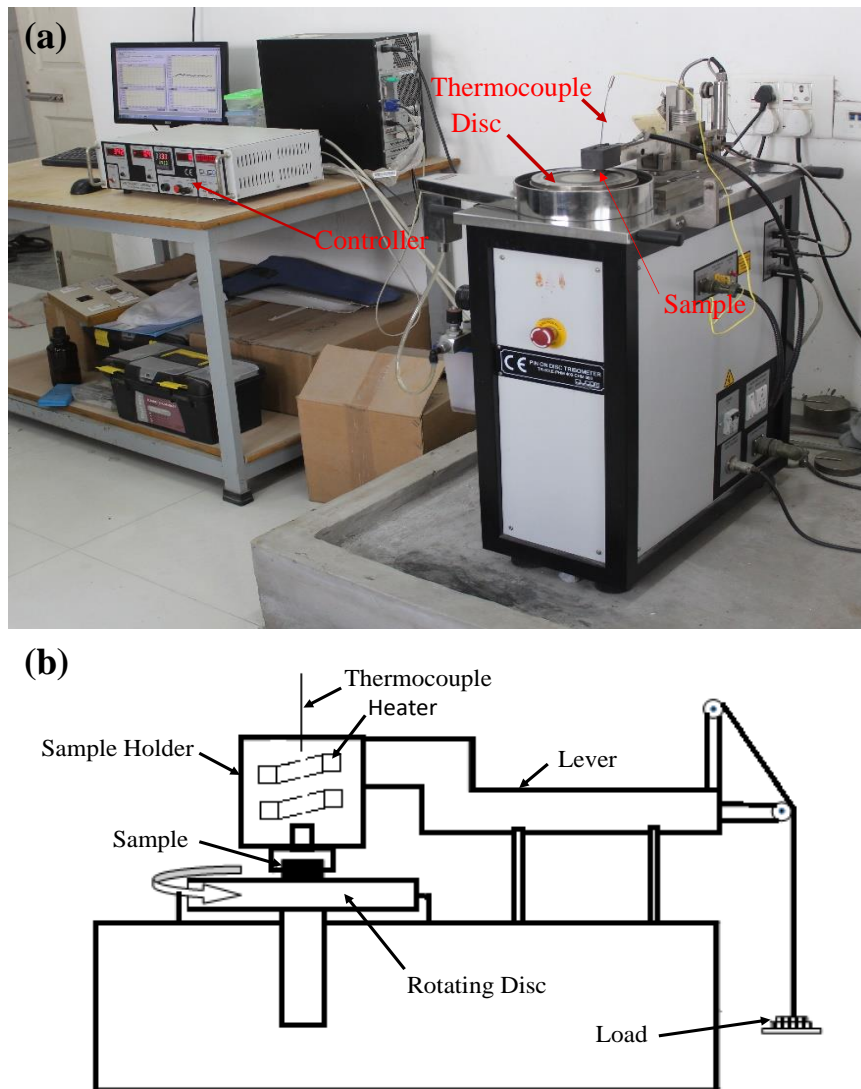


Figure 2.16 (a) Pin on disc tribometer setup (b) schematic representation of the test setup.

## 2.18 Summary

Metal injection moulding, a recent development of the conventional powder metallurgy process, is capable to produce parts which can be used as tools for reproduction technologies. The experimental equipment's used for MIM process involved compounding, mixing, moulding and sintering furnaces. For the debinding process the solvent are used for extracting the binder. The characterization techniques used for analysis of microstructural features, mechanical properties and tribological behaviour of the MIM composites used in the present work.

## CHAPTER 3

### 3 RESULTS AND DISCUSSION

In this chapter, relevant experimental results obtained from the metal injection moulding was discussed. This chapter is divided into four parts. The first part contains the results of characterization of feedstock. The second and third part contains results of debinding and sintering (conventional and microwave) of MIM samples of material systems  $\text{Cr}_3\text{C}_2\text{-NiCr+NiCrSiB}$ ,  $\text{SS316L+WC-CrC-Ni}$  and Tool Steel. The last part contains results of high-temperature wear and oxidation behaviour of sintered MIM samples.

#### 3.1 Particle size and shape

Characterization of particle size and shape of feedstock powder is very important for successful processing through MIM with critical powder loading. The critical loading is the point where all the particles are tightly packed and all voids between the particles are filled with the binder (Shengjie et al.,2016). An increase in particle size distribution width increases critical powder loading and irregular powder particle shape decreases critical powder loading (Rajabi et al.,2012). The irregular particle shape increases compact strength after removal of binder in debinding stage due to more interparticle friction but decreases the packing density. This results in increased viscosity during moulding and lowers the final density after sintering. On the other hand, spherical shape particle improves packing density, lowers the viscosity of feedstock during moulding as well as improves the final density of green compact. The spherical shape particle increases density after sintering compared to irregular shape powder. The optimal MIM powder should not be spherical in shape and should not be too much irregular.

The volume distribution plots of powders are shown in Figure 3.1. The material system of powders of  $\text{Cr}_3\text{C}_2\text{-NiCr+NiCrSiB}$ ,  $\text{SS316L+WC-CrC-Ni}$  and Tool Steel respectively. Table 3.1 shows metal powder particle size distribution. Figure 3.2 show the morphology of material system 1. The powder  $\text{Cr}_3\text{C}_2\text{-NiCr}$  irregular shape and  $\text{NiCrSiB}$  completely spherical as shown in Figure 3.2 (a-b) respectively. The powder mixture of  $\text{Cr}_3\text{C}_2\text{-NiCr + NiCrSiB}$  system 1 is shown in Figure 3.2(c)

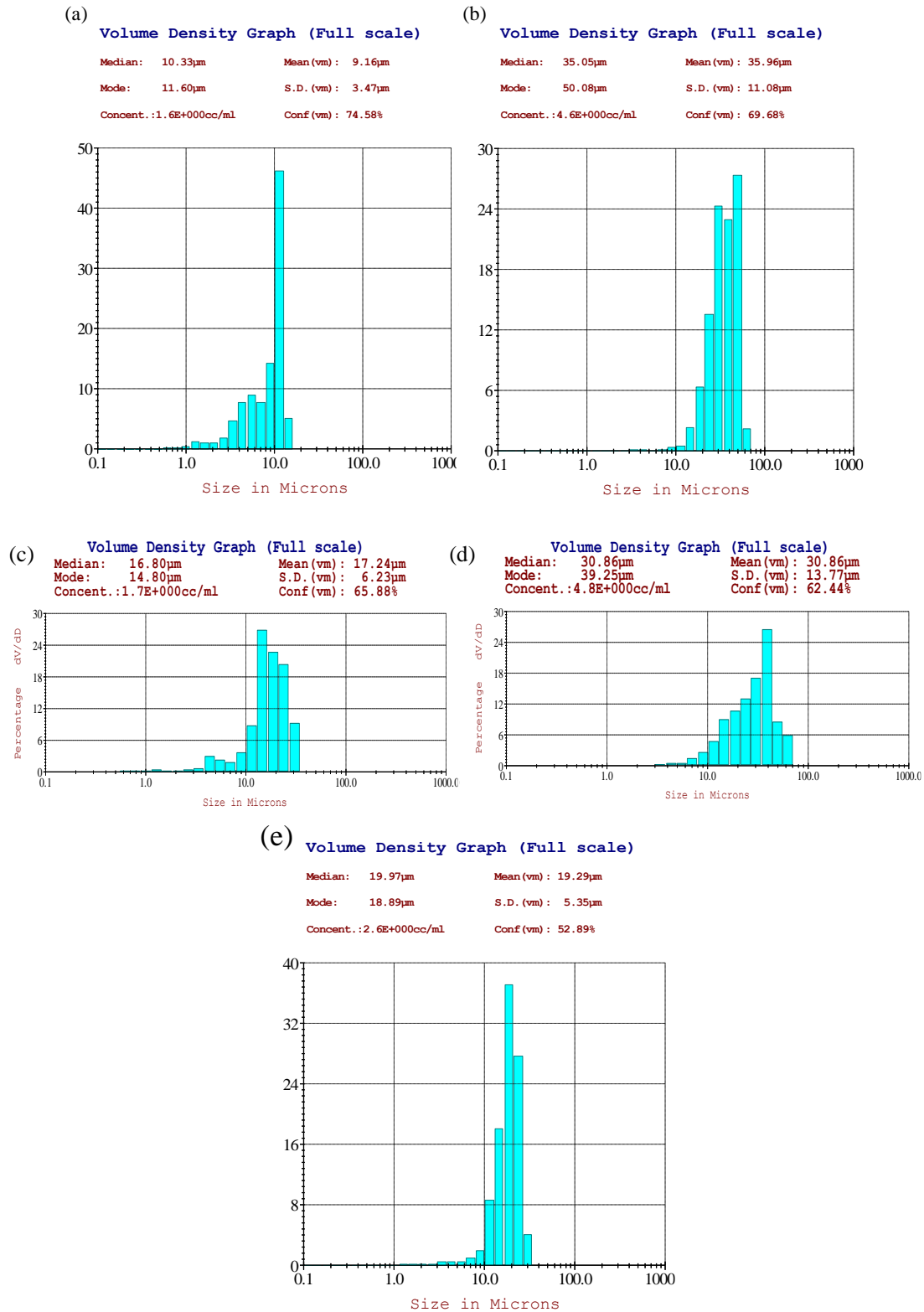


Figure 3.1 Metal particle distribution graph a) SS316L ,b) WC-CrC-Ni, c) Cr<sub>3</sub>C<sub>2</sub>-NiCr, d)Tool Steel e) NiCrSiB

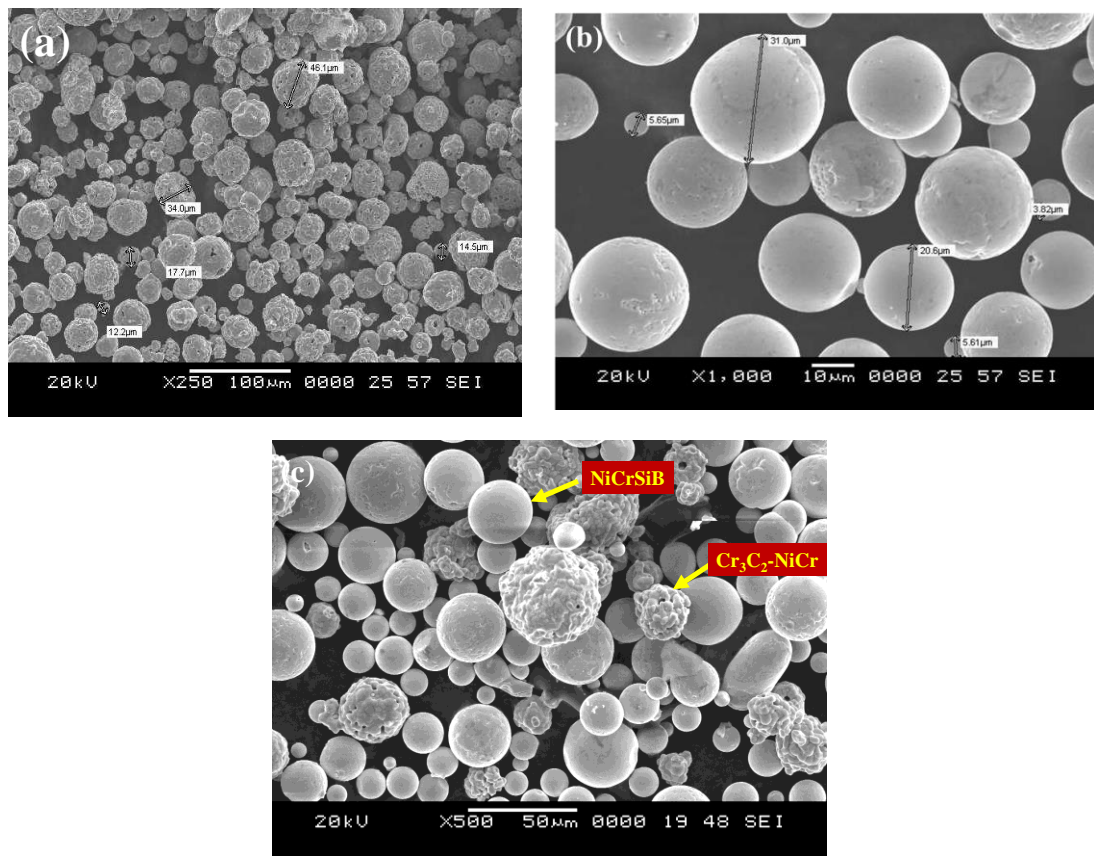


Figure 3.2 SEM micrograph of powder material system 1 a)  $\text{Cr}_3\text{C}_2\text{-NiCr}$  b)  $\text{NiCrSiB}$   
 c)  $\text{Cr}_3\text{C}_2\text{-NiCr} + \text{NiCrSiB}$

Table 3.1 Particle size distributions in ( $\mu\text{m}$ )

	Property			
	Particle size distribution ( $\mu\text{m}$ )			
Metal powder	D10( $\mu\text{m}$ )	D50( $\mu\text{m}$ )	D90( $\mu\text{m}$ )	D97( $\mu\text{m}$ )
SS316L	0.45	1.08	3.35	5.85
WC-CrC-Ni	0.42	1.07	17.68	31.56
NiCrSiB	0.36	0.90	3.84	8.48
$\text{Cr}_3\text{C}_2\text{-NiCr}$	0.46	1.10	6.42	16.85
Tool Steel T-15	0.54	1.92	12.91	21.49

Metal powder particle size distributions. The micrographs of selected feedstock metal Powder particle shape analysed through SEM is shown in Figure 3.3 to Figure 3.4. shown the morphology of the material system.

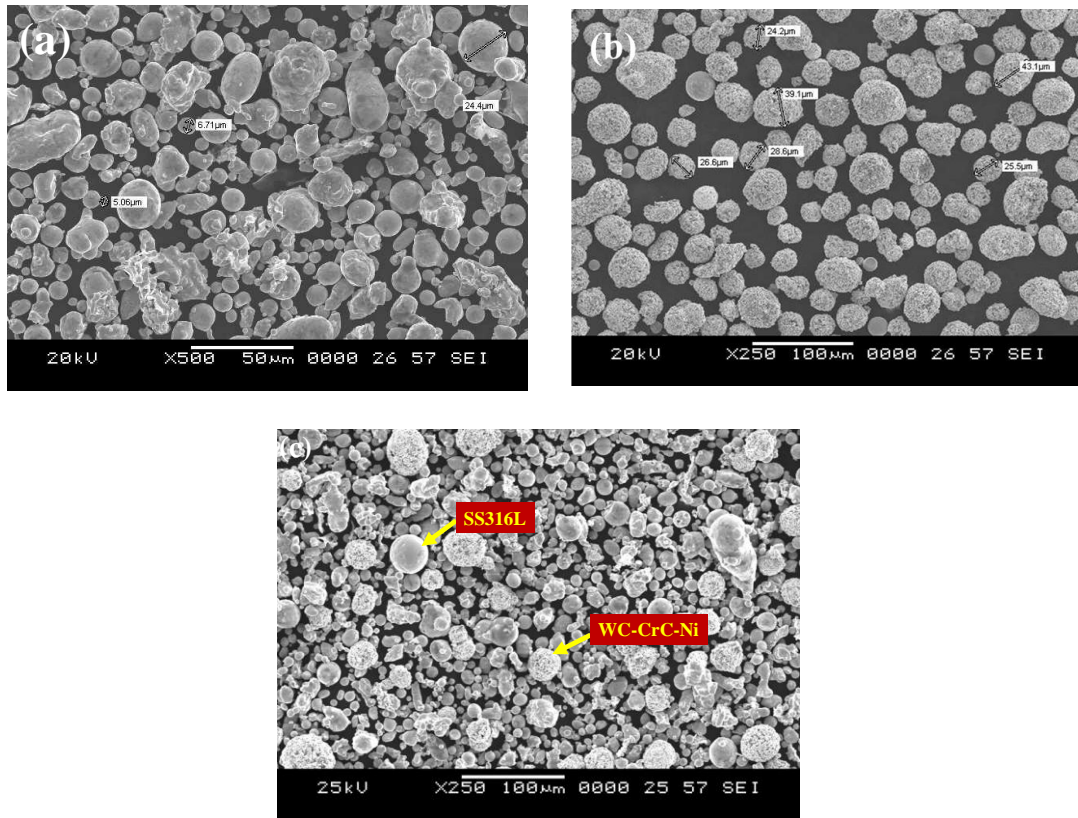


Figure 3.3 SEM micrograph of powder material system 2 a) SS316L b) WC-CrC-Ni  
c) SS316L + WC-CrC-Ni

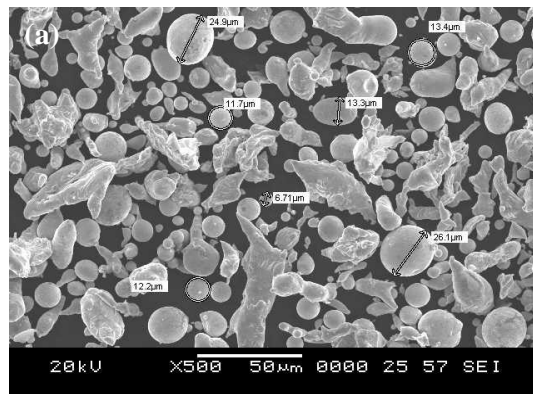


Figure 3.4 SEM micrograph of powder material system 3 a) Tool Steel

### 3.2 Viscosity of Feedstock

The rheological test is utilized to decide the thickness level of feedstock when it goes through a mould opening, and characterizations of feedstock play a vital role in accomplishing noble rheological properties (Meng et al., 2010). The viscosity is the



more important and that should be quantified. If the viscosity is too high, mould filling will be very challenging and sometimes lead to failure of the injection stage. On the other side, low viscosity is tolerable for MIM process which can facilitate filling the whole mould cavity. However, certain significances can be involved by too low viscosity, such as the segregation of powder particle in the feedstock, defects like bend or distortion, fracture and crack during and after the thermal or solvent debinding stage and the uneven shrinkage of the sintered components (Kafkas et al.,2014).

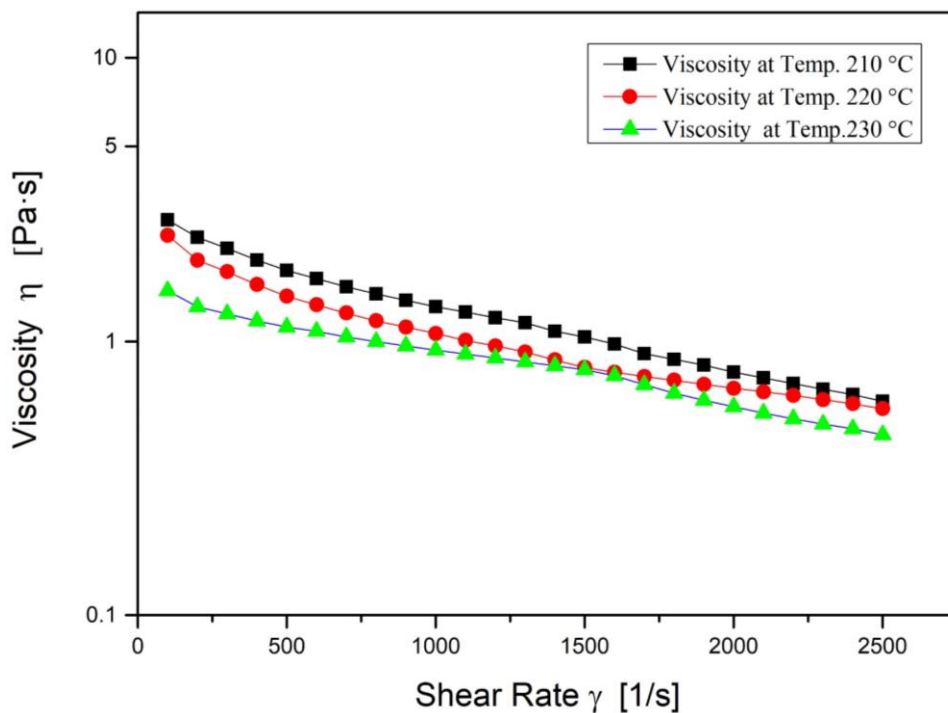


Figure 3.5 The relation between the viscosity of SS316L+WC-CrC-Ni feedstock and shear rate.

In rotational rheometer using a parallel plate geometry, the main factors to be consider while performing measurements, are that very small gaps must be maintained between the parallel plates (on the order of 50 microns) to eliminate initial secondary flows, and the ability to increase and decrease the shear rate quickly to minimize viscous heating (Shu-quan et al.,2007). Rotational viscosimeter (Physica MCR501 Anton Paar, Austria) is used for characterization of metal injection moulding feedstock. The diameter of the capillary plate is 50 mm and the feedstocks are tested at temperature 210, 220 and 230 °C corresponding to the mixing temperature. The relation between the viscosity and shear rate of feedstock used for MIM is shown in Figure 3.5 to Figure 3.7. The plots

show the dependence of viscosity on the shear rate for a feedstock temperature of 210 °C, 220 °C, and 230 °C. The shear rate ranges from 100 to 1000 S<sup>-1</sup> which typically occurs during the injection moulding stage is achieved. It is observed that viscosity decreases with an increase in the shear rate exhibiting to the pseudo-plastic behaviour curves.

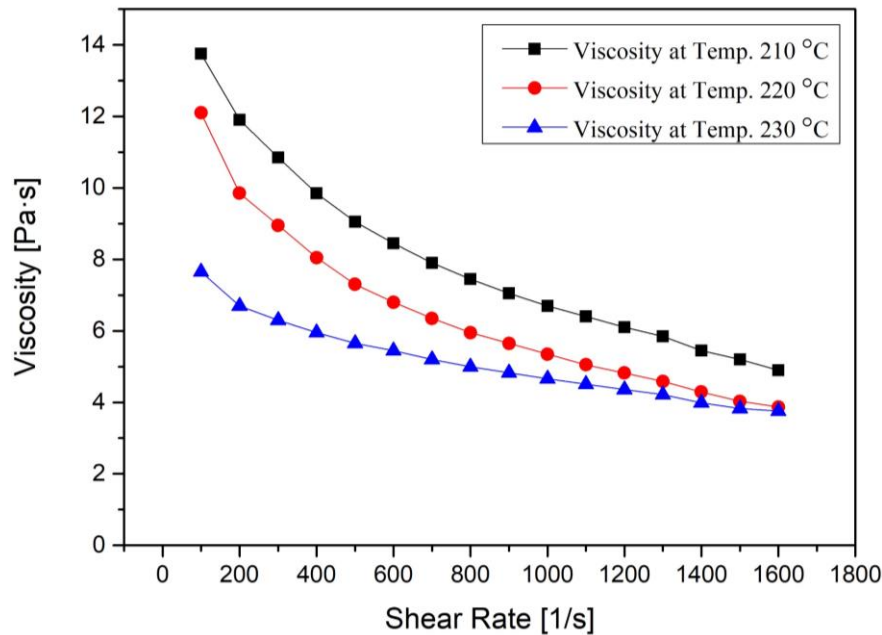


Figure 3.6 The relation between the viscosity of Cr<sub>3</sub>C<sub>2</sub>-NiCr+NiCrSiB feedstock and shear rate.

It is found that a lower shear viscosity was obtained for the 230 °C. Compared with the two other injection temperatures. The viscosity presented in this study is an apparent viscosity. The result shows the viscosity decreased with shear rate, indicating pseudo-plastic properties of the feedstock which is supposed to be suitable for further injection moulding. This kind of flow is important in the actual injection moulding as the feedstock need to flow through the different cross-sectional area in the die cavity. Therefore, lesser viscosity will ease the feedstock to flow to complete the mould cavity. The results showed that the viscosity of Cr<sub>3</sub>C<sub>2</sub>-NiCr+NiCrSiB (medium size powder particle) and Tool Steel T-15 (coarse size powder particle) is more than the SS316L+WC-CrC-Ni (fine size powder particle). This is due to the fact that fine powder contains smaller interstitial spaces than the coarse powder, thus it increases interparticle friction. Besides that, the fine powder has a larger particle surface contact

area between powder particles(German,2008). A sudden viscosity change could cause under stress concentrations in moulded parts, resulting in cracking and distortion (Nor et al.,2009).

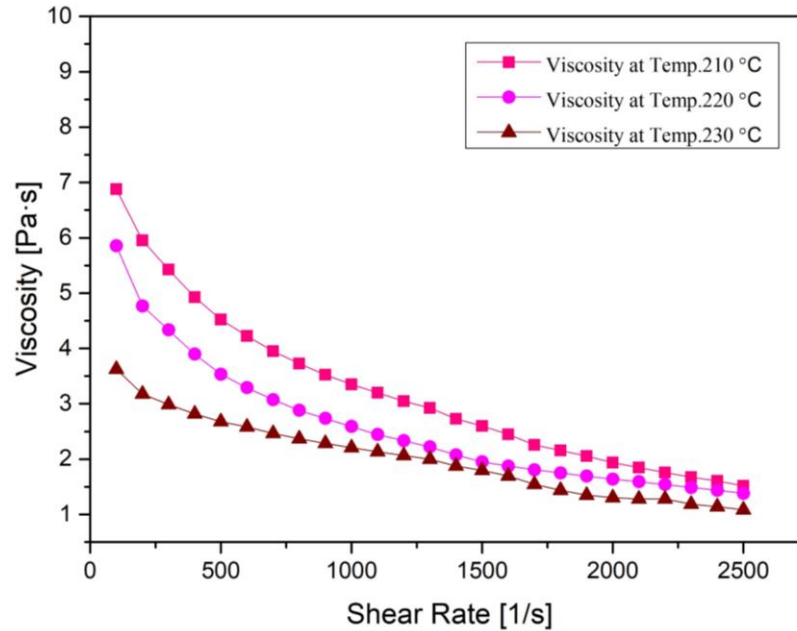


Figure 3.7 The relation between the viscosity of Tool Steel T-15 feedstock and shear rate.

### 3.3 Differential scanning calorimetry (DSC)

Thermal properties of the binder, as well as feedstock, provides the basic guidelines for processing subsequent steps in MIM. DSC provides the information about thermal properties such as melting range, solidification range, of binder and feedstock, in order to observe any temperature shift or possible formation of a new phase as a result of the addition of powder during mixing. Besides that, it is also used as a guide to determine the optimum temperature range for mixing to ensure all of the binders melt during mixing. Figure 3.8 and Figure 3.9 displays DSC results of binder and feedstock. In Figure 3.8 three endothermic peaks are observed at 56 °C, 102 °C and 232 °C during heating cycle due to the melting of major binder constituents.

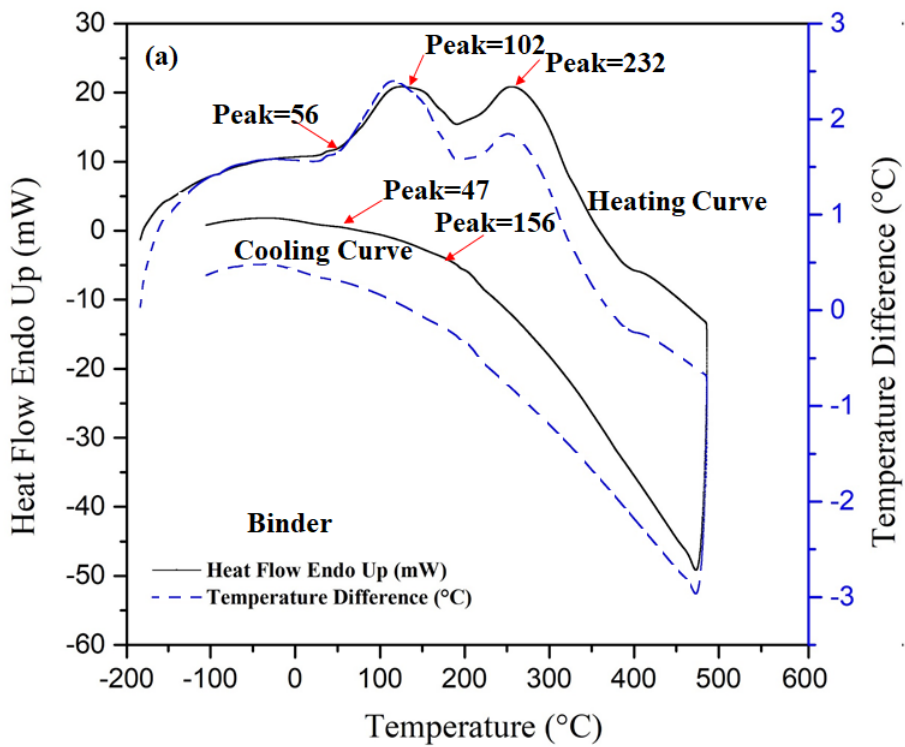


Figure 3.8 DSC plots for the binder

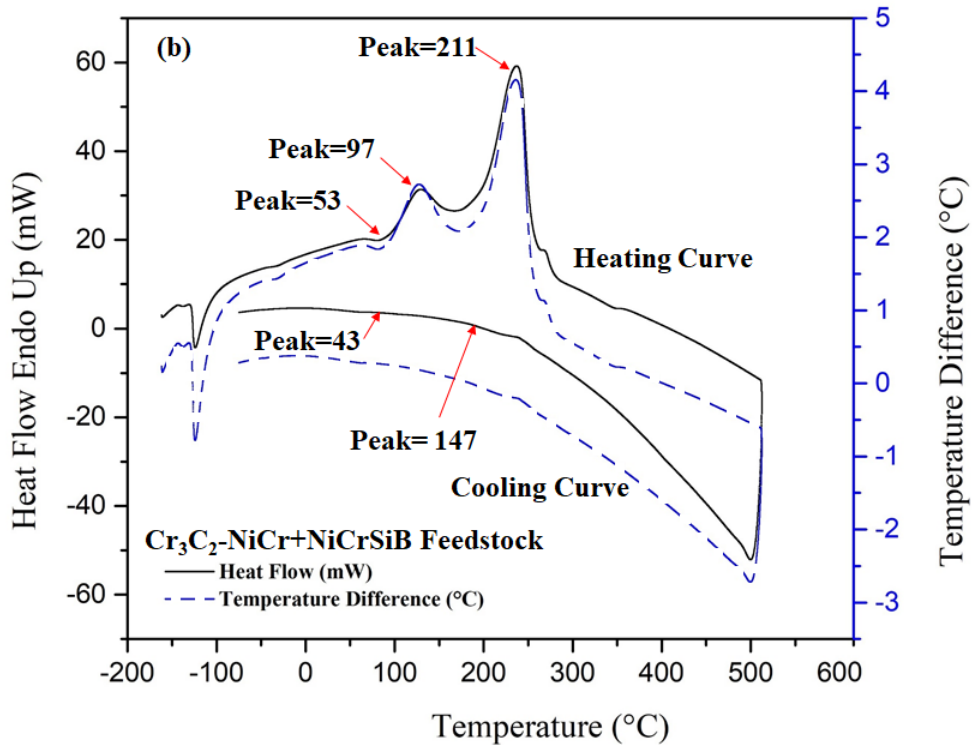


Figure 3.9 DSC plots for  $\text{Cr}_3\text{C}_2\text{-NiCr+NiCrSiB}$  feedstock

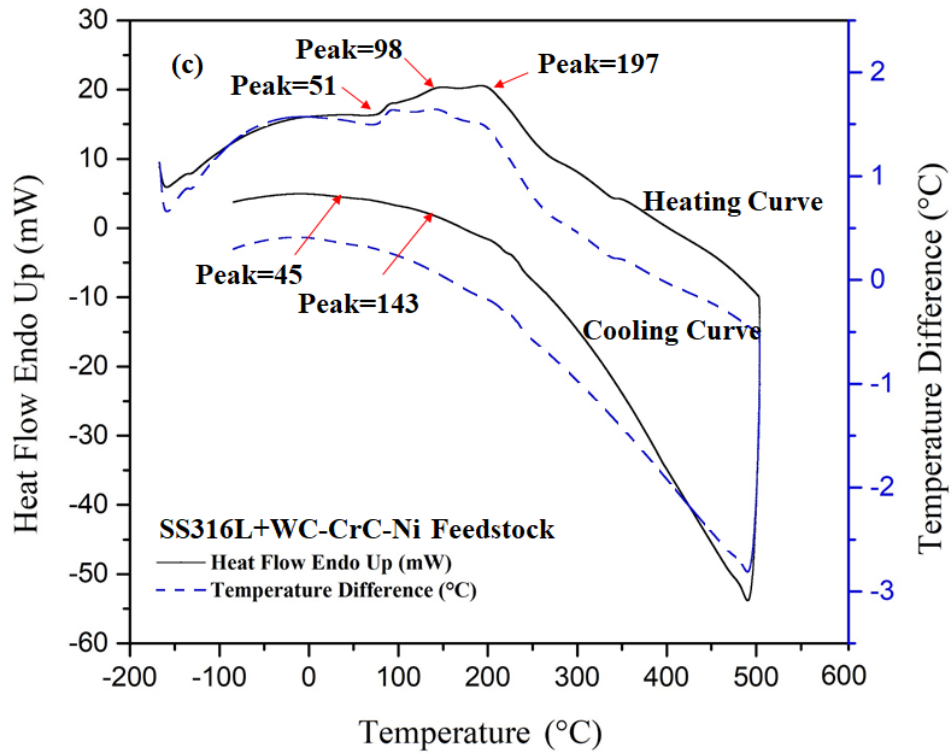


Figure 3.10 DSC plots for SS316L+WC-CrC-Ni Feedstock

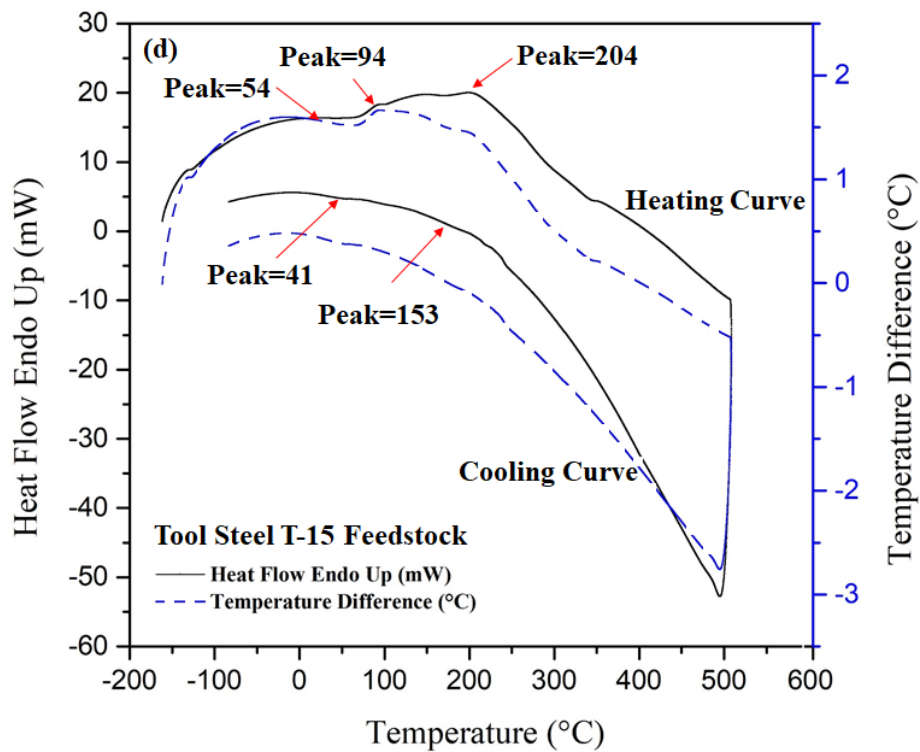


Figure 3.11 DSC plots for Tool Steel T-15 Feedstock

The first and second peak at 56 °C and 102 °C corresponds to the melting of PW, PEG-600 and SA. The third peak at 232 °C corresponds to the melting of LDPE. During

cooling cycle, the cooling curve shows two peaks observed at 156 °C (upper crystallization temperature) and 47°C (lower crystallization temperature) which corresponds to the solidification point of LDPE and other binders (PW, PEG-600, SA) respectively. Similarly, in the case of Cr<sub>3</sub>C<sub>2</sub>-NiCr+NiCrSiB feedstock, the heating curve for the feedstock at 53 °C,97 °C and 211 ° C. as shown in Figure 3.9. In the heating curves for SS316L+WC-CrC-Ni feedstock shows three peaks at 51 ° C, 98 °C and 197 ° C.as shown in Figure 3.10. In Figure 3.11 in heating curves, three peaks show for Tool Steel feedstock at 54 ° C, 94 °C and 204 °C. The heating curve these peaks in the heating cycle corresponding to the melting point of binders (PW, PEG-600, SA) and LDPE. The cooling curves are observed for feedstock material form Figure 3.9-Figure 3.11 at 147,143,153 °C (Upper crystallization temperature) and 43,45,41 °C (lower crystallization temperature) corresponding to the solidification point of LDPE and another binder (PW, PEG-600, SA). The DSC result of binder and feedstock shows that the injection temperature of the feedstock should be above 232 °C and mould temperature should be below 41 °C for successful injection moulding. Feedstock Injection was carried out above 232 °C where binder in the feedstock melts completely. Therefore, DSC cooling curves in

Figure 3.8 to Figure 3.11 is of more interest for the finding solidification range (upper and lower crystallization temperature). It can be seen from the cooling curves of Figure 3.8, Figure 3.9 and Figure 3.11 that upper crystallization temperature and lower crystallization temperature of feedstock decreases compared to that of the binder. The effect of metal powder in the shifting of solidification point is due to the reason that the dispersed metal powder restricts the mobility of binder, thereby restricts further reduction in the size of crystalline domains and reduces solidification points (Adames, 2007).

### **3.4 Thermogravimetric analysis (TGA)**

Thermogravimetric analysis of the feedstock is very useful especially in designing the heating cycle during the debinding process and also to determine the maximum injection temperature and removal of binder in the thermal debinding cycle. Besides that, it is generally used as a guide to know the suitable temperature for the debinding process and maximum limit for metal injection moulding process where the temperature

used must be lower than the degradation temperature. Thermogravimetric analysis of the feedstock was carried out and the TGA curve of feedstock is shown in Figure 3.12 to Figure 3.14. It can be seen from the graphs that weight loss of binder or degradation of binder starts just after 239.7, 234.75 and 241.53 °C. These indicate that the maximum injection temperature should not exceed 239.7, 234.75 and 241.53 °C. During heating beyond these temperature results in, degradation of PW, PEG-600 and SA in the binder, PW, PEG-600 and SA escape from the feedstock causing an amount of 9.75, 4.85 and 7.84 % weight loss of the feedstock. Until reaches 416, 329.90 and 433.10 °C. respectively. Subsequently, LDPE starts evaporating till temperature reaches 479.45, 521.01 and 487.38 °C causing a total weight loss of 12.64, 7.62 and 11.57% in the feedstock respectively. Beyond these temperatures, no loss of weight in the feedstock occurs. The temperature at 479.45, 521.01 and 487.38 °C almost all the binder is removed and hence, the minimum thermal debinding temperature of all feedstock should be 479.45 °C. Therefor thermal debinding was carried out at 500 °C, it is observed after thermal debinding binder materials burn-out, and left the powder on the heating pan without distortion of compact shape.

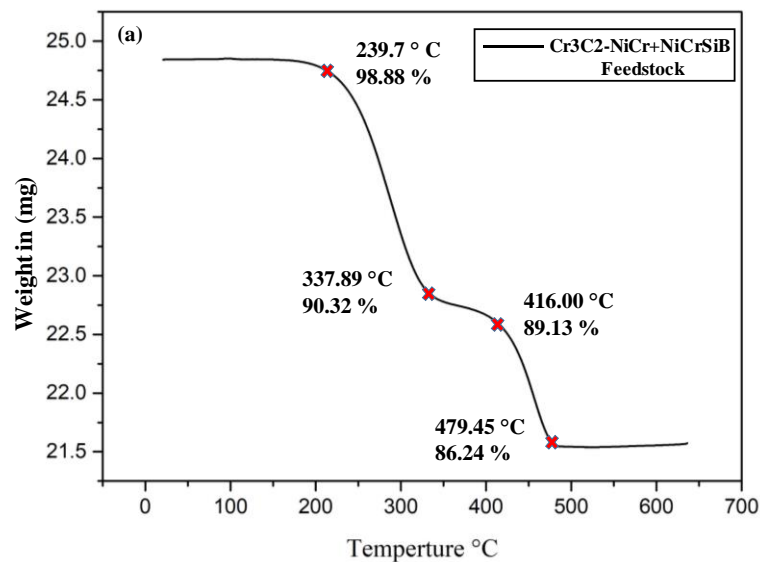


Figure 3.12 TGA Curves for Cr<sub>3</sub>C<sub>2</sub>-NiCr+NiCrSiB feedstock

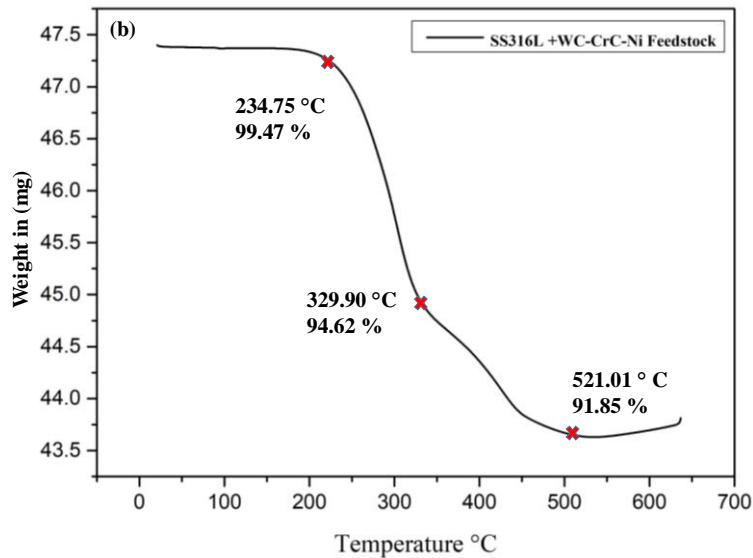


Figure 3.13 TGA Curves for SS316L+WC-CrC-Ni feedstock

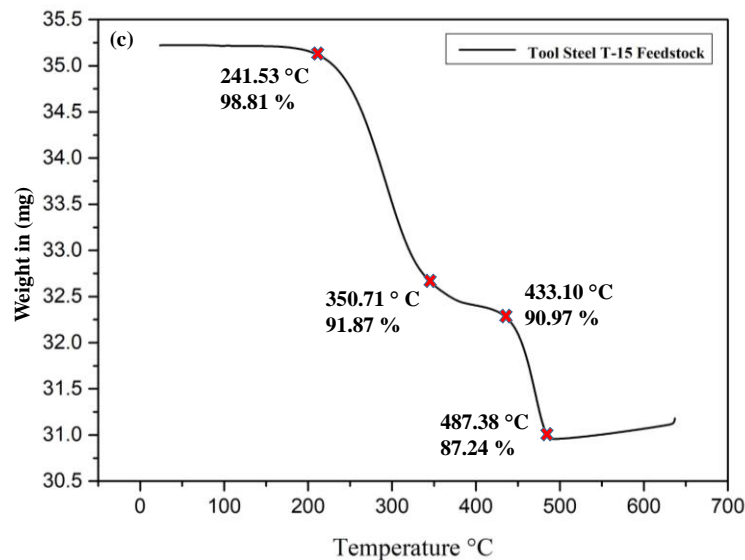


Figure 3.14 TGA Curves for tool steel feedstock

### 3.5 Measurement of density of the feedstock

The density of a material is defined mass per unit volume. It is a measure of how tightly matter is packed together. One of the most common uses of density is how the material interacts with other materials when mixed together such as feedstock (which is a mixture of powder and binder). Densities of binder and feedstock were measured by applying Archimedes Principle, at room temperature. The results of the density measurement of binder and feedstock are given in Table 3.2. The density of the binder was measured by immersing in Acetone (density 0.79 g/cc) and that for feedstock was measured by immersing in water.



Table 3.2 Density measurement of binder and feedstock

SL.No	Material	Average density (g/cc)
1.	Binder	0.930
2.	Cr <sub>3</sub> C <sub>2</sub> -NiCr+NiCrSiB	3.711
3.	SS316L+WC-CrC-Ni	4.791
4	Tool Steel	4.036

### 3.6 Debinding

The binder in the present investigation is composed of PEG- 600, PW, SA and LDPE. Since this is a multi-component binder, binder components are removed in steps. It is necessary to have one of the binder components at least 30 percent or more (Suri et al., 2003, H Abolhasani et al., 2010) in the binder-mix which is to be removed first during debinding to avoid insulated compact of pores. Debinding of the green injection moulded compact was carried out in two steps: solvent debinding followed by thermal debinding. Since PEG 600, PW and SA combined constitute more than 30 per cent and soluble in n-hexane (C<sub>6</sub>H<sub>14</sub>) solvent, hence these constituents were removed from the compact by immersing the compact in n-hexane bath at different temperatures. Figure 3.15 shows that as the temperature and time increases, the rate of removal of PEG 600 increases. This is in good agreement with the published literature(Yang et al.,2003). Due to increased solubility and diffusivity at a higher temperature, more PEG 600, PW and SA dissolve inn-hexane and come out from the compact thereby causing more weight loss. Similarly, it is observed that weight loss increases with increase in time since more binder is available to dissolve PEG 600. as time increases, more time is available to dissolve PEG 600, PW & SA in n-hexane and therefore, weight loss increases.

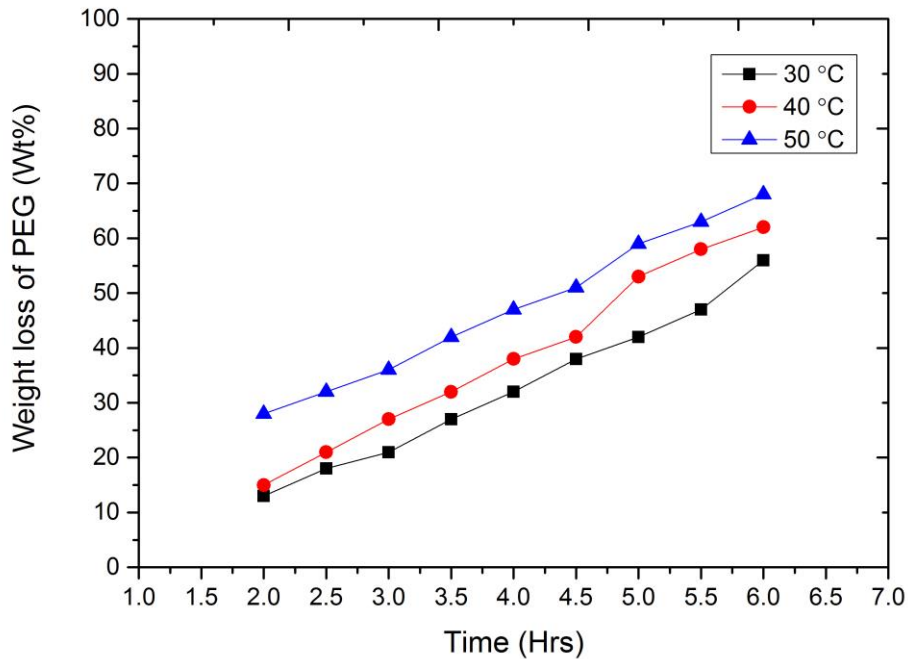


Figure 3.15 Effect of debinding temperature on the weight loss of MIM compact immersed in n-hexane for various extractive times.

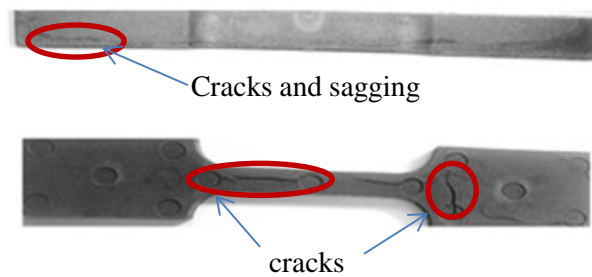


Figure 3.16 Shows the cracks and sagging on compact after debinding.

It is observed that for the case of solvent debinding above 50 °C, cracks are formed in the compact. This is caused by thermal expansion and contraction. As the insoluble backbone binder stay a long time in the n-hexane, it swells and causes expansion (Hwang et al., 2013, Guoxin et al., 2007). At the end of the solvent debinding at higher temperatures when compacts are taken out of the solvent, causes a sharp temperature drop. The sharp drop in temperature causes contraction. The expansion and sudden contraction induce internal stresses in the compact and causes cracking. It is also observed that solvent debinding above 60 °C, results in compact sagging, occurs due to softening of binder component PEG 600, PW and SA. Since cracks and compact

sagging occur above 50° C as shown in Figure 3.16. The solvent debinding compact temperature was selected at 48° C where no crack or distortion was observed in any specimen as shown in Figure 3.17.

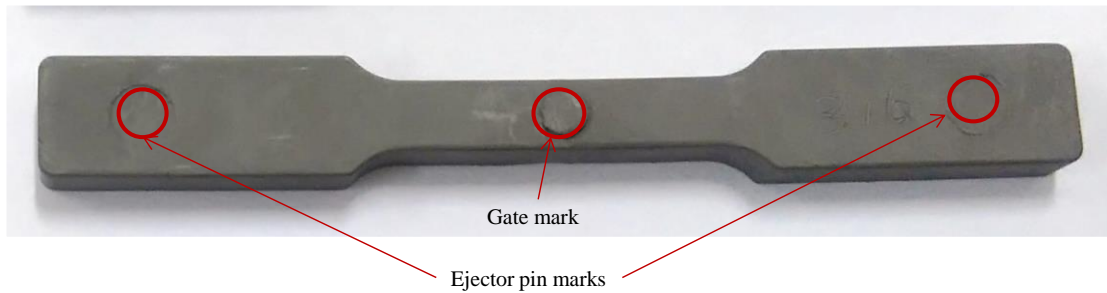


Figure 3.17 Defect-free solvent debonded compact at 48° C.

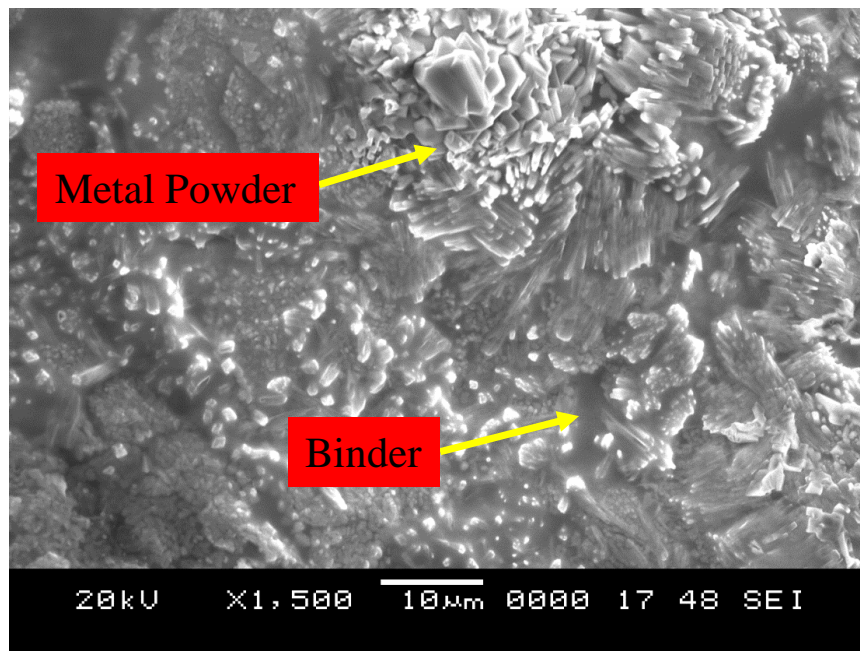


Figure 3.18 Micrograph of injection moulded green compact before debinding.

Solvent debinding was carried out in a view to create interconnected pores or passage through which backbone binder (LDPE) will come out from the compact by evaporation or saturation during thermal debinding and at least 30 % interconnected pores are required to be created by solvent debinding and it is better to have more pores created during solvent debinding for easy removal of backbone binder in thermal debinding. But the creation of more pores means removal of more PEG 600, PW and SA which will be at the cost of compact cracking and sagging as solvent debinding

temperature and time need to be increased. Since at 48° C, around 60 per cent of PEG 600, PW and SA were removed and no problem in thermal debinding of the specimens is encountered, solvent debinding was carried out up to 5 hours. show the micrograph of injection moulded green compact before debinding and after solvent debinding at 48° C for 5 hours. It can be clearly seen in Figure 3.18Figure 3.19 that binder surrounds the powder particles. Due to the removal of most of the major constituent of the binder, powder particles are not fully surrounded by binders. The binder LDPE and remains of PW and SA which have not been removed in solvent debinding.

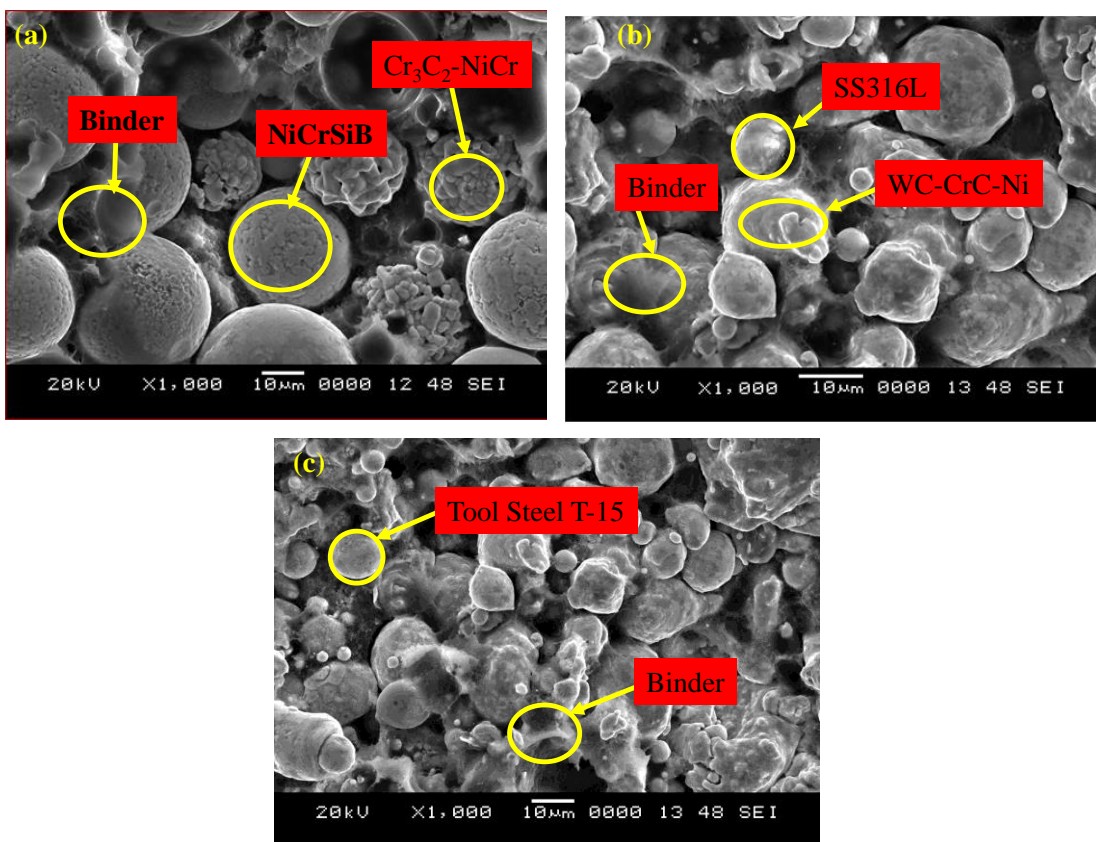


Figure 3.19 SEM Micrograph of the green compact after solvent debinding at 48 °C for 5 hours.

The specimens which are solvent debound at 48° C for 5 hours and thermally debound at different temperature and holding time. Thermal debinding was carried out to remove the backbone binder LDPE and the rest of the PEG 600, PW and SA which remain after solvent debinding. In thermal debinding, LDPE and the rest of the PEG 600, PW and SA evaporate and come out by saturating to the surface thereby to the atmosphere

through the interconnected pores generated by partial removal of PEG 600, PW and SA during solvent debinding.

Figure 3.21 shows the weight loss of the compact on the removal of binder from the compact at different temperatures for a holding time of 5 hours at the respective temperature. It can be observed that weight loss of the compact starts above 232 °C because the rest of the PW and SA start leaving the compact as observed in TG curve of feedstock in Figure 3.12 -Figure 3.14. In the temperature range, 239.7 - 337.89 °C, 234.75 -329.90 °C, 241.53-433.10°C PW and SA evaporate but LDPE does not.

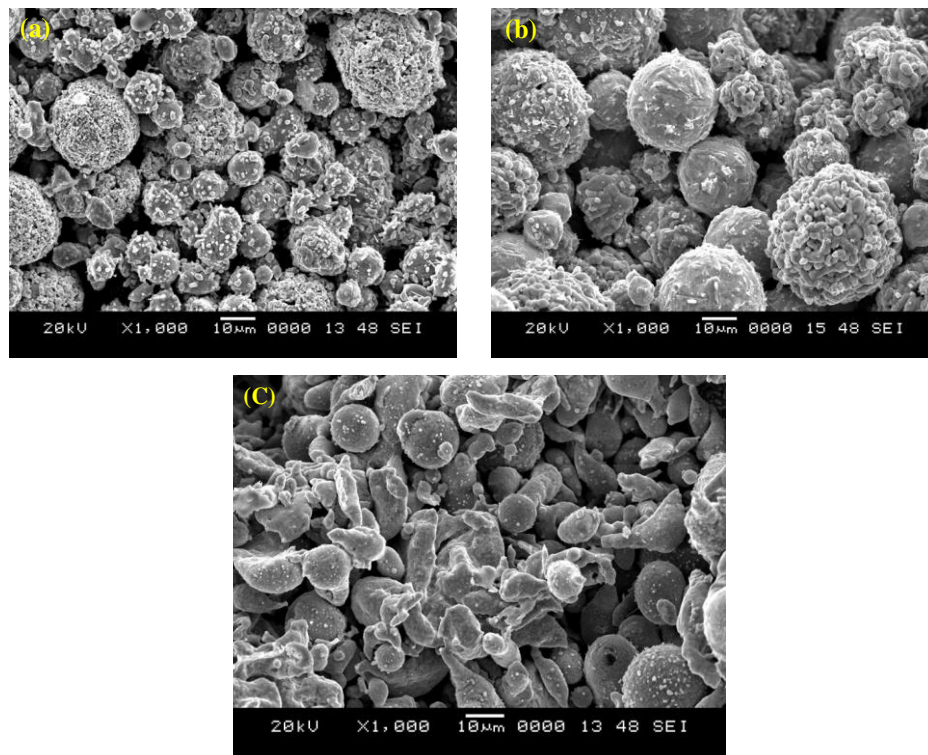


Figure 3.20 shows the SEM Micrograph of a specimen after thermal debinding.

a) SS316L+WC-CrC-Ni b)Cr<sub>3</sub>C<sub>2</sub>-NiCr+NiCrSiB c) Tool Steel –T 15

A major portion of the PW and SA leave the compact during solvent debinding. As the temperature approaches 337.89, 329.90,433.10 °C almost all PW and SA are removed and almost no PW &SA left to be removed as temperature approaches 337.89, 329.90,433.10 °C. Therefore, the rate of binder removal becomes almost constant in the temperature range of 337.89 - 479.45 °C, 329.90 - 521.01 °C, 433.10 - 487.38 °C. Above 337.89, 329.90 and 433.10 °C the rate of binder removal increases rapidly with

the increase in temperature since LDPE starts going out and as the temperature increases, the rate of LDPE removal increases and thereby increasing the weight loss in the compact as evident in TG analysis. The rate of binder removal becomes almost negligible above 500 °C almost no binder left in the compact. Along with the temperature, holding time also plays an important role in selecting a proper debinding cycle. Generally, debinding time depends on the thickness of the green compact and it is proportional to the square of the thickness (Banhart,2001). Figure 3.15 shows the effect of holding time on the weight loss or binder removal of the green compact that is solvent debound at 48 °C for 5 hours and thermally bound at 500 °C. As the holding time increases, the rate of binder removal increases rapidly but beyond 3 hours of holding time, the rate of removal slows down and beyond 5 hours it is almost negligible. It indicates that at temperature 500 °C almost no binder is left after 5 hours of holding time with loosely bounded structure. In this stage, the compact is delicate to handle until sintered.

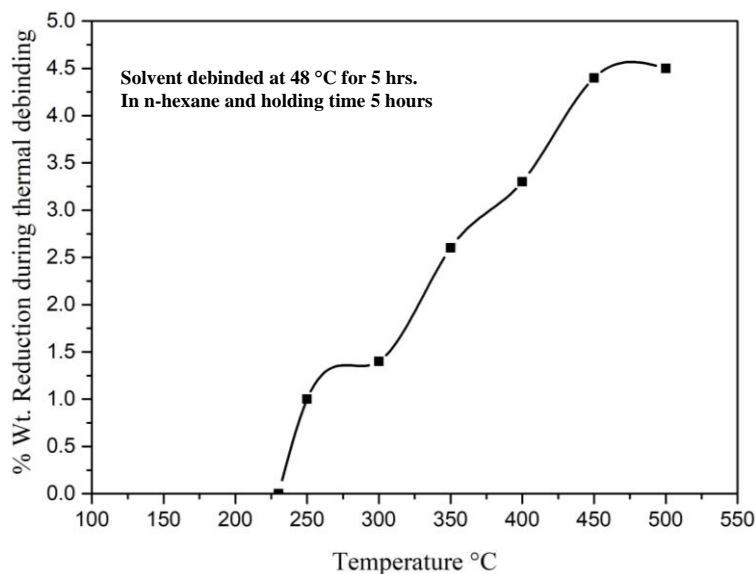


Figure 3.21 Weight reduction of green compact during thermal debinding at different temperatures

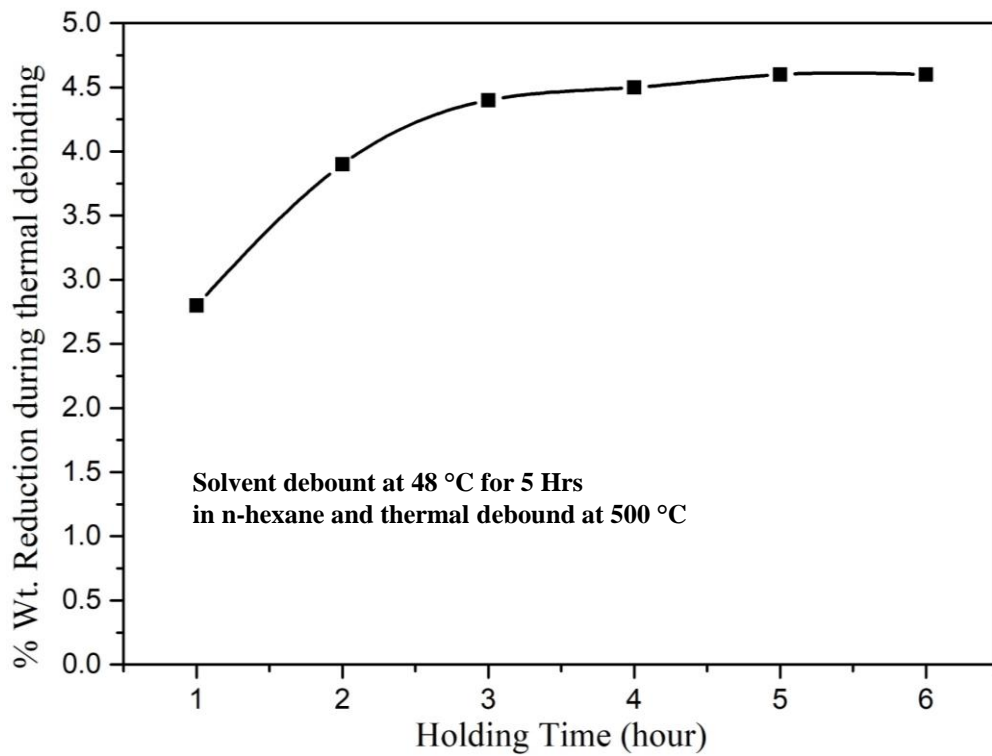


Figure 3.22 Weight reduction of green compact during thermal debinding at a different holding period

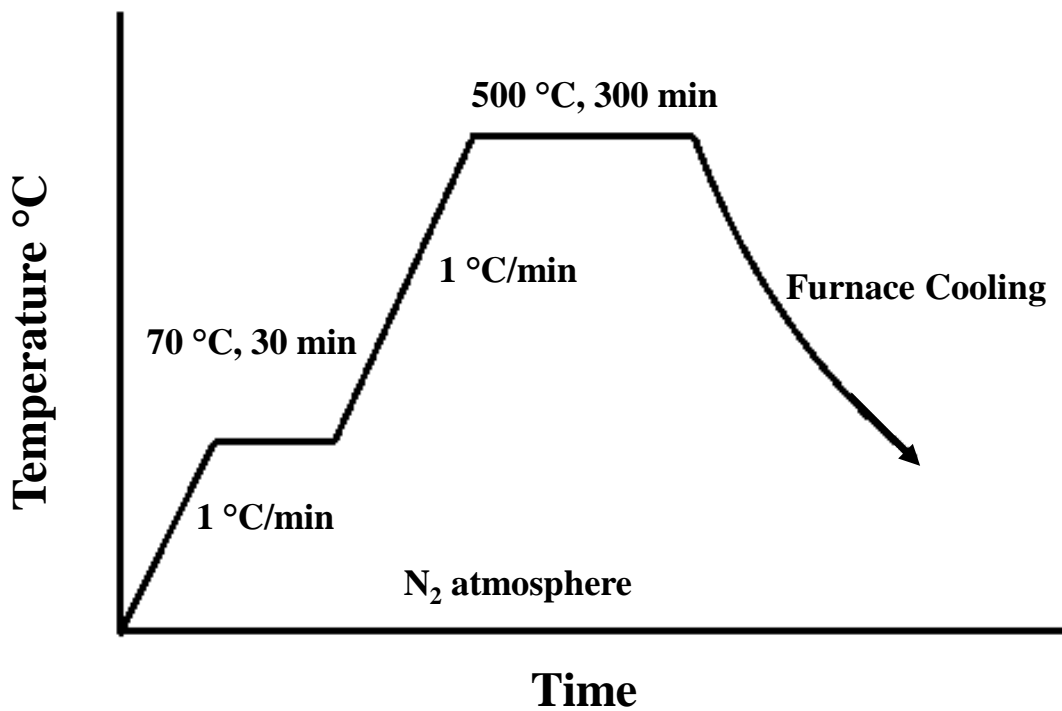


Figure 3.23 Thermal debinding cycle



Figure 3.24 Photograph of thermal debound specimen

Figure 3.23 shows the thermal debinding cycle for the specimens. The very slow heating rate of  $1^{\circ}\text{C}/\text{min}$  is used to allow the binder to evaporate and escape through the micropores created during solvent debinding to avoid cracking or distortion in the compact. Figure 3.24 shows a photograph of a specimen after thermal debinding. From the photograph, it can be observed that no crack or distortion occurred in the specimen.

### 3.7 Conventional Sintering

In the present investigation, thermal debound compacts were sintered. The general observation is that, as the temperature increases, density increases but beyond the formation of the liquid phase, compact shape starts distorting (Xiang-quan et al., 2007). The sintering was carried out at  $1200^{\circ}\text{C}$  and a pure hydrogen atmosphere was used to avoid oxidation.

In the sintering cycle Figure 3.25, the heating rate is varied from 1 to  $5^{\circ}\text{C}/\text{min}$  and also soaking time is allowed to remove remaining binders in the compact and to stabilize the furnace temperature. Initially  $2^{\circ}\text{C}/\text{min}$  constant heating rate maintained up to  $1000^{\circ}\text{C}$  followed by 80 min., 80 min. and 30 min. soaking time at  $250^{\circ}\text{C}$ ,  $400^{\circ}\text{C}$  and  $1000^{\circ}\text{C}$  respectively. In the next stage  $1^{\circ}\text{C}/\text{min}$  heating rate is maintained for densification of tensile specimen till  $1200^{\circ}\text{C}$ , and also  $5^{\circ}\text{C}/\text{min}$  cooling cycle was adopted for  $200^{\circ}\text{C}$  followed by furnace cooling. The importance of cooling cycle is for avoiding distortion in specimen due to a sudden drop in the temperature.



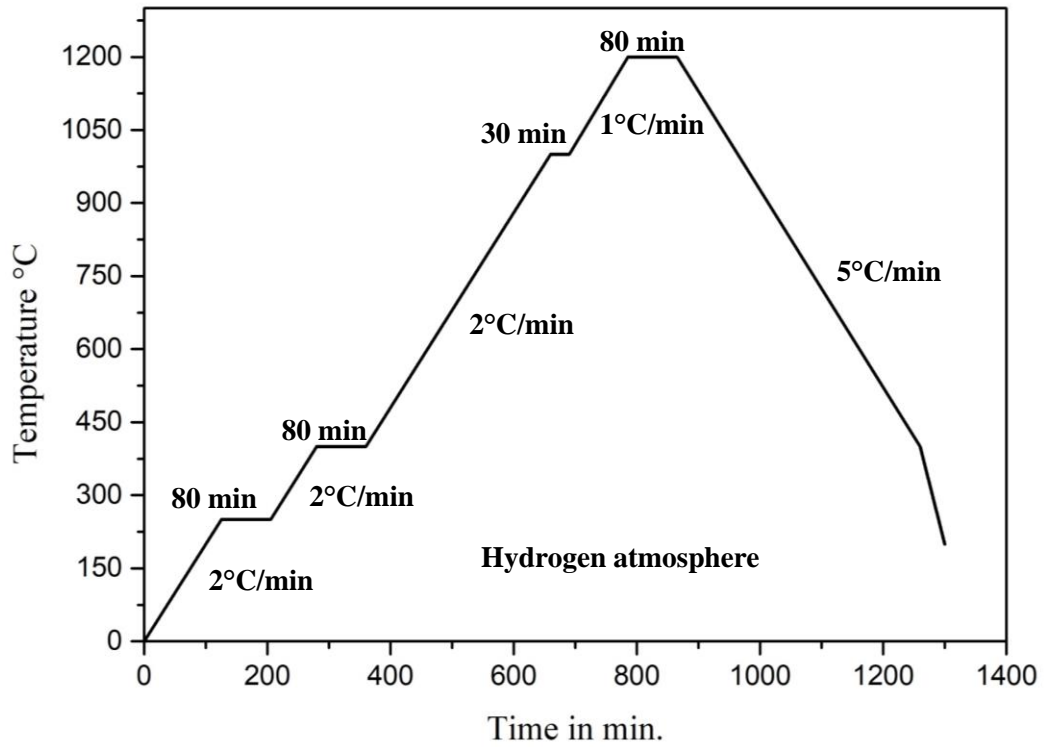


Figure 3.25 Sintering cycle



Figure 3.26 Tensile specimen sintered at 1200 °C

The specimen sintered at 1200 °C is shown in Figure 3.26. It is observed that SS316L+WC-CrC-Ni MIM specimen microstructural Figure 3.27 has characteristic fishbone structure. The microstructure of Cr<sub>3</sub>C<sub>2</sub>-NiCr+NiCrSiB Figure 3.27 (b) shows that powder particles are bound together and isolated pores are separated from the grain boundary.

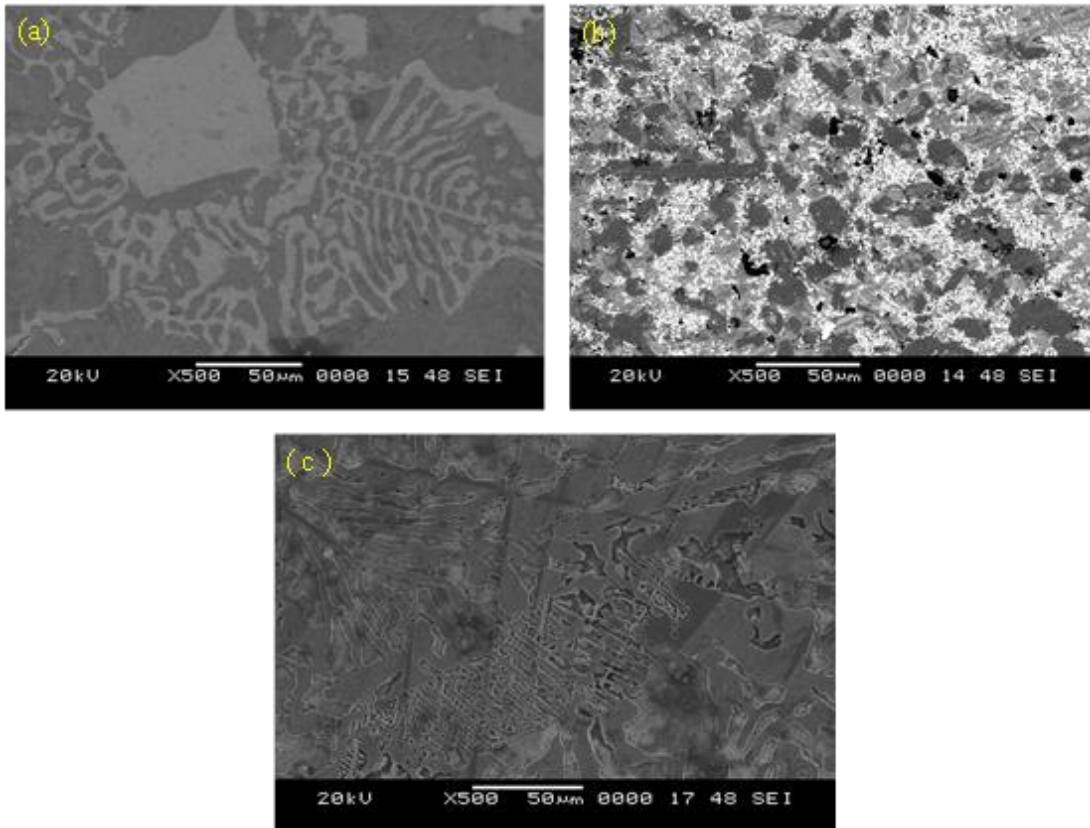


Figure 3.27 Micrograph of the conventionally sintered specimen a) SS316L+WC-CrC-Ni b)Cr<sub>3</sub>C<sub>2</sub>-NiCr+NiCrSiB c) Tool Steel T-15

The microstructure of Tool Steel T-15 Figure 3.27(c) shows a clear sign of the presence of a liquid phase during the sintering cycle appears in the samples, heated up to 1200 °C viewing herringbone morphologies

### 3.8 Microwave sintering of MIM specimen

After successful solvent debinding process, the MIM compacts are subjected to a heating rate at around 100 °C/min till the specimen attain 1200°C. Figure 3.28 shows the microstructure of the sample acquired after a microwave sintering time of 60 min. After 60 minutes of sintering time, there is a greater change in the distribution of grain and associated size from 20 to 40μm. The proportion of large and small grain is not the same and is seen to be different for all the materials.

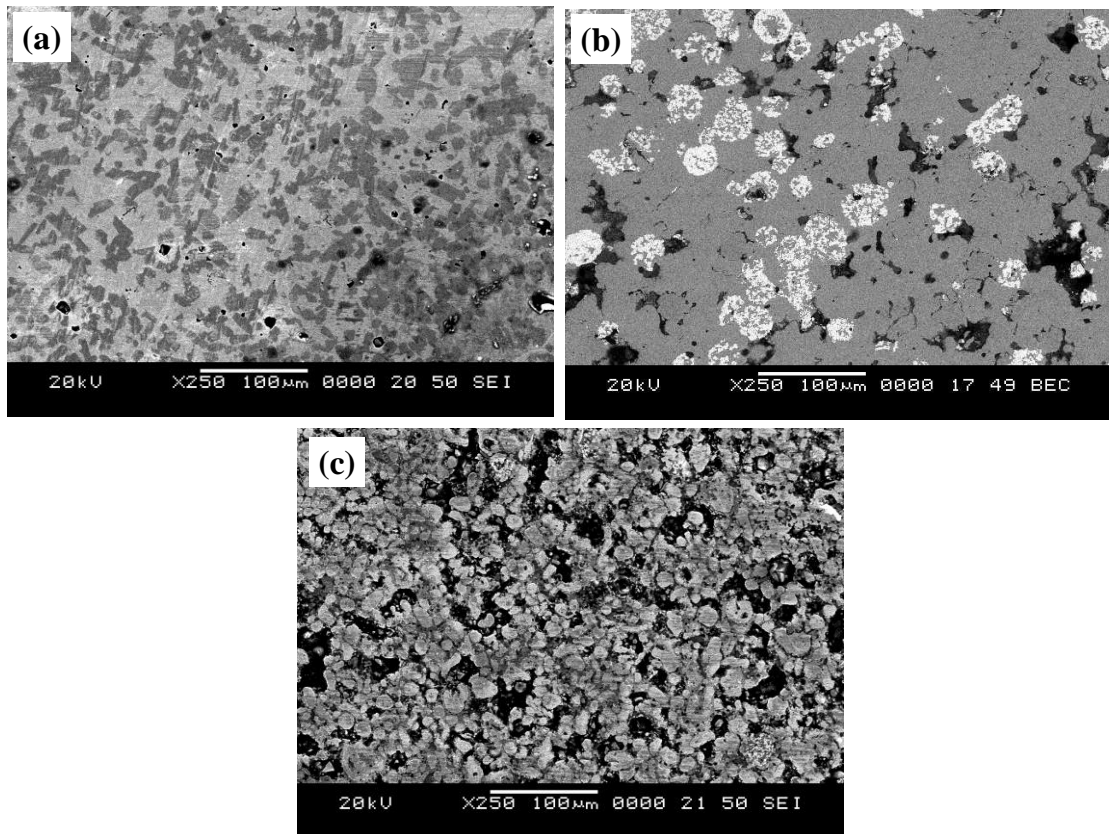


Figure 3.28 Micrograph of the microwave sintered specimen a) SS316L+WC-CrC-Ni  
 b)  $\text{Cr}_3\text{C}_2$ -NiCr+NiCrSiB c) Tool Steel T-15

The observation showed the development of hot points on a few specimens. The development of hot points is due to the attainment of locally and a critical temperature where the material is subjected to. This might occur due to excess energy supplied by the microwaves to the material clarifies this phenomenon.

Following one hour of microwave sintering, the micrographs show there exist more homogeneous grains. A few splits can be seen at first glance. During the debinding stage, an increase in the heating rate tends to deteriorate the shape of parts/specimens. Thereby, when the specimen attained the sintering temperature, the power is expected to keep steady to attain constant temperature. After a few minutes, there is considerably more power is required to attain the utmost of 3kw for the hardware. To complete one hour of sintering time, it was insufficient to continue at this temperature. The obtained porosities explained the impact of sintering time and temperature. Due to the absence

of observed porosities, it was extremely tougher for the microwaves to experience the specimen and considerably higher power was expected to constrain the way or path.

### 3.9 Density, Microhardness and Tensile Strength

The density of the sintered part was measured by the Archimedes immersion method and results are tabulated in Table 3.3. The lower values of density measured with SS316L+WC-CrC-Ni and Tool Steel is due to excessive liquid phase in the powder matrix during sintering at 1200 °C, However, liquid phase in solids will enhance the densification process, but too much liquid will reduce sintered density due to microstructure coarsening (Subuki 2010).

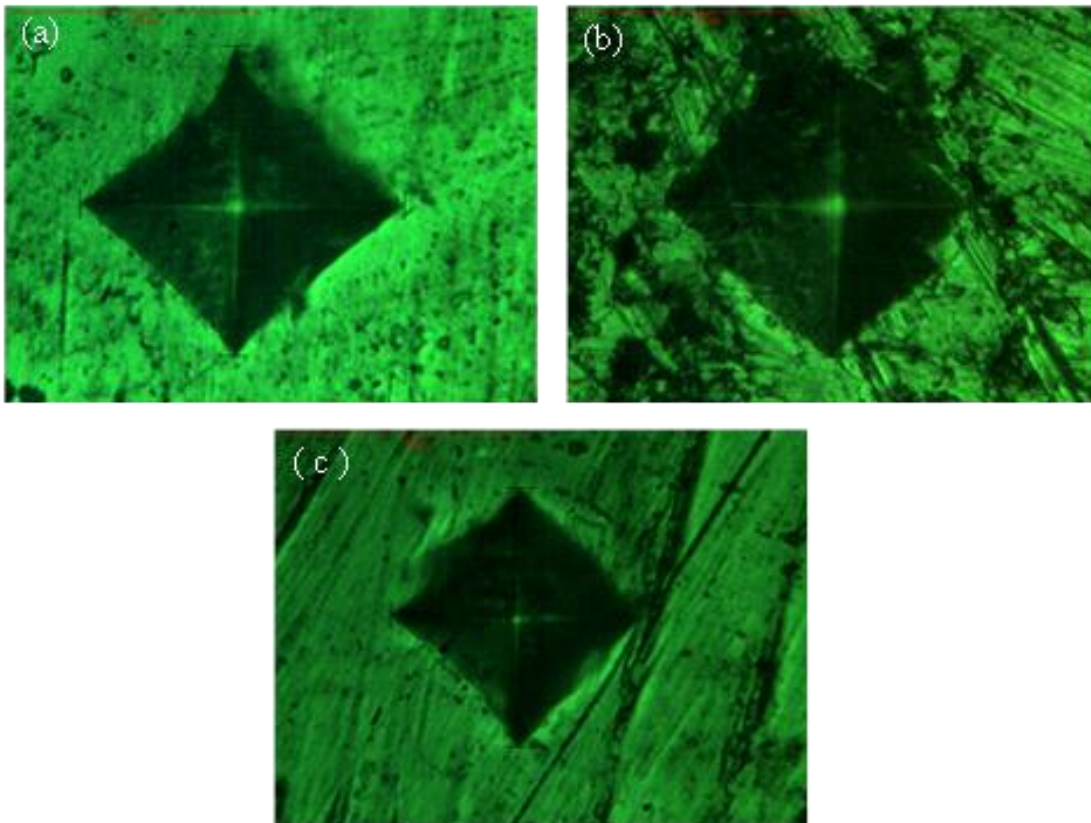


Figure 3.29 Microhardness indentation on a) SS316L+WC-CrC-Ni b) Cr<sub>3</sub>C<sub>2</sub>-NiCr+NiCrSiB, c) Tool Steel –T 15

Particle melting occurs during liquid phase sintering, resulting in a solid-liquid mixture during the thermal cycle. Furthermore, coarse powder compact sintered at a higher

temperature improves its density. This is due to the small surface area that eliminates the liquid phase in the compact (Jamaludin et al.,2009).

Vickers microhardness measurements are conducted on the cross-sectional area of the tensile bar, in the core region. The area was polished, and the microhardness of the sintered part is measured. The average value of microhardness is shown in Table 3.3. An increase in density enhances mechanical properties.

Table 3.3 Mechanical properties of the Conventional sintered MIM specimens

Material	Density (g/cc)		Microhardness (Hv)		UTS (MPa)
	Conventional Sintering	Microwave Sintering	Conventional Sintering	Microwave Sintering	Conventional Sintering
SS316L+WC-CrC-Ni	7.35	7.76	459	463	592
Cr <sub>3</sub> C <sub>2</sub> -NiCr+NiCrSiB	7.72	8.03	712	717	596
Tool Steel –T 15	7.15	7.6	703	707	616

As the specimens are sintered, density increases by the elimination of pores and substantial shrinkage occur in the specimens (Ibrahim et al.,2009). Shrinkage upon sintering of the specimens was measured in lengthwise, widthwise and thickness wise that is, in X, Y and Z direction (Table 3.4). Ideally, shrinkage should be equal in all directions in MIM, but in the present study, shrinkage is different in X, Y, Z direction. This variation of shrinkage may be attributed to the segregation of powder and binder phase in the specimen in the injection stage. Shrinkage variation is more in widthwise direction compared to the length and thickness-wise direction. More segregation of powder and binder phase occurs in the widthwise direction. Tool Steel is showing lower linear shrinkage. The higher powder size results in greater green density, which lowers the linear shrinkage (Onbattuvelli et al., 2013).

The density and hardness of MIM specimens are correlated between the conventional and microwave assisted sintering conditions. Conventionally sintered specimens resulted in comparatively lower density compared to microwave sintering. The higher density in microwave sintering account towards the use of low pressure purged gases

in the microwave chamber, which allows easy escape of binder from the compact. The microwave sintering offers a better hardness compared to conventional methods. Further, quick heating capability at low sintering time offers better grain size as per Hall-Petch effect, i.e. low grain size could always have resulted in better yield pressure abilities (Ferri et al. 2009).

The conventional sintering offers low hardness values due to the influence of two variables. The first might be due to the splits observed on the specimen surface as a result of excessive debinding and hot points framed inside the specimen during the sintering. Microwave sintering is considerably faster. Further, microwave sintering utilizes half of the sintering time compared to conventional sintering method. But with the available microwave sintering facility, there exist a restriction in sintering tensile sample with dimensions as per ASTM standard. The size of samples sintered in a microwave chamber is limited when compared to a conventional sintering method. Hence tensile test results of microwave sintered MIM compacts are not available.

Table 3.4 Linear shrinkage of conventional sintered MIM samples

Material	Length (Shrinkage %)	Width (Shrinkage %)	Thickness (Shrinkage %)
SS316L+WC-CrC-Ni	13.65 to 14.28	15.37 to 16.76	14.68 to 15.89
Cr <sub>3</sub> C <sub>2</sub> -NiCr+NiCrSiB	14.98 to 15.63	16.22 to 17.56	15.43 to 16.73
Tool Steel –T15	12.78 to 13.01	14.22 to 14.86	13.56 to 13.97

### 3.10 Wear Behaviour of Sintered MIM compacts

#### 3.10.1 Cr<sub>3</sub>C<sub>2</sub>-NiCr+NiCrSiB

##### 3.10.1.1 Frictional behaviour

Wear test was conducted at a constant sliding distance of 3000 m at room temperature, 200 °C, 400 °C and 600 °C. Load and temperature have a significant influence on wear loss of the material. Figure 3.30 to Figure 3.33, present typical advancements of the friction coefficient with sliding distance at varying temperature with different normal loading conditions. Three tests were performed for each temperature and load, and an

average friction coefficient was thus calculated within the steady-state system. It is observed that friction coefficient is decreased with increase in temperature and increased with increasing normal load. As the temperature increases, softening of interface material resulting in lower friction coefficient. Friction coefficient registered higher value at 200 °C and lower value at 600 °C.

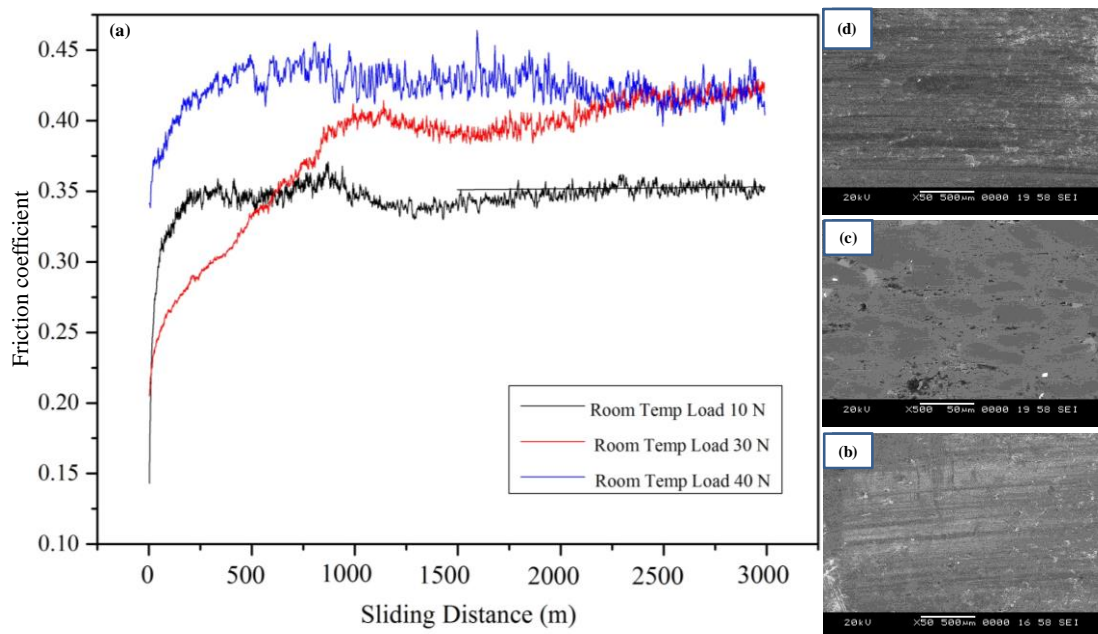


Figure 3.30 (a) Plot of friction coefficient with sliding distance at room temperature and SEM of worn surface of the  $\text{Cr}_3\text{C}_2\text{-NiCr+NiCrSiB}$  composite specimen at room temperature under varying loads of (b) 10 N and (c) 30 N (d) 40 N

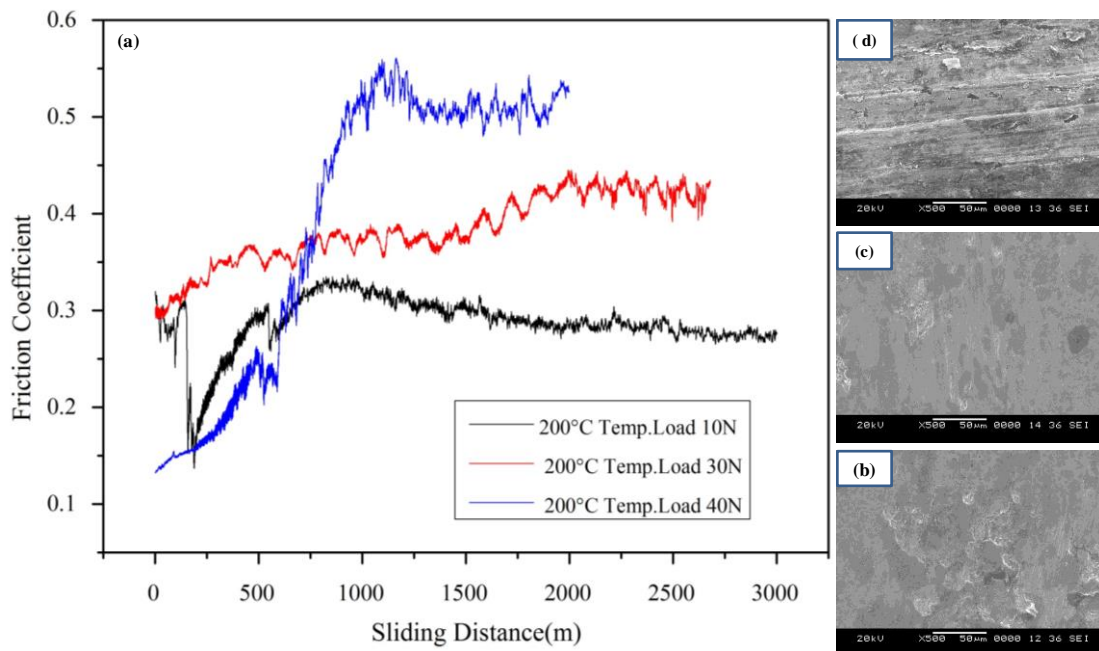


Figure 3.31 (a) Plot of friction coefficient with sliding distance at 200°C and SEM of worn surface of the  $\text{Cr}_3\text{C}_2\text{-NiCr+NiCrSiB}$  composite specimen at 200°C under varying loads of (b) 10 N and (c) 30 N (d) 40 N

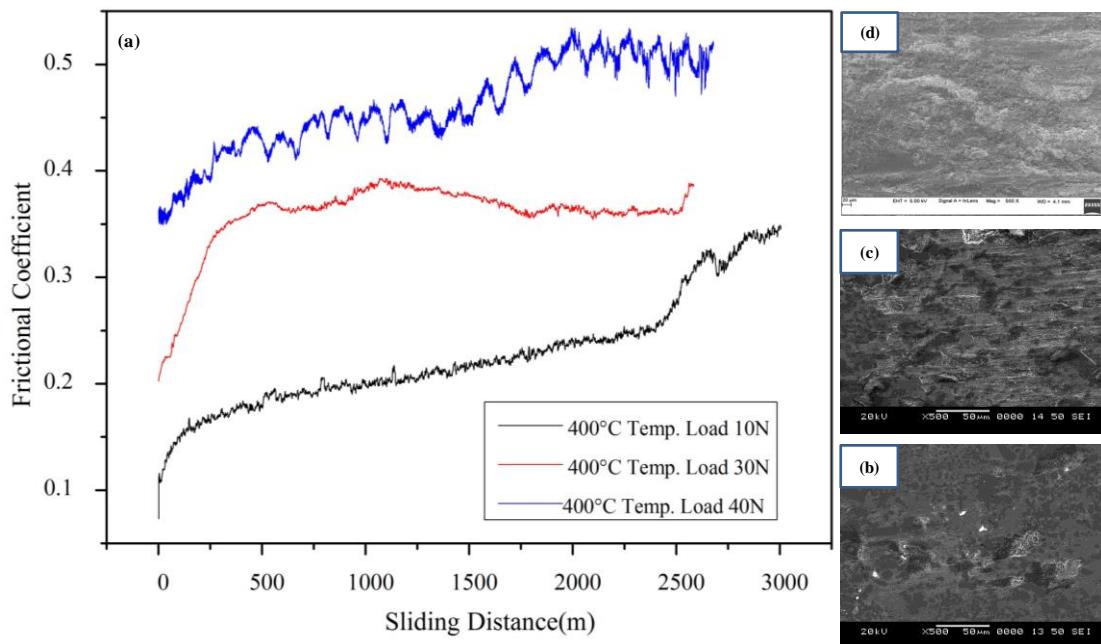


Figure 3.32 (a) Plot of friction coefficient with sliding distance at 400 °C and SEM of worn surface of the  $\text{Cr}_3\text{C}_2\text{-NiCr+NiCrSiB}$  composite specimen at 400 °C under varying loads of (b) 10 N and (c) 30 N (d) 40 N



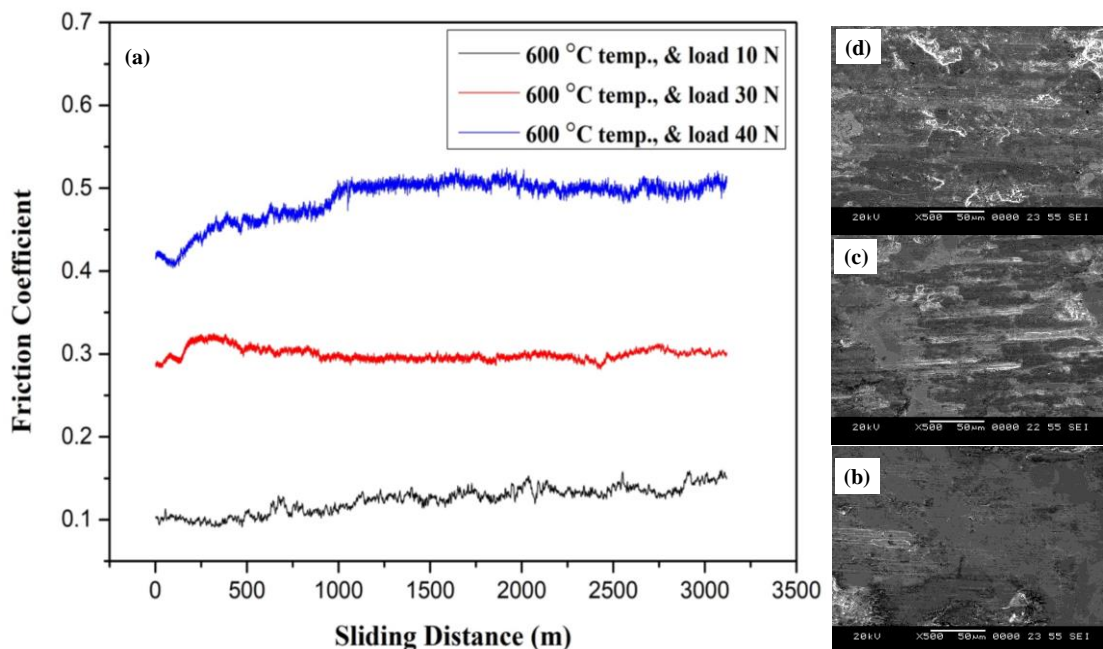


Figure 3.33 (a) Plot of friction coefficient with sliding distance at 600 °C and SEM of worn surface of the Cr<sub>3</sub>C<sub>2</sub>-NiCr+NiCrSiB composite specimen at 600 °C under varying loads of (b) 10 N and (c) 30 N (d) 40 N

### 3.10.1.2 SEM analysis

Worn surface SEM micrographs of the Cr<sub>3</sub>C<sub>2</sub>-NiCr+NiCrSiB at room temperature 200, 400 and 600 °C with 10, 30 and 40 N normal load are presented in Figure 3.30 to Figure 3.33. It can be observed that the worn surfaces with groove and delamination at all the test temperatures. Grooves are formed as a result of ploughing and exhibit plastic deformation of the material. At 400 °C (Figure 3.32c), worn surfaces are seen to be rough with a number of grooves suggesting drastic wear loss. At 600 °C (Figure 3.33 (b-d)), worn surfaces appear to be smooth with minimum grooves implying moderate wear loss. Formation of the oxide layer at an elevated temperature on the contacting surfaces might be the reason for such behaviour at 600 °C.

### 3.10.1.3 XRD analysis

Figure 3.34 displays the XRD pattern of worn surfaces of Cr<sub>3</sub>C<sub>2</sub>-NiCr+NiCrSiB MIM samples tested at Room temperature, 200, 400 and 600 °C.

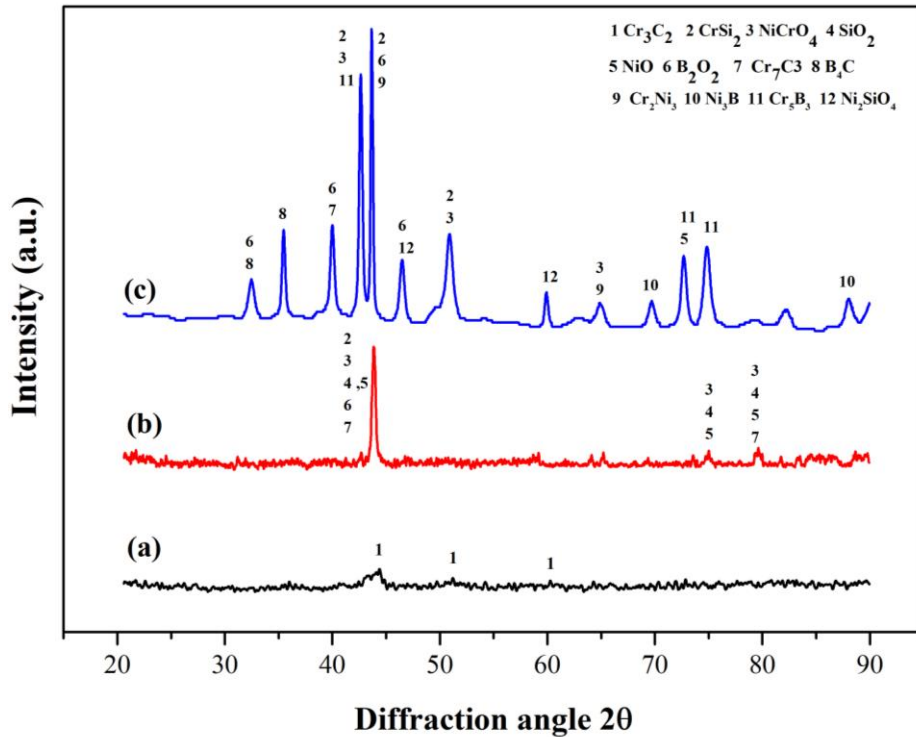


Figure 3.34 XRD pattern of the worn surface of Cr<sub>3</sub>C<sub>2</sub>-NiCr+NiCrSiB at a) room temperature, b) 400 and c) 600 °C.

From

Figure 3.34 it is observed that distinct peaks of Cr<sub>3</sub>C<sub>2</sub>, appear on the worn surfaces at Room temp and B<sub>2</sub>O<sub>2</sub>, SiO<sub>2</sub> peaks appear at 400 °C and 600 °C test temperatures. At 600 °C, distinct Cr<sub>2</sub>Ni<sub>3</sub> peaks are observed along with new phases of Ni<sub>3</sub>B<sub>2</sub> and Cr<sub>5</sub>B<sub>3</sub>. At elevated temperature, Nickel reacts with silicon and oxygen leads to the formation of Nickel silicate and Nickel silicon oxide which are responsible for low coefficient of friction and wear rate at higher temperatures.

### 3.10.1.4 Wear rate

Frictional coefficient and Wear rate of Cr<sub>3</sub>C<sub>2</sub>-NiCr+NiCrSiB at room temp.200, 400 and 600 °C with 10,30 and 40 N normal loads is shown in Figure 3.35. It is observed

that wear rate increase with increasing temperature and found to decrease with increase in load from 30N to 40N.

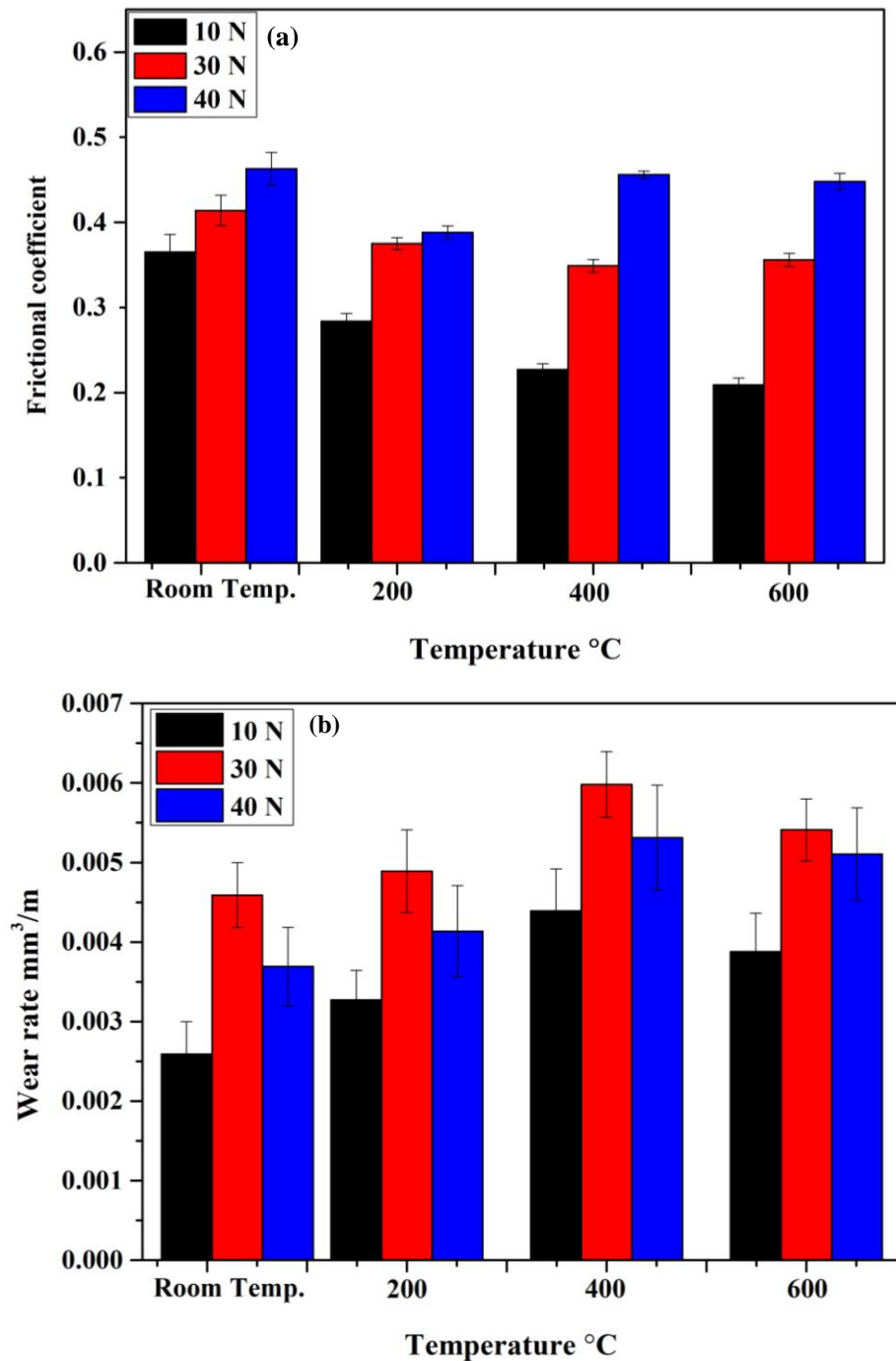


Figure 3.35 Frictional coefficient and wear rate of Cr<sub>3</sub>C<sub>2</sub>-NiCr+NiCrSiB (a) Frictional coefficient v/s Temperature (b) Wear rate v/s Temperature

Wear rate is found to change with temperature variation, minimum at room temperature and maximum at 600 °C. This fact infers temperature rise lowers material hardness that leads to higher wear rate.

According to Archard's wear equation,

$$Q = \frac{KWL}{H} \quad (3)$$

where,  $Q$  - wear volume,  $W$ - load,  $H$ -hardness of material,  $K$ – constant,  $L$  - sliding distance. Wear rate varies inversely with the hardness. As temperature increases, hardness of the material decreases and wear rate increases. The wear rate at 600 °C is slightly reduced owing to the formation of protective oxide film on the surface as observed from XRD( Figure 3.34).

### **3.10.2 SS316L+WC-CrC -Ni**

#### **3.10.2.1 Frictional behaviour**

The friction coefficient of SS316L+WC-CrC-Ni MIM Specimen at room temperature, 200, 400 and 600 °C with 10, 30 and 40 N normal loads is presented in Figure 3.36 to Figure 3.39. Three tests were performed for each temperature and load, and an average friction coefficient was thus calculated from the steady-state system. It is observed that friction coefficient is decreased with the increase in the temperature and increased with increasing load. With respect to temperature, friction coefficient showed higher value at 400 °C and lower value at 600 °C. SS316L+WC-CrC–Ni MIM Specimen exhibited higher friction coefficient as compared to Cr<sub>3</sub>C<sub>2</sub>-NiCr+NiCrSiB MIM specimen. At 40 N normal load, the friction coefficient of SS316L+WC-CrC–Ni and Cr<sub>3</sub>C<sub>2</sub>-NiCr+NiCrSiB are in the range of 0.356-0.543 and 0.388-0.463 respectively. The lower friction coefficient of the SS316L+WC-CrC–Ni MIM Specimen is attributed to lubricity property of FeMo, NiSiO<sub>4</sub> and B<sub>2</sub>O<sub>3</sub> at wide temperature range. At lower temperature, FeMo establishes the lubricating layer between the contacting surfaces thereby lowers the friction coefficient.

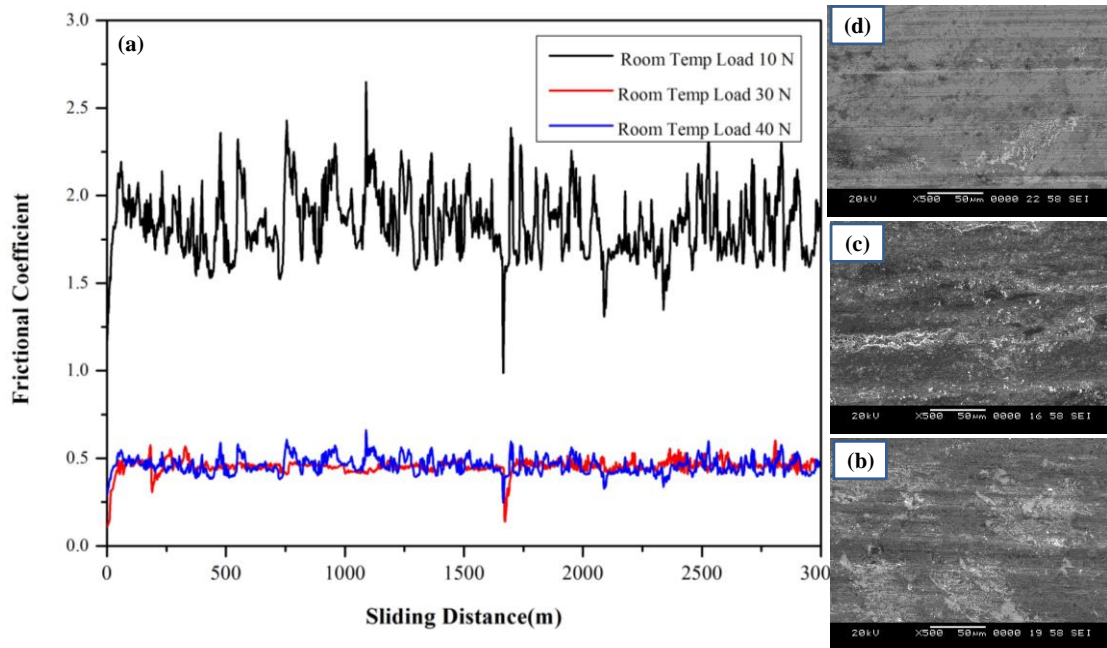


Figure 3.36 (a) Plot of friction coefficient with sliding distance at room temperature and SEM of worn surface of the SS316L+WC CrC-Ni composite specimen at room temperature under varying loads of (b) 10 N and (c) 30 N (d) 40 N

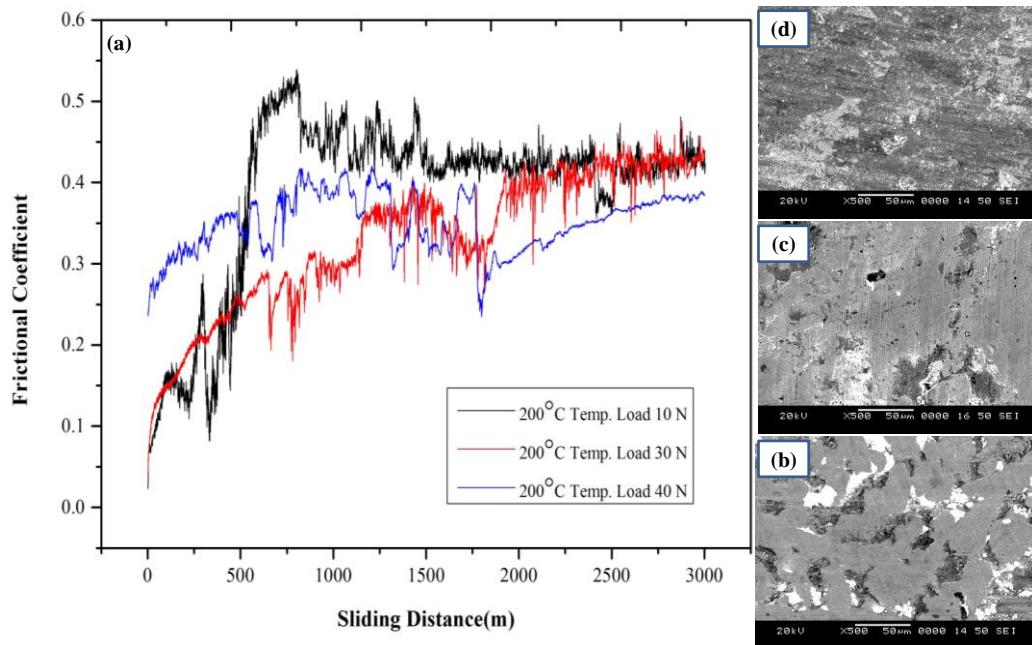


Figure 3.37 (a) Plot of friction coefficient with sliding distance at 200°C and SEM of worn surface of the SS316L+WC CrC-Ni composite specimen at 200°C under varying loads of (b) 10 N and (c) 30 N (d) 40 N

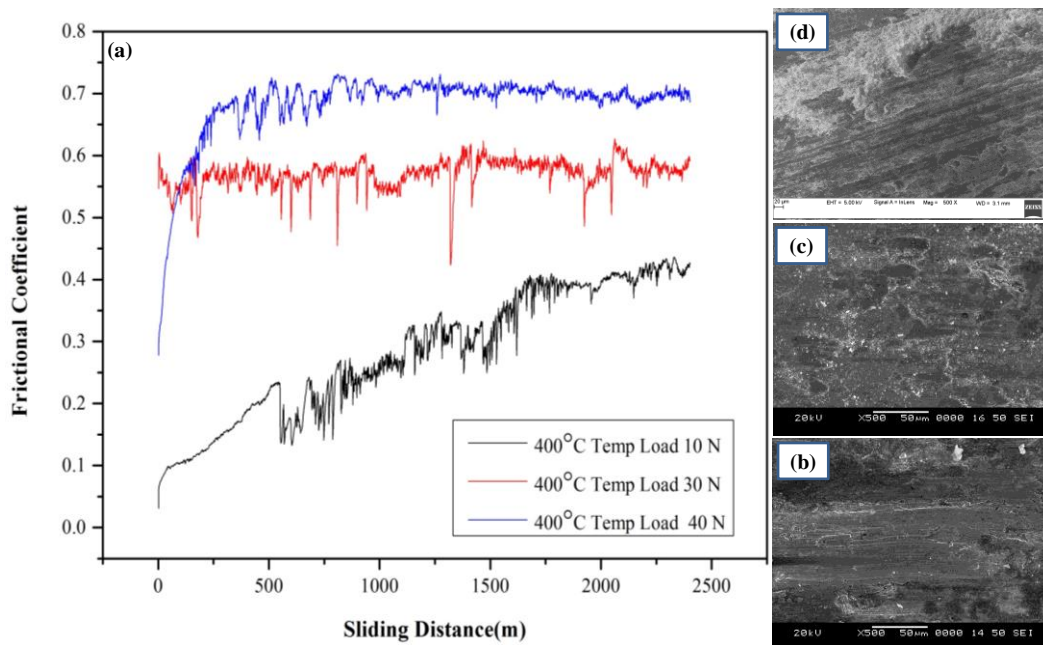


Figure 3.38 (a) Plot of friction coefficient with sliding distance at 400°C and SEM of worn surface of the SS316L+WC CrC-Ni composite specimen at 400°C under varying loads of (b) 10 N and (c) 30 N (d) 40 N

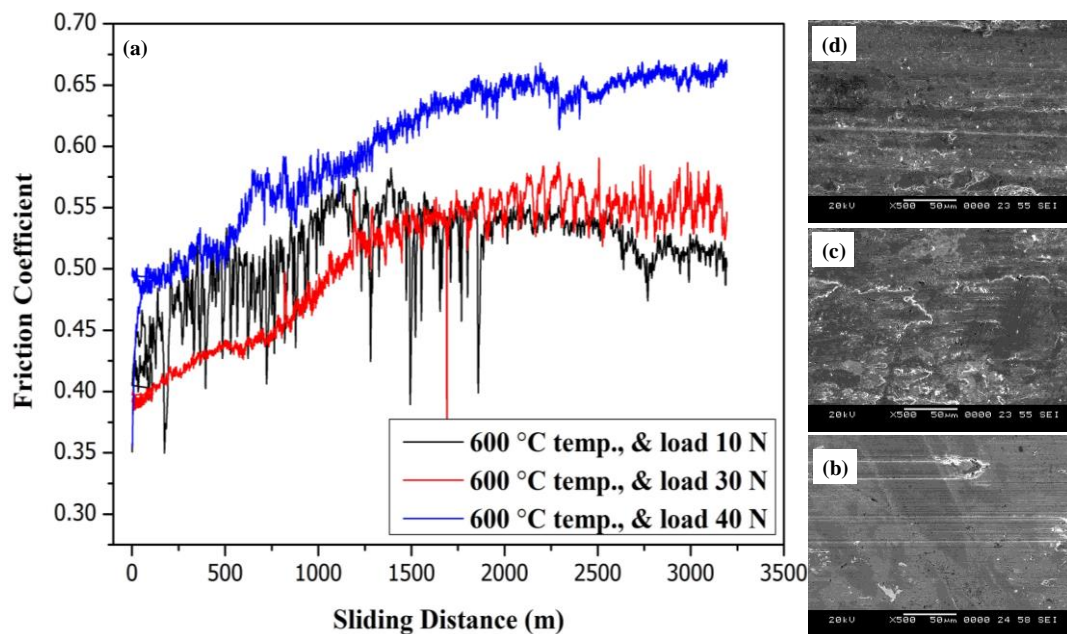


Figure 3.39 (a) Plot of friction coefficient with sliding distance at 600°C and SEM of worn surface of the SS316L+WC CrC-Ni composite specimen at 600°C under varying loads of (b) 10 N and (c) 30 N (d) 40 N

### 3.10.2.2 SEM analysis

Figure 3.36 to Figure 3.39 demonstrates the worn surface SEM micrographs of the SS 316L+ WC-CrC-Ni at 10, 30 and 40 N normal load with room temperature 200, 400 and 600 °C temperatures. It can be observed that the worn surfaces of SS 316L+ WC-CrC-Ni MIM specimen is characterized by a groove, delamination and flaking pits at all the test temperatures Figure 3.37(b-d) indicate ploughing and delamination. From Figure 3.38(c-d) it is noticed that at 400 °C worn surfaces are not smooth and the coating is detached by maximum delamination suggesting severe wear. At 600 °C (Figure 3.39b-d), worn surfaces look like smooth with minimum grooves implying moderate wear loss. Formation of the oxide layer at an elevated temperature on the contacting surfaces might be the reason for lower wear at 600 °C.

### 3.10.2.3 XRD analysis

Figure 3.40 displays the XRD patterns of worn surfaces of SS 316L+ WC-CrC-Ni at room temperature, 400 and 600 °C. XRD graph shows the formation of oxides and

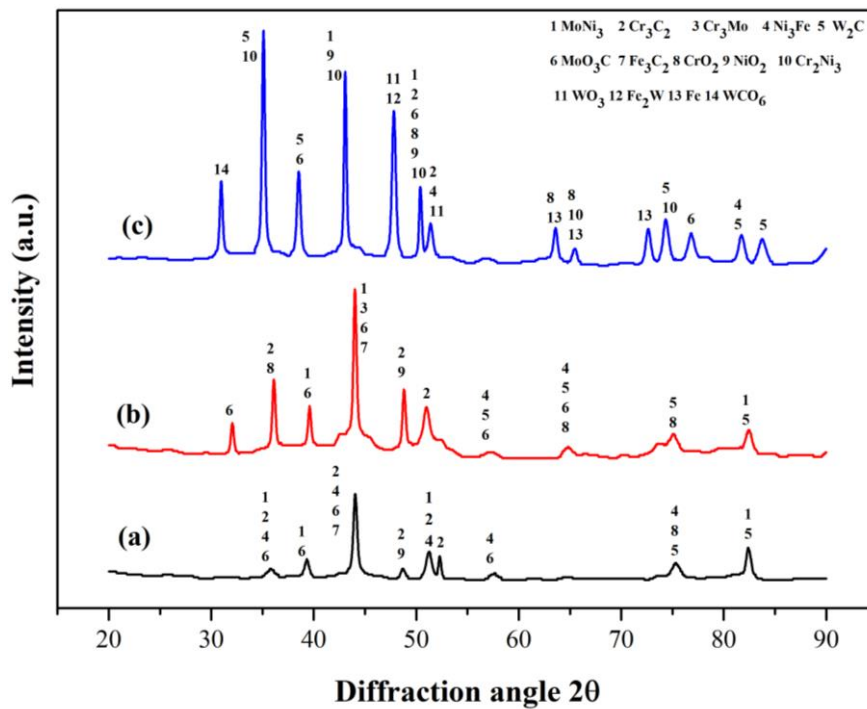


Figure 3.40 XRD pattern of the worn surface of SS316L+WC-CrC-Ni at a) room temperature, b) 400 and c) 600 °C.

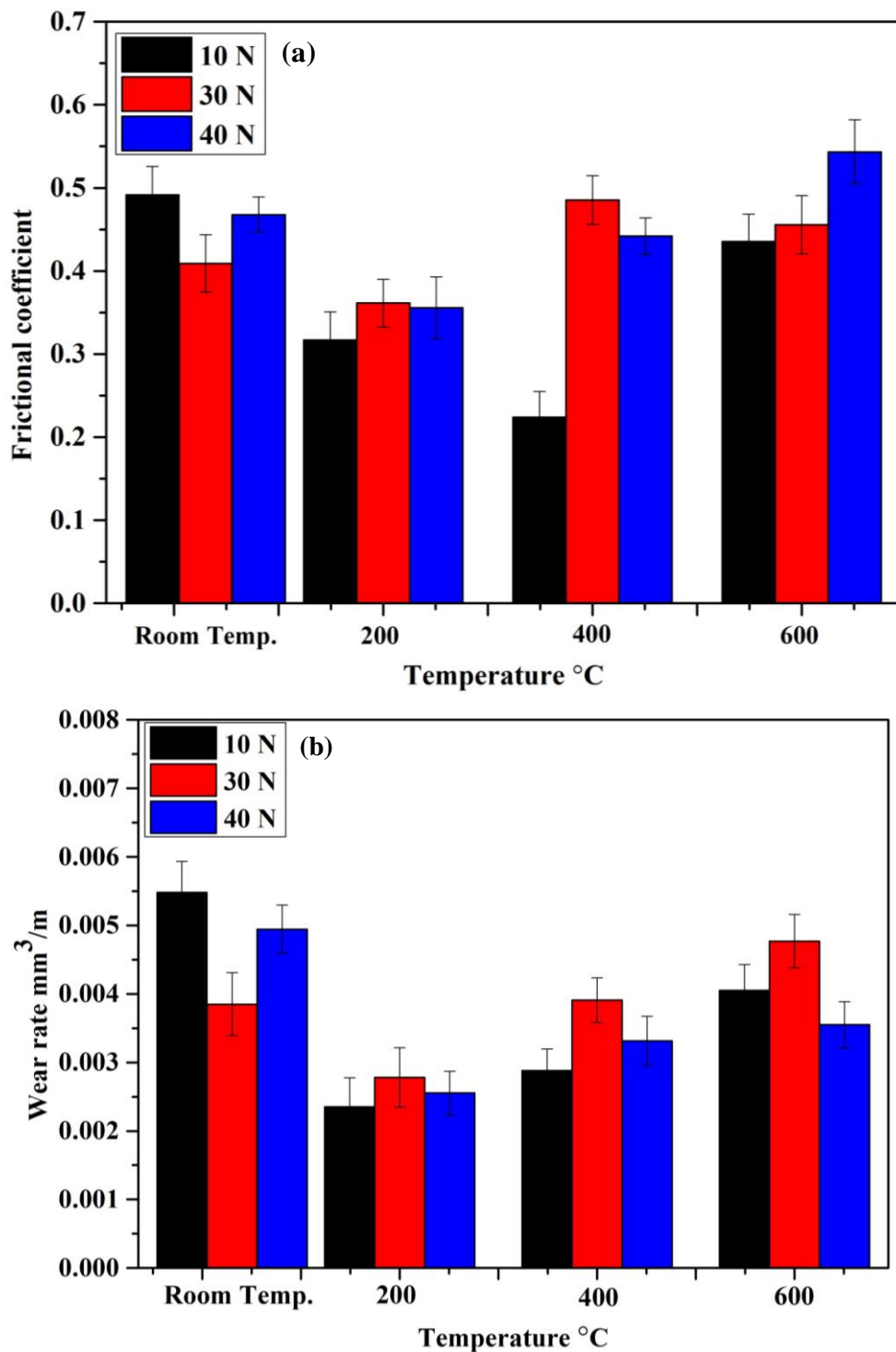


Figure 3.41 Frictional coefficient and wear rate of SS316L+WC-CrC-Ni with

(a) Frictional coefficient v/s Temperature (b) Wear rate v/s Temperature

intermetallic phases at elevated temperatures. From

Figure 3.40 it is observed that smaller peaks of  $Fe_3C_2$  are noticed at room temp. and 200 °C. Further, these peaks become strong at 600 °C implying lubrication at higher



temperatures by  $\text{Fe}_3\text{C}_2$ . New phases of  $\text{W}_2\text{C}$  and  $\text{WO}_3$  are observed at  $600^\circ\text{C}$  suggesting tungsten reaction with carbide and oxygen forming tungsten oxide responsible for low coefficient of friction and low wear rate at higher temperatures.

#### **3.10.2.4 Wear loss**

Figure 3.41 demonstrates the wear rate of SS316L+WC-CrC-Ni MIM specimen at room temperature 200, 400 and  $600^\circ$  with 10 30 and 40 N normal loads. The wear rate of the MIM specimen increased with increasing normal load. The wear rate at elevated temperature is lower than wear rate at room temperature. Lower wear rate at 200 and  $400^\circ\text{C}$  is due to the formation of the lubrication layer on the surface. At  $200^\circ\text{C}$ ,  $\text{MoO}_3$  acts as a lubricant as it is a low-temperature lubricant and forms the lubricating layer on the surface thereby reduces the wear rate. At  $600^\circ\text{C}$ , higher wear rate is observed due to the loss of lubricating property of Mo owing to its oxidation at a higher temperature and brittle form of solid lubricants ( $\text{MoO}_3$  and  $\text{MoNi}_4$ ). Also, the thin oxide layer of iron and chromium formed on the surface is not stable to impart wear resistance.

#### **3.10.3 Tool Steel**

##### **3.10.3.1 Frictional behaviour**

The friction coefficient of Tool steel MIM specimen is higher at the beginning of the wear test due to the high surface roughness of the contact surface with the rotating disc. It is uniform and constant after 500m of sliding distance. The behaviour of the friction coefficient is usually related to the origin of tribo-layers at the contact surface (Vergne et al.,2001). The variation of friction coefficient with a sliding distance at room temperature 200, 400 and  $600^\circ\text{C}$  is shown in Figure 3.42 to Figure 3.45. In order to understand the wear mechanisms of MIM specimen with different load and temperature, it is important to study the topography and microstructure of MIM specimen subjected to wear.

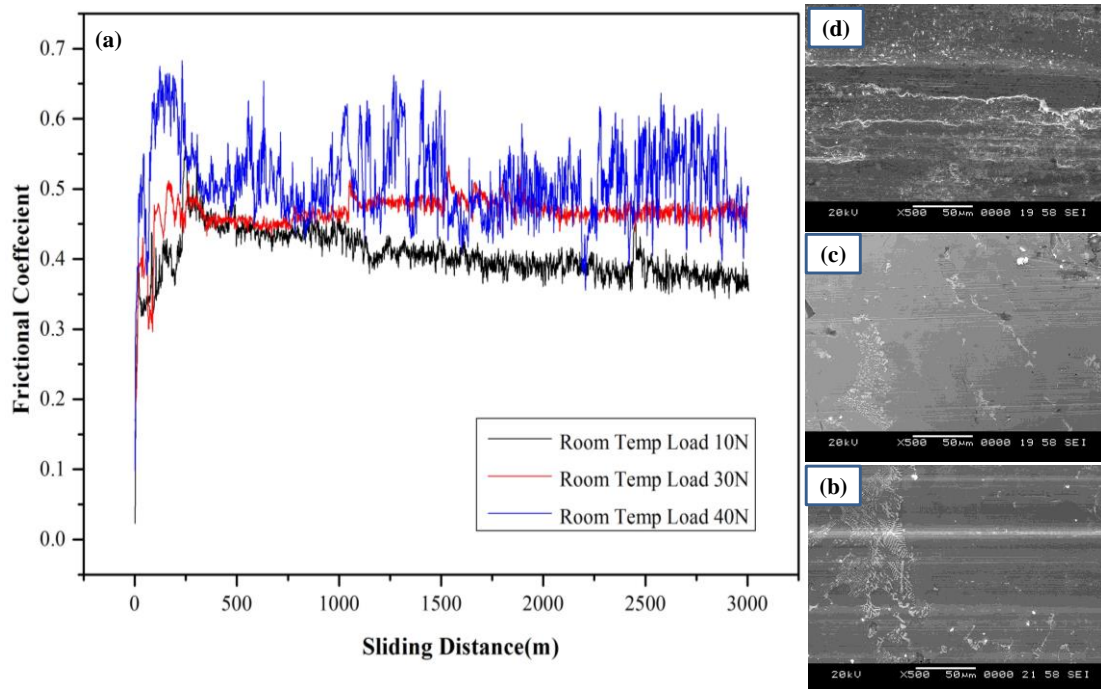


Figure 3.42 (a) Plot of friction coefficient with sliding distance at room temperature and SEM of worn surface of the Tool Steel specimen at room temperature under varying loads of (b) 10 N and (c) 30 N (d) 40 N

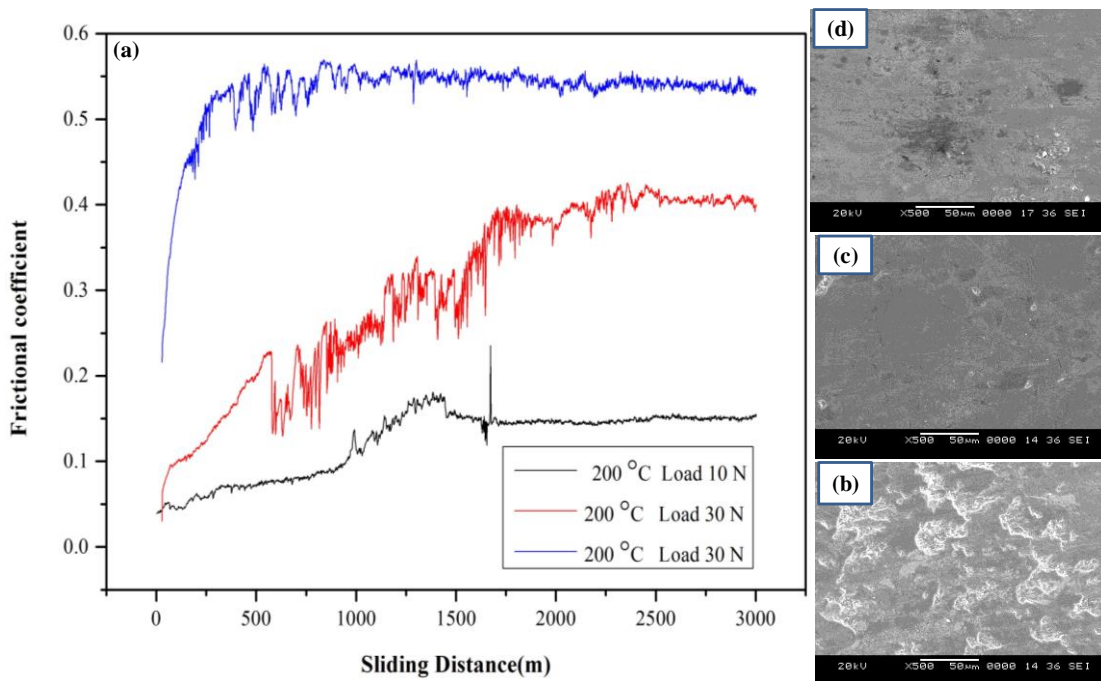


Figure 3.43 (a) Plot of friction coefficient with sliding distance at 200 °C and SEM of worn surface of the Tool Steel specimen at 200 °C under varying loads of (b) 10 N and (c) 30 N (d) 40 N

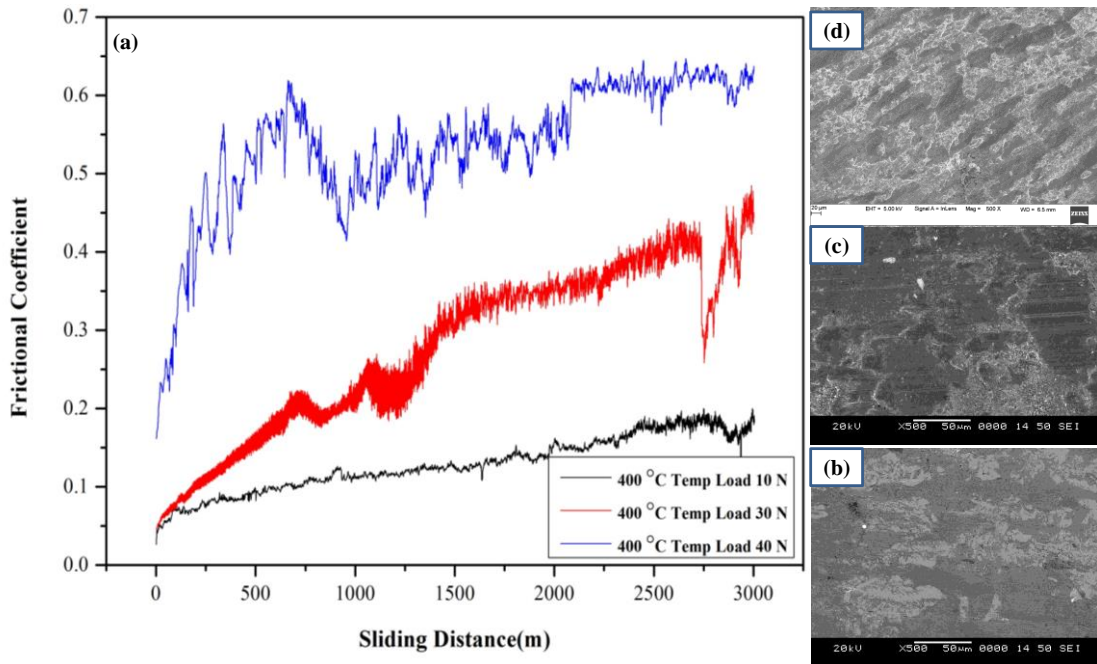


Figure 3.44 (a) Plot of friction coefficient with sliding distance at 400 °C and SEM of worn surface of the Tool Steel specimen at 400 °C under varying loads of (b) 10 N and (c) 30 N (d) 40 N

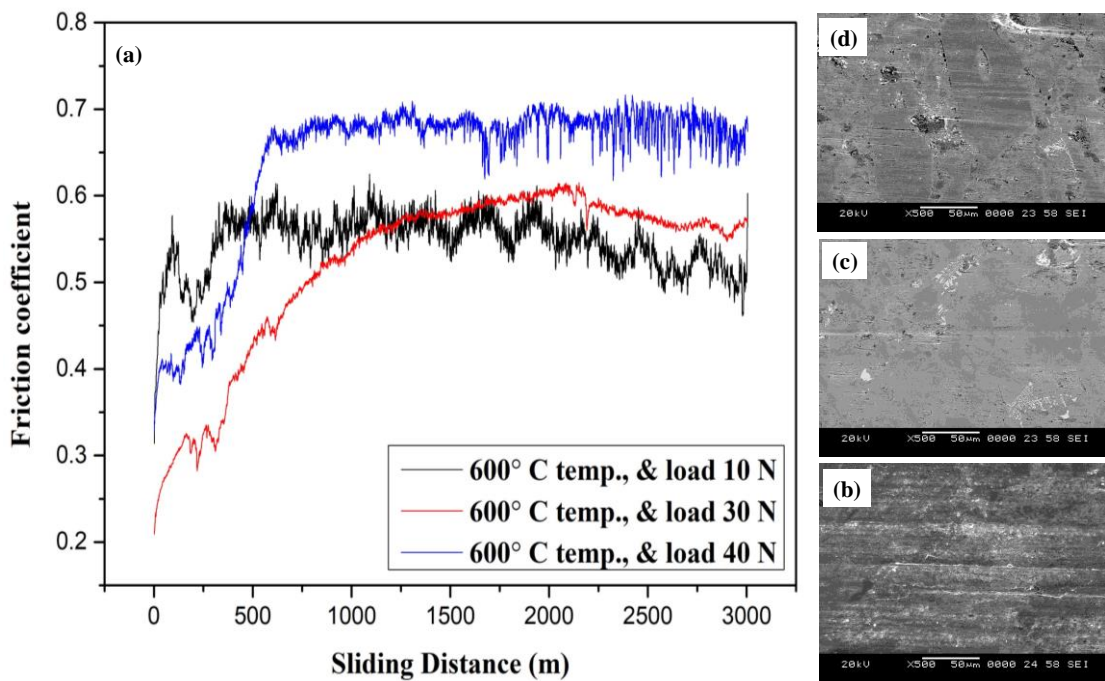


Figure 3.45 (a) Plot of friction coefficient with sliding distance at 600 °C and SEM of worn surface of the Tool Steel specimen at 600 °C under varying loads of (b) 10 N and (c) 30 N (d) 40 N

### 3.10.3.2 SEM Analysis

Figure 3.42 to Figure 3.45, demonstrates the worn surfaces of MIM specimens tested at a sliding speed of 3000 m at room temperature, 200 400 and 600 °C for 10, 30 and 40N loads. At higher temperature, MIM specimen leads to promote the formation of protective oxide films on the mating surfaces. Wear track on the MIM specimen has typical signs of adhesive interaction such as adhering to materials at higher load shown in Figure 3.42-Figure 3.45 (d). The Wear scars associated with the specimens presented different widths and the general appearances of the wear marks also varied. It seems that the wear volume was increased by the introduction of higher loads (Riahi et al.,2001; Venkataraman et al.,2000). Inside the wear scar, there is a clear evidence of abrasive wear, as evidenced by the presence of multiple parallel scratches. The intensity and number of scratches varied according to the normal load increased (Lim et al.,1987; Yuvaraja et al.,2009). MIM specimen has smooth surfaces and no signs of adhesion interaction or cracks observed at lower load.

### 3.10.3.3 XRD analysis

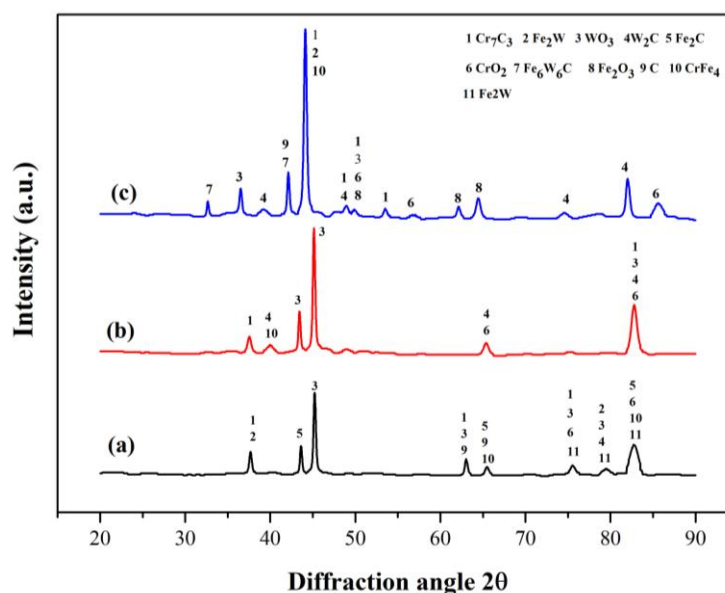


Figure 3.46 XRD pattern of worn out Tool Steel at a) room temperature, b) 400 and c) 600 °C.

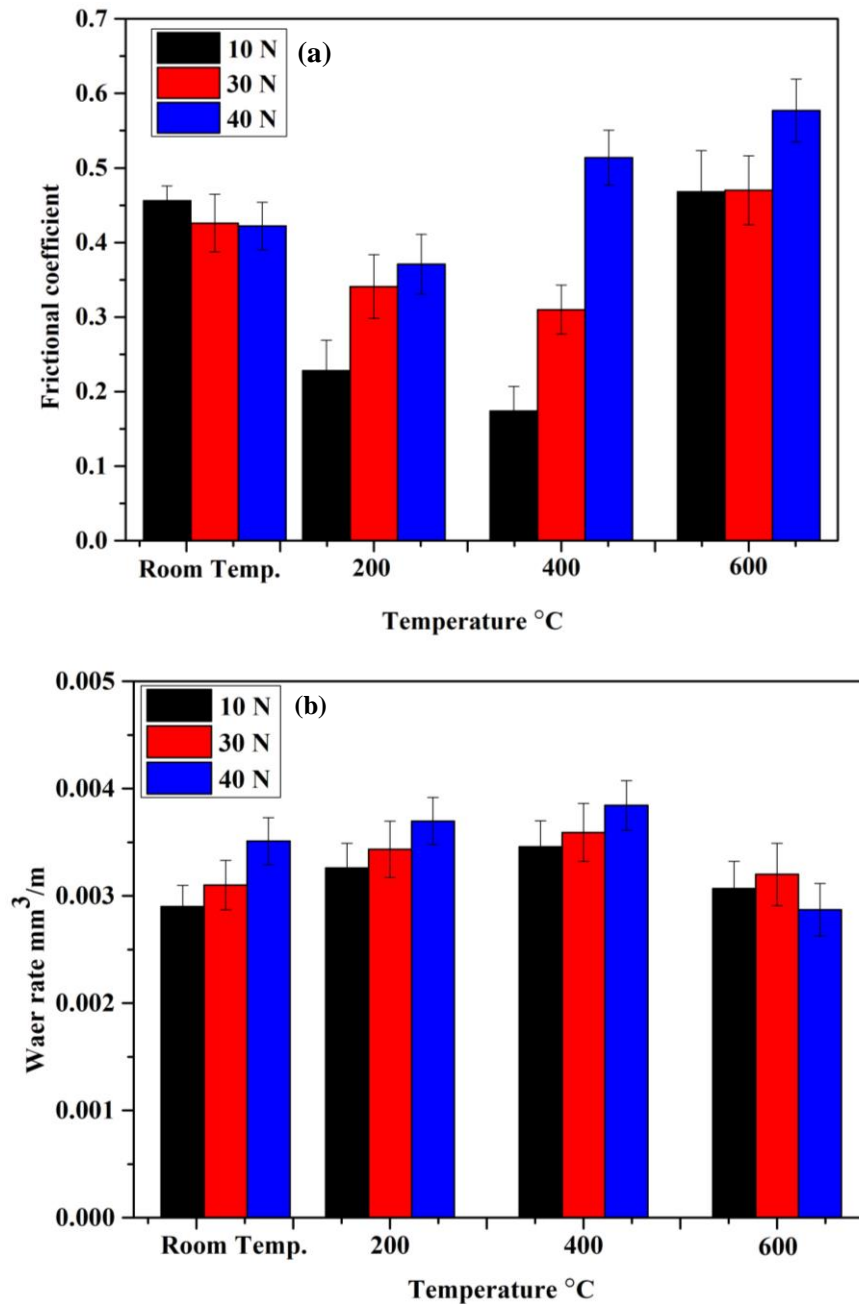


Figure 3.47 Frictional coefficient and wear rate of Tool steel with (a) Frictional coefficient v/s Temperature (b) Wear rate v/s Temperature

Figure 3.46 displays the XRD pattern of worn surfaces of Tool Steel MIM sample tested at room temp. 400 and 600 °C. The major peaks are indexed to  $\text{Cr}_7\text{C}_3$ ,  $\text{Fe}_2\text{W}$ ,  $\text{WO}_3$ ,  $\text{CrFe}_4$  and minor peaks are  $\text{Fe}_6\text{W}_6\text{C}$ ,  $\text{Fe}_2\text{O}_3$ ,  $\text{Fe}_2\text{C}$  and C. It is observed that distinct peaks of  $\text{Fe}_2\text{W}$  appear on the worn surfaces at room temp. At 600 °C, distinct  $\text{W}_2\text{C}$  peaks are observed along with new phases of  $\text{Fe}_6\text{W}_6\text{C}$  and  $\text{Fe}_2\text{O}_3$ . At elevated temperature, Iron

reacts with tungsten and oxygen leads to the formation of tungsten oxide which is responsible for the low coefficient of friction and low wear rate at higher temperatures.

### 3.10.3.4 Wear loss

Figure 3.47 (a & b) exhibits the Frictional coefficient and wear rates of Tool steel MIM specimen at room temperature, 200, 400 and 600 °C at 10, 30 and 40 N normal loads. It is observed that the wear rate of Tool steel MIM specimen is increased with increasing normal load from 10 to 40 N and decreased with increase in the temperature from 400 to 600 °C. Tool steel MIM specimen exhibited a lower wear rate at 600 °C and higher wear rate at 400 °C. At elevated temperature  $Fe_2O_3$  and  $Fe_2C_2$  get converted from brittle to ductile behaviour shearing easily on the contacting surface.

## 3.11 Oxidation Studies

### 3.11.1 Visual observations

Camera photographs of the  $Cr_3C_2$ -NiCr+NiCrSiB, SS316L+WC-CrC-Ni and Tool Steel MIM samples subjected to cyclic oxidation in air at 700 °C for 50 cycles are presented in Figure 3.48.

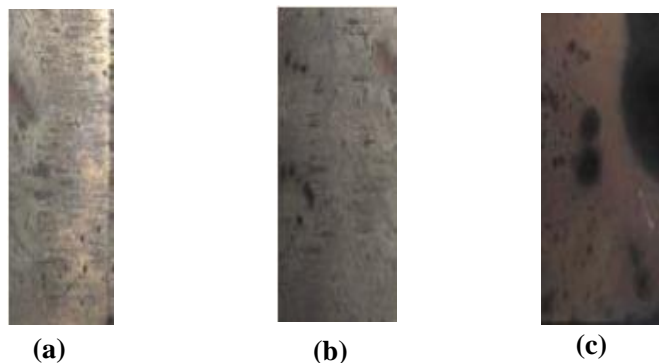


Figure 3.48 Camera photographs of a)  $Cr_3C_2$ -NiCr+NiCrSiB, b) SS316L+WC-CrC-Ni and c) Tool Steel MIM samples subjected to cyclic oxidation at 700 °C in air for 50 cycles.

At the end of the oxidation cycles, dark brown and reddish-brown colour oxide scale is noticed on the surface of  $\text{Cr}_3\text{C}_2\text{-NiCr+NiCrSiB}$ ,  $\text{SS316L+WC-CrC-Ni}$  and Tool Steel respectively. MIM samples are seen to be in good condition during the course of cyclic oxidation studies. The oxide scale is found to be compact, smooth and no spalling or cracks are seen.

### 3.11.2 Thermogravimetric behaviour

The plots of cumulative weight gain and weight gain square as a function of a number of cycles of  $\text{Cr}_3\text{C}_2\text{-NiCr+NiCrSiB}$ ,  $\text{SS316L+WC-CrC-Ni}$  and Tool Steel MIM samples are presented in a and b respectively.

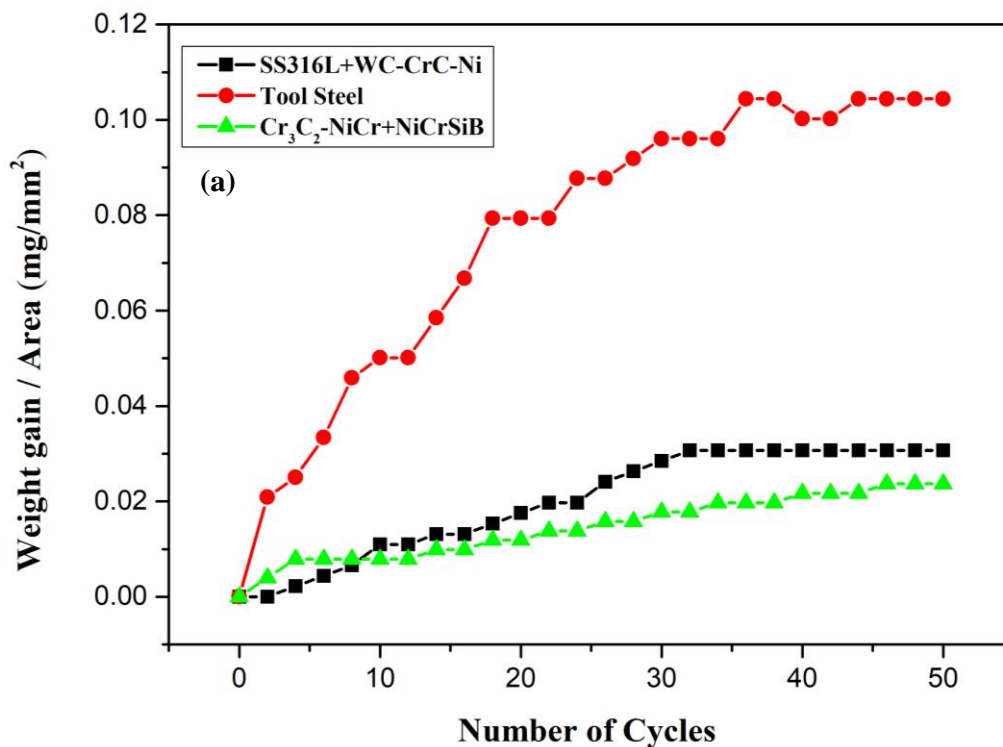


Figure 3.49 Plot of oxidation cycles (a) weight gain per unit area (b) square of weight gain per unit area.

The rapid increase in the weight gain is observed in the initial 30 cycles, thereafter a gradual increase in weight gain is observed for remaining cycles. The weight gain after 50 cycles for  $\text{Cr}_3\text{C}_2\text{-NiCr+NiCrSiB}$ ,  $\text{SS316L+WC-CrC-Ni}$  and Tool Steel MIM samples are 0.023, 0.030 and 0.104  $\text{mg/cm}^2$  respectively.

The Cr<sub>3</sub>C<sub>2</sub>-NiCr+NiCrSiB, SS316L+WC-CrC-Ni samples exhibited lower weight gain as compared to Tool steel owing to the formation of a protective oxide layer on the surface. Figure 3.50 shows the plot of weight gain square versus a number of cycles. The oxidation behaviour of MIM sample is parabolic in nature up to 50 cycles. Kinetics of oxidation is approximated by the parabolic rate law. The parabolic rate constant (Sahu et al. 2010) is calculated using the linear least square fit method in the form of :

$$\left(\frac{dW}{A}\right)^2 = K_p \times t \quad (4)$$

where  $dW/A$  is the weight gain per unit area,  $t$  is the oxidized time in seconds. The parabolic rate constants ( $K_p$  in  $10^{-14}g^2mm^{-4}s^{-1}$ ) for Cr<sub>3</sub>C<sub>2</sub>-NiCr+NiCrSiB, SS316L+WC-CrC-Ni and Tool Steel MIM sample is 0.333, 0.686 and 6.805 respectively.

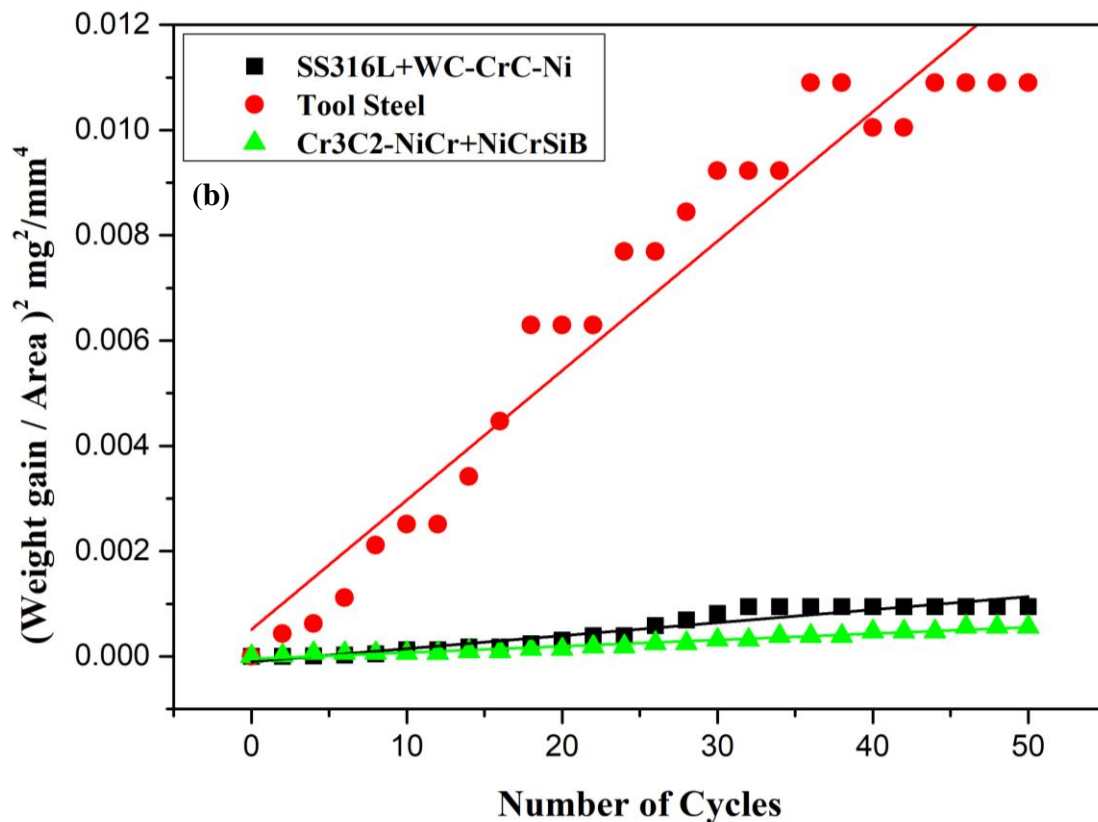


Figure 3.50 Plot of oxidation cycles (a) weight gain per unit area (b) square of weight gain per unit area.



### 3.11.3 XRD analysis

XRD pattern of  $\text{Cr}_3\text{C}_2\text{-NiCr+NiCrSiB}$ , MIM sample oxidized at  $700\text{ }^\circ\text{C}$  are shown in Figure 3.51. The major peaks correspond to  $\text{NiCrO}_4$ ,  $\text{B}_2\text{O}_3$ ,  $\text{CrBO}_3$ ,  $\text{NiSi}_2$  and  $\text{Cr}_3\text{C}_2$  while the intermediate peaks are indexed to  $\text{NiO}_2$ ,  $\text{NiSiO}_4$  and  $\text{Cr}_2\text{SiO}_4$  oxide formed protect the surface from further oxidation leading to parabolic weight gain. Figure 3.52 shows XRD pattern of  $\text{SS316L+WC-CrC-Ni}$  MIM sample oxidized at  $700\text{ }^\circ\text{C}$ . The major peaks correspond to  $\text{CrO}_2$ ,  $\text{Cr}$  and  $\text{W}_2\text{C}$  and minor phases  $\text{Cr}_3\text{C}_2$ ,  $\text{Fe}_3\text{O}_4$ ,  $\text{Cr}_3\text{Ni}_2$ ,  $\text{MoO}_3$ , and  $\text{NiO}_2$  oxide formed protect the surface from further oxidation leading to parabolic weight gain.

Figure 3.53 shows XRD pattern of Tool steel MIM sample oxidized at  $700\text{ }^\circ\text{C}$ . The major peaks correspond to  $\text{W}_2\text{C}$ ,  $\text{Fe}_3\text{O}_4$ ,  $\text{WO}_3$  and  $\text{CrO}_2$  and minor phases  $\text{Fe}_5\text{C}_2$  and  $\text{CrC}_2$ . However, many numbers of minor peaks indexed to  $\text{WO}_3$ , oxide formed protect the surface from further oxidation leading to parabolic weight gain.

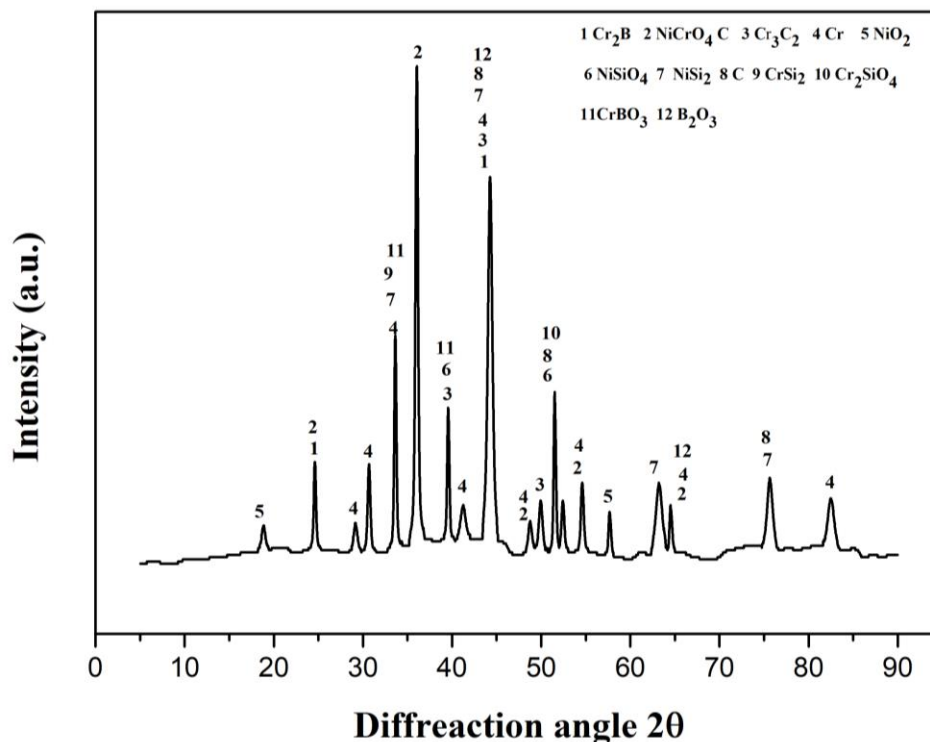


Figure 3.51 XRD pattern of  $\text{Cr}_3\text{C}_2\text{-NiCr+NiCrSiB}$  at  $700\text{ }^\circ\text{C}$ .

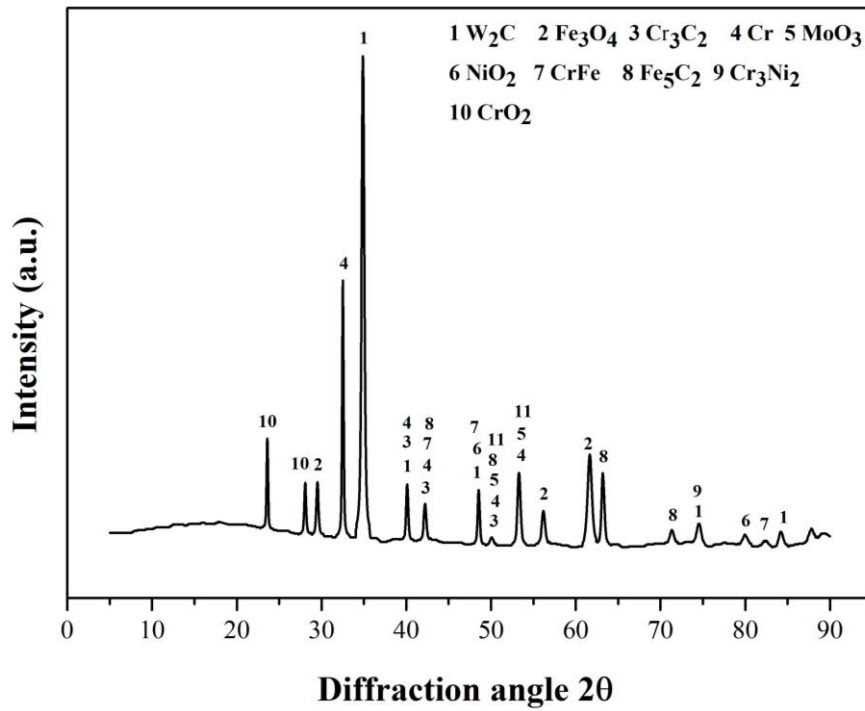


Figure 3.52 XRD pattern of SS316L+WC-CrC-Ni at 700 °C.

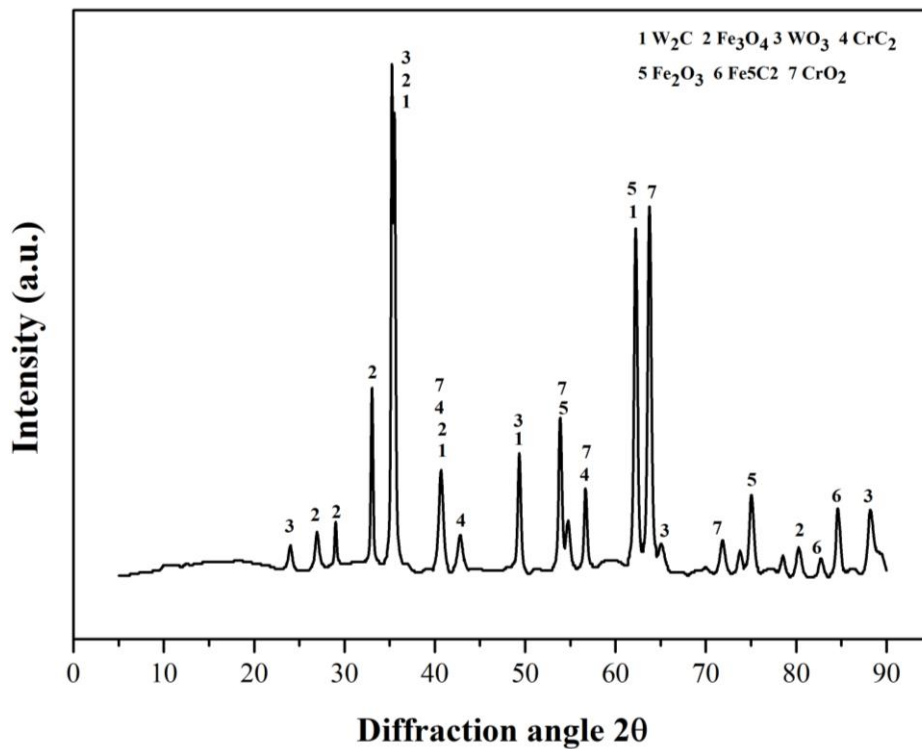


Figure 3.53 XRD pattern of Tool Steel MIM samples oxidized at 700 °C.

### 3.11.4 cross-sectional and Surface analysis of scale

The BSE image of MIM material system cross section subjected to 50 cycles of oxidation is shown in Figure 3.54. The micrographs (Figure 3.54 a-c) show that the MIM material system has retained their lamellar structure, with no obvious internal oxidation found on MIM samples.

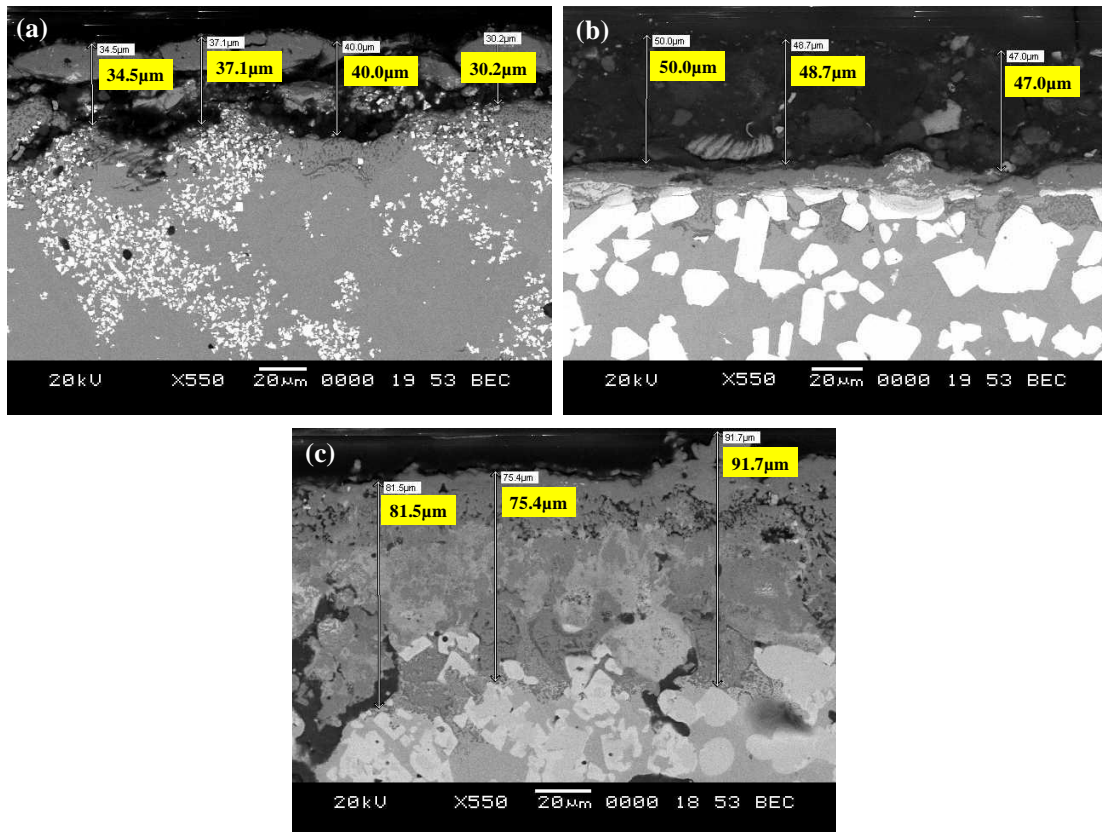


Figure 3.54 Oxidised MIM material system cross section a)  $\text{Cr}_3\text{C}_2\text{-NiCr+NiCrSiB}$  b)  $\text{SS316L+WC-CrC-Ni}$  c) Tool Steel

Compared with the Tool steel, thin and discontinuous oxide scale is observed on the  $\text{Cr}_3\text{C}_2\text{-NiCr+NiCrSiB}$ ,  $\text{SS316L+WC-CrC-Ni}$ . The subsurface not oxidised on MIM samples, an oxide layer formed prevent oxygen enter into the inside of MIM sample. Figure 3.55 shows the SEM micrographs with EDS analysis of  $\text{Cr}_3\text{C}_2\text{-NiCr+NiCrSiB}$ . EDS analysis depicts that the scale is mainly consisting of Fe, C, B, Si, Cr and O, implies the possibility of forming oxides of Fe, C, B, Si and Cr XRD results of oxidized MIM sample also confirms the existence of  $\text{NiCrO}_4$ ,  $\text{NiO}_2$ ,  $\text{Cr}_{15}\text{O}_2$  and  $\text{B}_2\text{O}_2$  oxides on the surface. The formed oxides restrict the penetration of oxygen into the MIM sample

by forming a protective oxide layer on the top surface. Hence only the top surface of the MIM sample has undergone oxidation increasing the oxidation resistance of the MIM sample surface.

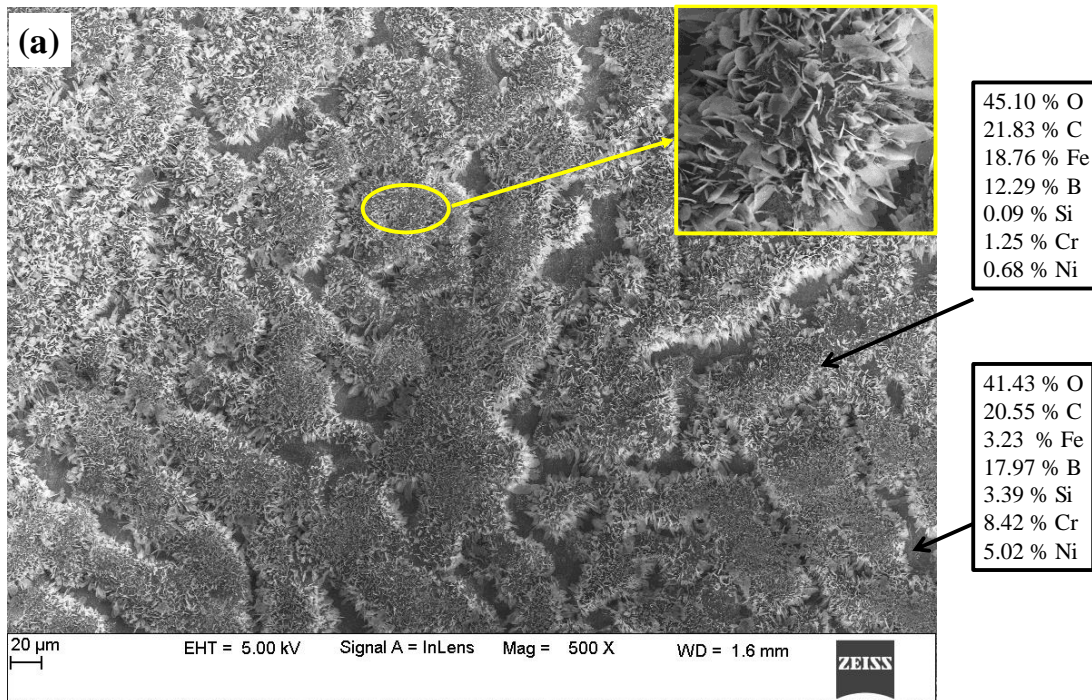


Figure 3.55 Surface morphology and EDS analysis of oxidized  $\text{Cr}_3\text{C}_2\text{-NiCr+NiCrSiB}$  MIM sample at 700 °C.

Surface elemental X-ray mapping of  $\text{Cr}_3\text{C}_2\text{-NiCr+NiCrSiB}$  MIM sample subjected to cyclic oxidation for 50 cycles is shown in Figure 3.56. X-ray mapping revealed that the topmost layer is rich in Ni, Cr, B and O indicates the formation of  $\text{NiO}_2$ ,  $\text{B}_2\text{O}_2$  and  $\text{Cr}_{15}\text{O}_2$  oxides. The oxide scale formed on the surface acts as a barrier to the inward diffusion of oxygen into the MIM Sample. The surface morphology of oxidized  $\text{Cr}_3\text{C}_2\text{-NiCr+NiCrSiB}$  MIM sample comprises of closely packed needle-like structure.

Figure 3.57 shows the SEM micrographs with EDS analysis of  $\text{SS316L+WC-CrC+Ni}$  MIM sample. EDS analysis of oxidized surface reveals the presence Ni, Cr, C, W, Fe and O as main constituents that denotes the presence of its oxides and spinels. XRD pattern (Figure 3.52) of oxidized  $\text{SS316L+WC-CrC+Ni}$  MIM sample also demonstrates the existence of  $\text{Fe}_3\text{O}_4$ ,  $\text{NiO}_2$ ,  $\text{CrO}_2$ , and  $\text{MoO}_3$ , oxides on the surface. The formed oxides restrict the penetration of oxygen into the MIM sample by forming a protective

oxide layer on the top surface. Hence only the top surface of the MIM sample has undergone oxidation increasing the oxidation resistance of the MIM sample.

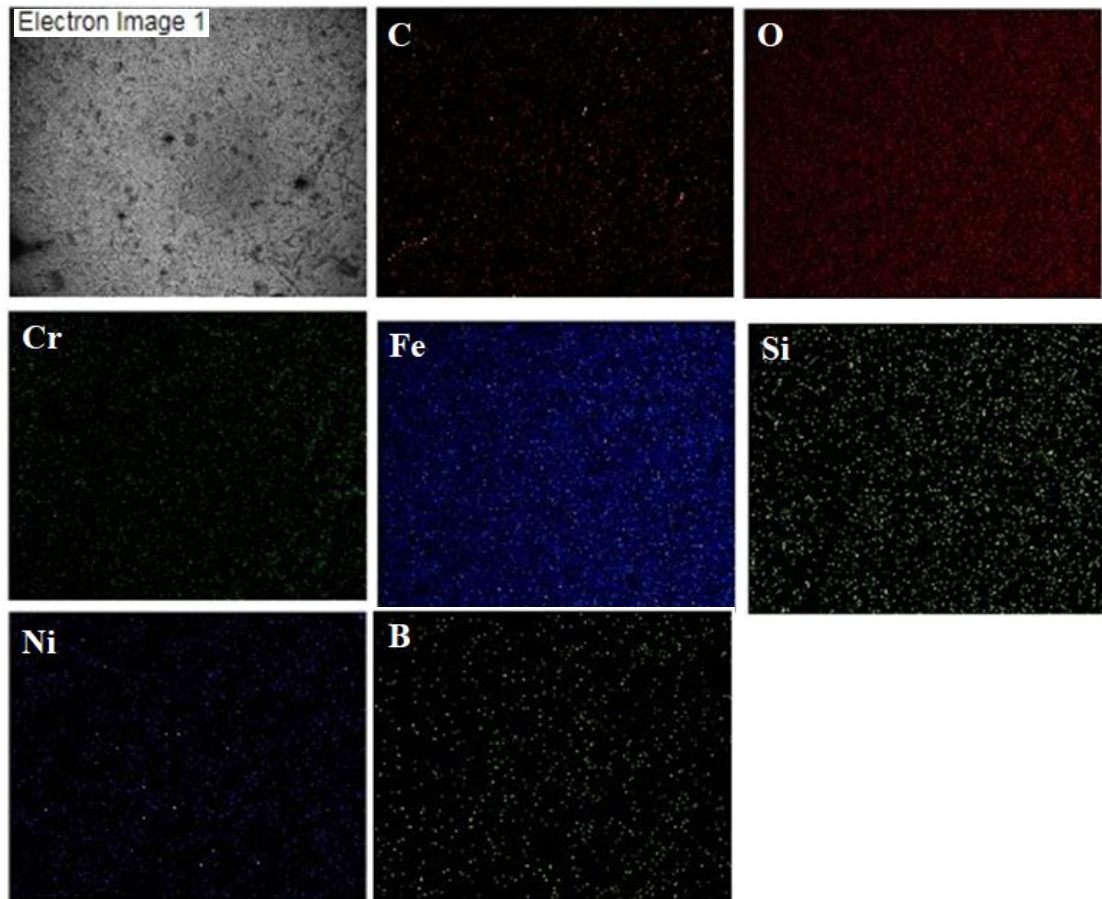


Figure 3.56 X-ray mapping of oxidized  $\text{Cr}_3\text{C}_2\text{-NiCr+NiCrSiB}$  at 700 °C.

Surface elemental X-ray mapping of SS316L+WC-CrC+Ni MIM sample subjected to cyclic oxidation for 50 cycles is presented in Figure 3.58. The surface morphology of oxidized SS316L+WC-CrC+Ni MIM sample comprises of closely packed flat needle-like structure.

X-ray mapping shows the distribution of O, Fe, Cr, Ni and W in the MIM samples. Dense oxygen is observed towards the top layer depicts the presence of oxides on the top layer.

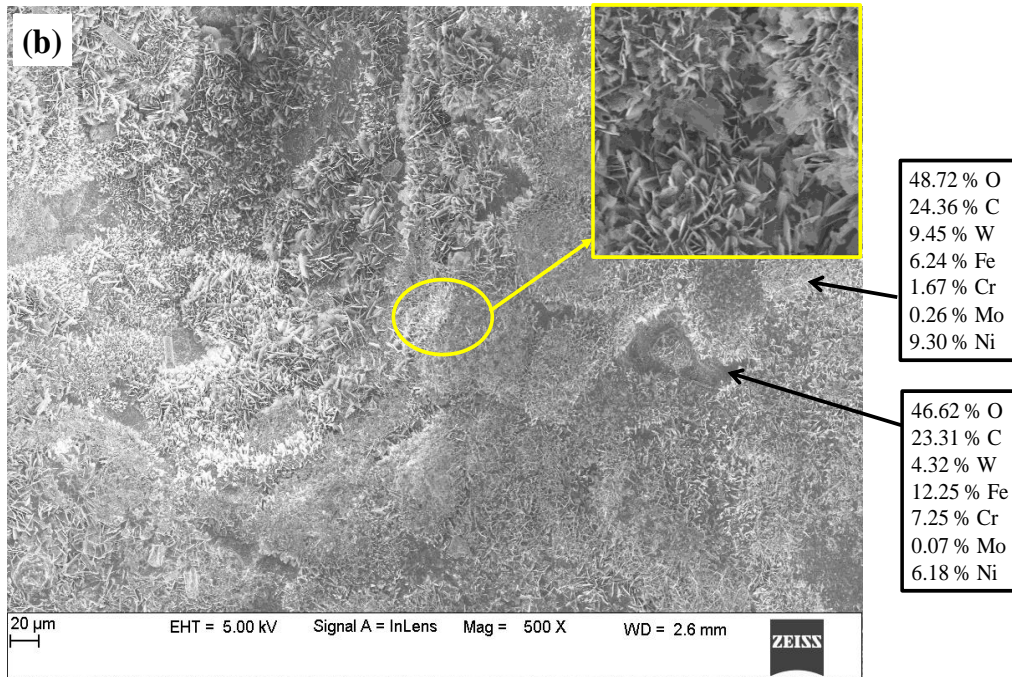


Figure 3.57 Micrograph of surface morphology and EDS analysis of oxidized SS316L+WC-CrC+Ni at 700 °C.

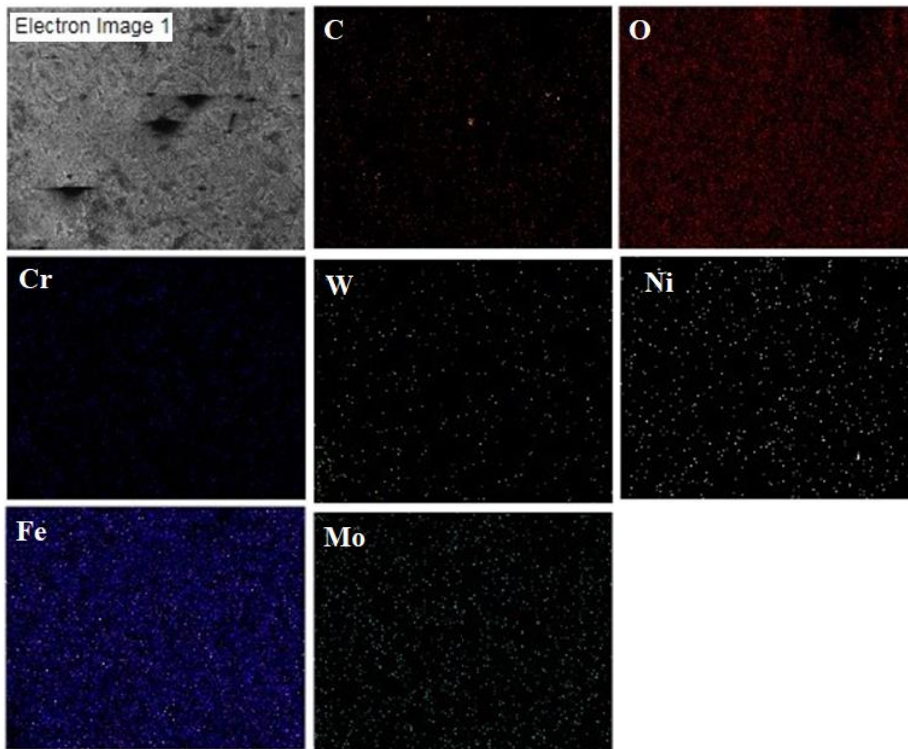


Figure 3.58 X-ray mapping of oxidized SS316L+WC-CrC+Ni at 700 °C.

Figure 3.59 shows the SEM micrographs with EDS analysis of Tool Steel. EDS analysis of oxidized surface reveals the presence C, V, Fe, Cr, and as main constituents that denotes the presence of its oxides and spinles. The surface morphology of oxidized MIM Tool steel sample comprises of the closely packed continuous globular structure. XRD pattern (

Figure 3.53) of the oxidized coating also demonstrates the existence of  $Fe_3O_4$ ,  $V_2O_5$ ,  $WO_3$  and  $CrO_2$  oxides on the surface. The formed oxides restrict the penetration of oxygen into the Tool Steel MIM sample by forming a protective oxide layer on the top surface. Hence only the top surface of the coating has undergone oxidation increasing the oxidation resistance of the Tool Steel MIM sample.

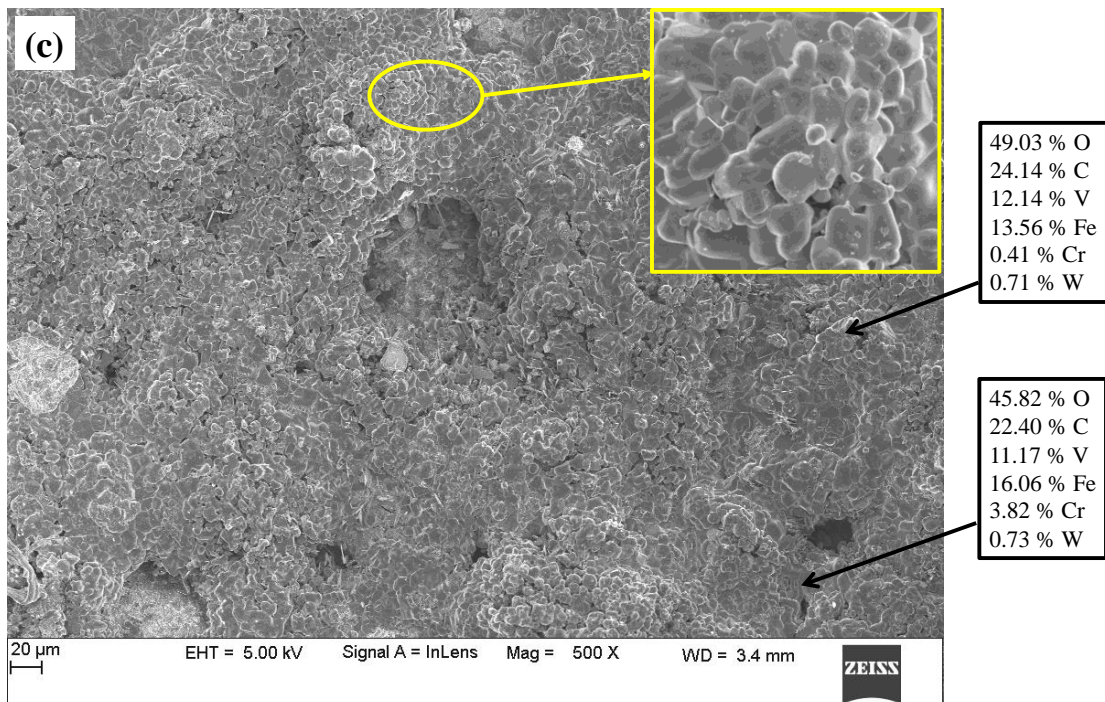


Figure 3.59 Micrograph of surface morphology and EDS analysis of oxidized Tool Steel at 700 °C.

Elemental X-ray mapping of Tool Steel MIM subjected to cyclic oxidation for 50 cycles is presented in Figure 3.60. X-ray mapping shows the distribution of O, Cr, and W in the Tool Steel MIM sample. Dense oxygen is observed towards the top layer depicts the presence of oxides on the top layer. Distribution of oxygen inside the Tool Steel

MIM sample is also observed which is due to  $\text{Fe}_3\text{O}_4$  (Maria et al. 2008) presence in the Tool Steel MIM sample.

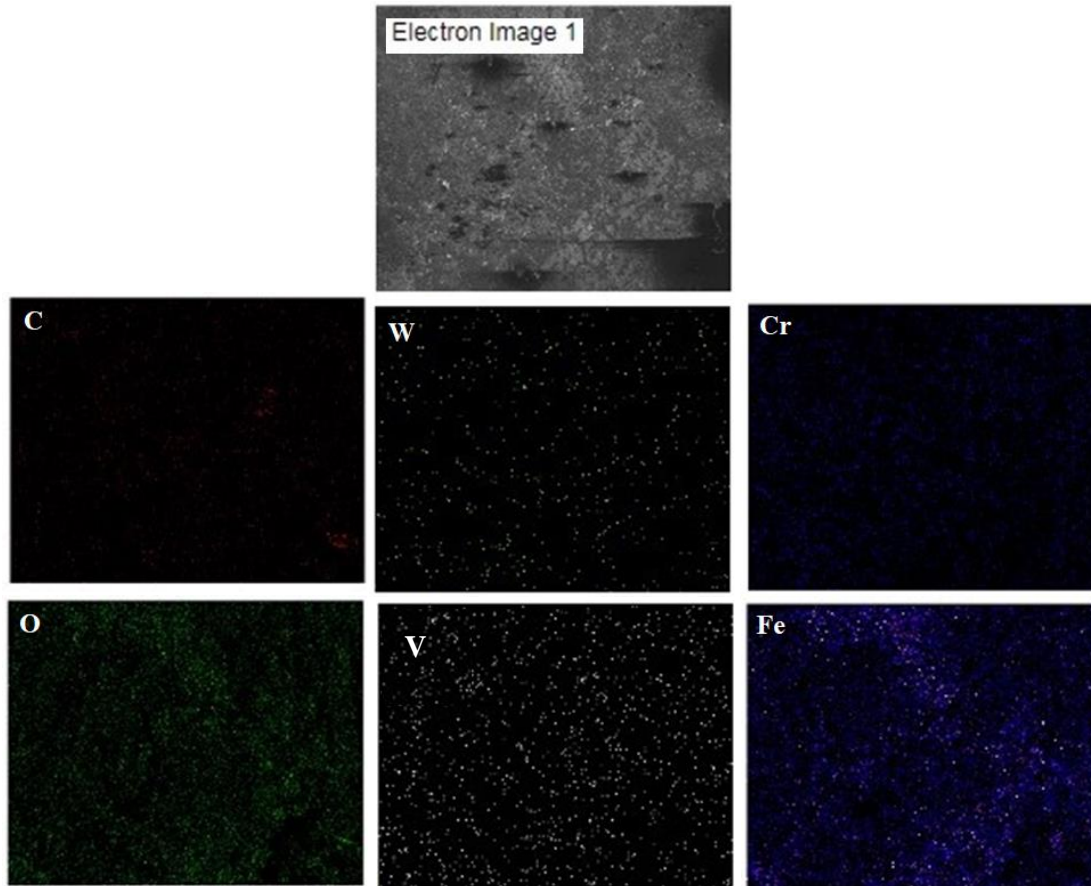


Figure 3.60 X-ray mapping of oxidized Tool Steel at 700 °C.

$\text{Cr}_3\text{C}_2\text{-NiCr+NiCrSiB}$  and  $\text{SS316L+WC-CrC-Ni}$  exhibited higher oxidation resistance as compared to Tool Steel. Protective thin oxide scale formed during oxidation imparted better oxidation resistance to the MIM samples. Based on the thermogravimetric data, the relative oxidation resistance of the Tool Steel and  $\text{Cr}_3\text{C}_2\text{-NiCr+NiCrSiB}$ , and  $\text{SS316L+WC-CrC-Ni}$  can be arranged in the following sequence:

$\text{Cr}_3\text{C}_2\text{-NiCr+NiCrSiB} > \text{SS316L+WC-CrC-Ni} > \text{Tool Steel}$ .

The better oxidation resistance of  $\text{Cr}_3\text{C}_2\text{-NiCr+NiCrSiB}$  is attributed to the superior oxidation resistance property of NiCrSiB matrix. Further, continuous and protective thin oxide scale consisting of oxides of Cr, Si and Ni and mixed spinel-type oxides of  $\text{NiSiO}_4$  increased the resistance to oxidation.



### **3.12 Summary**

The study aimed at the understanding of the effects of different Nickel and Iron based alloy contents on the microstructure and mechanical properties. Nickel and Iron based alloy with a porosity of less than 5% have been produced via the MIM process, and the shape of tensile test specimens was well preserved from the green state to the as-sintered state. The Nickel and Iron based alloy powders are fabricated by metal injection moulding showed a good combination of high temperature wear and oxidation resistance. It is thus feasible to use MIM to fabricate Nickel and Iron based alloy with excellent resistance to high temperature applications.



## CHAPTER 4

### 4 CONCLUSIONS

- Three types of materials systems  $\text{Cr}_3\text{C}_2\text{-NiCr+NiCrSiB}$ , SS316L+WC-CrC-Ni and Tool Steel T-15 was successfully developed and fabricated using MIM technique.
- The binders are successfully employed for defect-free metal injection moulding.
- A nickel and chromium-based feedstock achieved good homogeneity, thermal and rheological properties and defect free solvent debinding were done at 48 °C.
- Injection moulding parameters are optimized by several trails. Injection speed 41.4cc/s, injection time 3.7s and feedstock velocity 5.85m/s at injection temperatures 210, 220 and 230° C was adopted.
- The binder is removed in two stages: solvent debinding followed by thermal debinding. In solvent debinding, as the temperature of the solvent increases the rate of PEG 600, PW and SA removal increases but it is found that 48°C is the optimal temperature.
- From the viscosity measurement, it is found that the feedstock is shear thinning fluid i.e. as the shear strain rate increases viscosity decreases.  $\text{Cr}_3\text{C}_2\text{-NiCr+NiCrSiB}$  exhibits more viscosity among the selected feedstock, Tool steel T-15 feedstock shows the least viscosity within limits.
- The densification process was almost completed after one and a half hours at 1200 °C, reaching a density of Tool Steel 7.15 g/cm<sup>3</sup> with Vickers microhardness of 703 H<sub>v</sub>.
- Around 95 % of the theoretical density was achieved in sintering at 1200 °C with average UTS of 616 MPa. The shrinkage upon sintering varies between 11.8 to 13.84 % and this anisotropic shrinkage may be attributed to phase segregation.

- The density and microhardness of  $\text{Cr}_3\text{C}_2\text{-NiCr+NiCrSiB}$  is better than  $\text{SS316L+WC-CrC-Ni}$  and Tool Steel T-15
- The coefficients of friction for the composites were approximately dependent on the load and the temperature, the coefficients of friction increased with increasing load at a different temperature. And also wear rate due to adhesion is highest for the composite at a temperature of 400 °C for 40 N load, and lowest at room temperature for 10 N load. Wear rate scars increase gradually with increase in the tempering temperature, SEM analysis of wear tracks agrees with wear results
- $\text{Cr}_3\text{C}_2\text{-NiCr+NiCrSiB}$  and  $\text{SS316L+WC-CrC-Ni}$  exhibited higher oxidation resistance as compared to Tool Steel. The relative oxidation resistance of the MIM samples are in the sequence:  
 $\text{Cr}_3\text{C}_2\text{-NiCr+NiCrSiB} > \text{SS316L+WC-CrC-Ni} > \text{Tool Steel}$ .

## **FUTURE WORK**

It is strongly believed (by the author) that the newly developed thermal plastic-wax-based PEG-600, LDPE, PW, SA binder system has enormous potential for the injection moulding of metal and other powders and therefore further work should be carried out in applying this binder system for a full-scale production line.

Due to still long debinding times obtained during this work by the control of the heating rates further work should be conducted with the objective of reducing the debinding time of the PEG-600, LDPE, PW, SA binder system by the control of the rate of weight loss instead of the heating rates. This would require the use of a special binder-removal equipment

Further studies for improving the wetting characteristics of the PEG-600, LDPE, PW, SA binder system in contact with other powders such as silicon carbide, hard metal and alumina powders are believed to be of some value for providing a better mixing and moulding properties.

Further work in improving the powder characteristics such as particle size distribution is believed to be of some value for obtaining higher volume loadings and therefore higher sintered densities.

It is particularly felt necessary to improve the powder characteristics such as particle size distribution of each powder in order to achieve higher volume loadings within the wax-based PEG-600, LDPE, PW, SA binder system (without increasing the viscosity of the mixture) so that to obtain higher sintered densities and lower shrinkages.

Further optimization of the sintering conditions (temperature and time) is necessary for the injection moulded Tool Steel, carbide, hard metal and metallic powders so that to improve sintered densities and microstructures and therefore to obtain optimum mechanical properties.



## REFERENCES

- Abolhasani, H., and Muhamad, N. (2010). "A new starch-based binder for metal injection molding." *Journal of Materials Processing Technology*, Elsevier B.V., 210(6–7), 961–968.
- Aggarwal, G., Park, S. J., and Smid, I. (2006). "Development of niobium powder injection molding: Part I. Feedstock and injection molding." *International Journal of Refractory Metals and Hard Materials*, 24(3), 253–262.
- Agote, I., Odriozola, A., Gutierrez, M., Santamaria, A., Quintanilla, J., Coupelle, P., and Soares, J. (2001). "Rheological study of waste porcelain mixtures for injection molding." *Boletin De La Sociedad Espanola De Ceramica Y Vidrio*, 40(3), 195–200.
- Ahn, S., Park, S. J., Lee, S., Atre, S. V., and German, R. M. (2009). "Effect of powders and binders on material properties and molding parameters in iron and stainless steel powder injection molding process." *Powder Technology*, Elsevier B.V., 193(2), 162–169.
- Albolhasani, H., & Muhamad, N. (2009). "Rheological investigation of a starch based binder and feedstock for metal injection moulding." *International Journal of Mechanical and Materials Engineering*, 4(3)(294–299), 294–299.
- Almanar, I. P., Hussain, Z., and Omar, M. A. (2011). "Single step of binder thermal debinding and sintering of injection moulded 316L stainless steel." *Advanced Materials Research*, 155, 1518–1521.
- Atre, S. V., Park, S.-J., Zauner, R., and German, R. M. (2007). "Process simulation of powder injection moulding: identification of significant parameters during mould filling phase." *Powder Metallurgy*, 50(1), 76–85.
- Banhart, J. (2001). "Manufacture, characterization and application of cellular metals and metal foams." *Prog. Mater. Sci.*, 46, 559–632.
- Bilovol, B. V. V., and Kowalski, L. (2000). "Numerical Simulation of the Powder Injection Moulding Process for Optimization of Mould Design and Process Parameters ." *Advanced Engineering Materials*,(1438), 127–131.

Bilovol, V. V. (2003). *Mould filling simulations during powder injection moulding*. Ph.D. Thesis, Delft University of Technology, Delft, The Netherlands.

Bilovol, V. V., Kowalski, L., Duszczuk, J., and Katgerman, L. (2006). “The effect of constitutive description of PIM feedstock viscosity in numerical analysis of the powder injection moulding process.” *Journal of Materials Processing Technology*, 178(1–3), 194–199.

Chan, Y., White, J. L., and Oyanagi, Y. (1978). “Influence of glass fibers on the extrusion and injection molding characteristics of polyethylene and polystyrene melts.” *Polymer Engineering & Science*, 18(4), 268–272.

Daudt, N. de F., Bram, M., Barbosa, A. P. C., Laptev, A. M., and Alves, C. (2017). “Manufacturing of highly porous titanium by metal injection molding in combination with plasma treatment.” *Journal of Materials Processing Technology*, Elsevier B.V., 239, 202–209.

Davies, G. A., and Stokes, J. R. (2008). “Thin film and high shear rheology of multiphase complex fluids.” *Journal of Non-Newtonian Fluid Mechanics*, 148(1–3), 73–87.

Dehghan-Manshadi, A., Bermingham, M. J., Dargusch, M. S., StJohn, D. H., and Qian, M. (2017). “Metal injection moulding of titanium and titanium alloys: Challenges and recent development.” *Powder Technology*, Elsevier B.V., 319, 289–301.

Dimitri, C., Mohamed, S., Thierry, B., and Jean-Claude, G. (2017). “Influence of particle-size distribution and temperature on the rheological properties of highly concentrated Inconel feedstock alloy 718.” *Powder Technology*, Elsevier B.V., 322, 273–289.

Dobrzański, L. A., Matula, G., Herranz, G., Várez, A., Levenfeld, B., and Torralba, J. M. (2006). “Metal injection moulding of HS12-1-5-5 high-speed steel using a PW-HDPE based binder.” *Journal of Materials Processing Technology*, 175(1–3), 173–178.

Ferri, O. M. (2010). “Optimisation of Fatigue Behaviour of Ti-6Al-4V Alloy Components Fabricated by Metal Injection Moulding.” *Ph.D dissertation*, Belo Horizonte, Brasil .

Ferri, O. M., Ebel, T., and Bormann, R. (2009). “High cycle fatigue behaviour of Ti-6Al-4V fabricated by metal injection moulding technology.” *Materials Science and*



*Engineering A*, 504(1–2), 107–113.

Gelin, J. C., Barriere, T., and Song, J. (2010). “Processing Defects and Resulting Mechanical Properties After Metal Injection Molding.” *Journal of Engineering Materials and Technology*, 132(1), 011017.

Gerling, R., Aust, E., Limberg, W., Pfuff, M., and Schimansky, F. P. (2006). “Metal injection moulding of gamma titanium aluminide alloy powder.” *Materials Science and Engineering A*, 423(1–2), 262–268.

German, R. M. (1990). “Powder Injection Molding.” MPIF, Princeton, NJ.

German, R. M. (1993). “Technological barriers and opportunities in powder injection molding.” *International Journal of Powder Metallurgy*, 25(4):165-169

Gülsoy, H. Ö., and German, R. M. (2008). “Production of micro-porous austenitic stainless steel by powder injection molding.” *Scripta Materialia*, 58(4), 295–298.

Guoxin, H., Lixiang, Z., Yunliang, F., and Yanhong, L. (2008). “Fabrication of high porous NiTi shape memory alloy by metal injection molding.” *Journal of Materials Processing Technology*, 206(1–3), 395–399.

Hayat, M. D., Li, T., Wen, G., and Cao, P. (2015). “Suitability of PEG/PMMA-based metal injection moulding feedstock: an experimental study.” *International Journal of Advanced Manufacturing Technology*, 80(9–12), 1665–1671.

Heldele, R., Rath, S., Merz, L., Butzbach, R., Hagelstein, M., and Haußelt, J. (2006). “X-ray tomography of powder injection moulded micro parts using synchrotron radiation.” *Nuclear Instruments and Methods in Physics Research, Section B: Beam Interactions with Materials and Atoms*, 246(1), 211–216.

Ho, P. W., Li, Q. F., and Fuh, J. Y. H. (2008). “Evaluation of W-Cu metal matrix composites produced by powder injection molding and liquid infiltration.” *Materials Science and Engineering A*, 485(1–2), 657–663.

Huang, B., Liang, S., & Qu, X. (2003). “The rheology of metal injection moulding.” *Journal of Materials Processing Technology*, 137(1-3), 132–137.

- Huang, B., Fan, J., Liang, S., and Qu, X. (2003). "The rheological and sintering behavior of W – Ni – Fe nano-structured crystalline powder." *Milling*, 137, 177–182.
- Hwang, J., Choi, S., Hong, S., and Kim, N. (2013). "Determination of the flow stress and thermal properties of ceramic powder feedstock in ceramic injection molding." *Journal of Mechanical Science and Technology*, 27(6), 1815–1824.
- Ibrahim, M. H. I., Muhamad, N., and Sulong, A. B. (2009). "Rheological Investigation of Water Atomised Stainless Steel." *International Journal of Mechanical and Materials Engineering (IJMME)*, 4(1), 1–8.
- Ibrahim, M. H. I., Muhammad, N., Sulong, A. B., Jamaludin, K. R., Ahmat, S., and Nor, N. H. M. (2009). "Water Atomised Stainless Steel Powder for Micro Metal Injection Molding : Optimization of Rheological Properties." *Journal of Mechanical and Material Engineering*, c(December), 1–8.
- Ibrahim, M., and Muhamad, N. (2010). "Single performance optimization of micro metal injection molding for the highest green strength by using Taguchi method." *International Journal of Integrated Engineering*, 5(C), 35–44.
- IKEDA, S., SATOH, S., TSUNO, N., YOSHINOUCI, T., and SATAKE, M. (2014). "Development of Metal Injection Molding Process for Aircraft Engine Part Production." *IHI Engineering Review*, 47(1), 44–48.
- Imgrund, P., Rota, A., Petzoldt, F., and Simchi, A. (2007). "Manufacturing of multi-functional micro parts by two-component metal injection moulding." *International Journal of Advanced Manufacturing Technology*, 33(1–2), 176–186.
- Jamaludin, K. R., Muhamad, N., Nizam, M., Rahman, A., Amin, S. Y. M., Halim, M., Ibrahim, I., Hafiez, N., and Nor, M. (2009). "Moulding Parameter Optimisation for the Best Sintered Density." *Engineering*, I, 1–5.
- Janardhana Reddy, J., Ravi, N., and Vijayakumar, M. (2000). "A simple model for viscosity of powder injection moulding mixes with binder content above powder critical binder volume concentration." *Journal of the European Ceramic Society*, 20(12), 2183–2190.

- Jisa, R., Laumann, S., Cihak-Bayr, U., Tomastik, C., Eberle, R., Keppeler, M., Hofmann, U., and Franek, F. (2014). "Tribological properties of MIM manufactured copper alloys." *Tribology - Materials, Surfaces & Interfaces*, 8(1), 27–34.
- Kafkas, F., and Ebel, T. (2014). "Metallurgical and mechanical properties of Ti-24Nb-4Zr-8Sn alloy fabricated by metal injection molding." *Journal of Alloys and Compounds*, 617, 359–366.
- Kate, K. H., Enneti, R. K., Park, S. J., German, R. M., and Atre, S. V. (2014). "Predicting Powder-Polymer Mixture Properties for PIM Design." *Critical Reviews in Solid State and Materials Sciences*, 39(3), 197–214.
- Karatas, C., Sözen, A., Arcaklioglu, E., Ergüney, S. (2008). "Investigation of mouldability for feedstocks used powder injection moulding." *Materials and Design*, Elsevier B.V., 29 (2008) 1713–1724.
- Kaur, M., Singh, H., and Prakash, S. (2011). "Surface engineering analysis of detonation-gun sprayed Cr<sub>3</sub>C<sub>2</sub>-NiCr coating under high-temperature oxidation and oxidation-erosion environments." *Surface and Coatings Technology*, Elsevier B.V., 206(2–3), 530–541.
- Khairur, R. J., Norhamidi, M., Sufizar, A., Mohd, H. I. I., Nor, H. M. N., and Yusof, D. (2011). "Injection moulding temperature and powder loading influence to the metal injection moulding (MIM) green compact." *Scientific Research and Essays*, 6(21), 4532–4538.
- Khakbiz, M., Simchi, A., and Bagheri, R. (2005). "Analysis of the rheological behavior and stability of 316L stainless steel-TiC powder injection molding feedstock." *Materials Science and Engineering A*, 407(1–2), 105–113.
- Kim, J., Ahn, S., Atre, S. V., Park, S. J., Kang, T. G., and German, R. M. (2014). "Imbalance filling of multi-cavity tooling during powder injection molding." *Powder Technology*, Elsevier B.V., 257, 124–131.
- Kong, X. (2013). "powder feedstocks for micro-injection molding." Ph.D thesis, Université de Franche-Comté.
- Kong, X., Barriere, T., and Gelin, J. C. (2012). "Determination of critical and optimal

powder loadings for 316L fine stainless steel feedstocks for micro-powder injection molding.” *Journal of Materials Processing Technology*, Elsevier B.V., 212(11), 2173–2182.

Kuebler, J., and Blugan, G. (2011). “Failure analysis of zirconia ceramic watch bracelet components.” *Engineering Failure Analysis*, Elsevier Ltd, 18(2), 625–632.

Li, Y., Li, L., and Khalil, K. A. (2007). “Effect of powder loading on metal injection molding stainless steels.” *Journal of Materials Processing Technology*, 183(2–3), 432–439.

Li, Y., Lou, J., and Yue, J. (2005). “Analysis and evaluation of effects of processing steps on dimensional tolerance of PIM parts.” *J. Cent. South Univ. Technol.*, 12, 33–38.

Lim, S. C., Ashby, M. F., and Brunton, J. H. (1987). “Wear-rate transitions and their relationship to wear mechanisms.” *Acta Metallurgica*, 35(6), 1343–1348.

Liu, D.-M., and Tseng, W. J. (1998). “Influence of debinding rate, solid loading and binder formulation on the green microstructure and sintering behaviour of ceramic injection mouldings.” *Ceramics International*, 24(6), 471–481.

Liu, L., Loh, N. H., Tay, B. Y., Tor, S. B., Murakoshi, Y., and Maeda, R. (2005). “Mixing and characterisation of 316L stainless steel feedstock for micro powder injection molding.” *Materials Characterization*, 54(3), 230–238.

Liu, L., Loh, N. H., Tay, B. Y., Tor, S. B., Yin, H. Q., and Qu, X. H. (2011). “Investigation of final-stage sintering of various microsize structures prepared by micro powder injection molding.” *Applied Physics A: Materials Science and Processing*, 103(4), 1145–1151.

Liu, P. A., Zeng, L. K., and Li, X. Y. (2005). “Sintering products molded by injecting ceramic and metal powders.” *Journal of Central South University of Technology*, 12(3), 269–271.

LIU, X. quan, LI, Y. min, YUE, J. ling, and LUO, F. hua. (2008). “Deformation behavior and strength evolution of MIM compacts during thermal debinding.” *Transactions of Nonferrous Metals Society of China (English Edition)*, 18(2), 278–284.

Liu, Z. Y., Loh, N. H., Khor, K. A., and Tor, S. B. (2000). “Sintering of injection molded

M2 high -speed steel.” *Journal of Materials Processing Technology*, 32–38.

Liu, Z. Y., Loh, N. H., Tor, S. B., and Khor, K. A. (2003). “Characterization of powder injection molding feedstock.” *Materials Characterization*, 49(4), 313–320.

Loh, N. H., Tor, S. B., and Khor, K. A. (2001). “Production of metal matrix composite part by powder injection molding.” *Journal of Materials Processing Technology*, 108(3), 398–407.

Ma, J., Qin, M., Zhang, L., Tian, L., Li, R., Chen, P., and Qu, X. (2014). “Effect of ball milling on the rheology and particle characteristics of Fe-50%Ni powder injection molding feedstock.” *Journal of Alloys and Compounds*, Elsevier B.V., 590, 41–45.

Maria, S., Fernandes, D. C., Correa, O. V., and Ramanathan, L. V. (2008). “Oxidation and Erosion-Oxidation Behavior of Steels.” *Materials research*, 11(1), 43–46.

Martin, R., Vick, M., Enneti, R. K., and Atre, S. V. (2013). “Powder injection molding of ceria-stabilized, zirconia-toughened mullite parts for UAV engine components.” *Jom*, 65(11), 1388–1394.

Matula, G., Dobrzański, L. a, Várez, a, and Levenfeld, B. (2008). “Development of a feedstock formulation based on PP for MIM of carbides reinforced M2.” *Journal of Achievements in Materials and Manufacturing Engineering*, 27(2), 195–198.

Melli, V., Juszczak, M., Sandrini, E., Bolelli, G., Bonferroni, B., Lusvarghi, L., Cigada, A., Manfredini, T., and De Nardo, L. (2015). “Tribological and mechanical performance evaluation of metal prosthesis components manufactured via metal injection molding.” *Journal of Materials Science: Materials in Medicine*, 26(1), 1–11.

Meng, J., Loh, N. H., Fu, G., Tor, S. B., and Tay, B. Y. (2010). “Replication and characterization of 316L stainless steel micro-mixer by micro powder injection molding.” *Journal of Alloys and Compounds*, Elsevier B.V., 496(1–2), 293–299.

Mizerakova, S. (2013). “Online rheological characterization of highly filled polymer melts employed in powder injection moulding with the special regard to wall-slippage.” Master thesis ,*UTB ve Zlíne*.

Mori, K., and Osakada, K. (1997). “Finite element simulation of jetting behaviour in metal

injection molding using remeshing scheme.” *Finite Elements in Analysis and Design*, 25(3–4), 319–330.

Nor, N. H. M. M., Muhamad, N., Ihsan, A. K. A. M. A. M., and Jamaludin, K. R. (2013). “Sintering parameter optimization of Ti-6Al-4V metal injection molding for highest strength using palm stearin binder.” *Procedia Engineering*, Elsevier B.V., 68(February 2016), 359–364.

Nor, N. H. M., Muhamad, N., Ismail, M. H., Jamaludin, K. R., Ahmad, S., and Ibrahim, M. H. I. (2009). “Flow Behaviour To Determine the Defects of Green Part in Metal Injection Molding.” 4(1), 70–75.

Oh, I. H., Nomura, N., Masahashi, N., and Hanada, S. (2003). “Mechanical properties of porous titanium compacts prepared by powder sintering.” *Scripta Materialia*, 49(12), 1197–1202.

Onbattuvelli, V. P., Enneti, R. K., Park, S. J., and Atre, S. V. (2013). “The effects of nanoparticle addition on SiC and AlN powder-polymer mixtures: Packing and flow behavior.” *International Journal of Refractory Metals and Hard Materials*, Elsevier Ltd, 36, 183–190.

Pan-wei, S. H. O. (2009). “Based Metal Matrix Composites.” Ph.D thesis, National University of Singapore .

Porter, M. (2003). “Effects of binder systems for metal injection moulding.” M Tech Thesis, Luleå University of Technology.

Rajabi, J., Muhamad, N., Sulong, A. B., Fayyaz, A., and Wahi, A. (2012). “Jurnal Teknologi Full paper Advantages and Limitations of Using Nano Sized Powders for Powder Injection Molding Process : A Review.” *Jurnal Teknologi (Sciences and Engineering)*, 59, 137–140.

Riahi, A. ., and Alpas, A. . (2001). “The role of tribo-layers on the sliding wear behavior of graphitic aluminum matrix composites.” *Wear*, 251(1–12), 1396–1407.

Romano, P., Velasco, F. J., Torralba, J. M., and Candela, N. (2006). “Processing of M2 powder metallurgy high-speed steel by means of starch consolidation.” *Materials Science*

*and Engineering A*, 419(1–2), 1–7.

Sahu, S. P., Satapathy, A., Patnaik, A., Sreekumar, K. P., and Ananthapadmanabhan, P. V. (2010). “Development, characterization and erosion wear response of plasma sprayed fly ash-aluminum coatings.” *Materials and Design*, Elsevier Ltd, 31(3), 1165–1173.

Scott Weil, K., Nyberg, E., and Simmons, K. (2006). “A new binder for powder injection molding titanium and other reactive metals.” *Journal of Materials Processing Technology*, 176(1–3), 205–209.

Shahbudin, S. N. A., Othman, M. H., Amin, S. Y. M., and Ibrahim, M. H. I. (2017). “A Review of Metal Injection Molding- Process, Optimization, Defects and Microwave Sintering on WC-Co Cemented Carbide.” *IOP Conference Series: Materials Science and Engineering*, 226, 012162.

Shengjie, Y., Lam, Y. C., Yu, S. C. M., and Tam, K. C. (2002). “Thermal debinding modeling of mass transport and deformation in powder-injection molding compact.” *Metallurgical and Materials Transactions*, 33(3), 477–488.

Shengjie, Y., Li, Q. F., and Yong, M. S. (2006). “Method for determination of critical powder loading for powder-binder processing.” *Powder Metallurgy*, 49(3), 219–223.

Shibo, G., Xuanhui, Q., Xinbo, H., Ting, Z., and Bohua, D. (2006). “Powder injection molding of Ti-6Al-4V alloy.” *Journal of Materials Processing Technology*, 173(3), 310–314.

Shivashankar, T. S., Enneti, R. K., Park, S. J., German, R. M., and Atre, S. V. (2013). “The effects of material attributes on powder-binder separation phenomena in powder injection molding.” *Powder Technology*, Elsevier B.V., 243, 79–84.

Sidambe, A. T. (2014). “Biocompatibility of advanced manufactured titanium implants-A review.” *Materials*, 7(12), 8168–8188.

Sidambe, A. T., Figueroa, I. A., Hamilton, H., and Todd, I. (2010). “Metal injection moulding of Ti-64 components using a water soluble binder.” 4(4), 56–62.

Subuki, I. (2010). “Injection Moulding of 316L Stainless Steel Powder Using Palm Stearin Based Binder System.” (January), 228.

- Sulong, A. B., Ramli, M. I., Hau, S. L., Sahari, J., Muhamad, N., and Suherman, H. (2013). "Rheological and mechanical properties of carbon nanotube/Graphite/SS316L/polypropylene nanocomposite for a conductive polymer composite." *Composites Part B: Engineering*, Elsevier Ltd, 50, 54–61.
- Sun, L., Zhao, Q., Xiang, J., Shi, J., Wang, L., Hu, S., and Su, S. (2009). "Adsorption of NO and NH<sub>3</sub> over CuO/ $\gamma$ -Al<sub>2</sub>O<sub>3</sub> catalyst by DRIFTS." *Huagong Xuebao/CIESC Journal*, 60(2), 444–449.
- Suri, P., Atre, S. V., German, R. M., and de Souza, J. P. (2003). "Effect of mixing on the rheology and particle characteristics of tungsten-based powder injection molding feedstock." *Materials Science and Engineering A*, 356(1–2), 337–344.
- Suri, P., Koseski, R. P., and German, R. M. (2005). "Erratum: Microstructural evolution of injection molded gas- and water-atomized 316L stainless steel powder during sintering (Materials Science and Engineering A (10.1016/j.msea.2004.08.002))." *Materials Science and Engineering A*, 402(1–2), 341–348.
- Thavanayagam, G., Pickering, K. L., Swan, J. E., and Cao, P. (2014). "Analysis of rheological behaviour of titanium feedstocks formulated with a water-soluble binder system for powder injection moulding." *Powder Technology*, Elsevier B.V., 269, 227–232.
- Thavanayagam, G., and Swan, J. E. (2018). "Aqueous debinding of polyvinyl butyral based binder system for titanium metal injection moulding." *Powder Technology*, Elsevier B.V., 326, 402–410.
- Thian, E. S., Loh, N. H., Khor, K. A., and Tor, S. B. (2001). "Effects of debinding parameters on powder injection molded Ti-6Al-4V /HA composite parts." *Advanced Powder Technol*, Society of Powder Technology Japan, 12(3), 361–370.
- Thian, E. S., Loh, N. H., Khor, K. a, and Tor, S. B. (2002). "Ti-6Al-4V / HA composite feedstock for injection molding." *Materials Letters*, 56(October), 522–532.
- Tong, J., Yin, H., and Qu, X. (2009). "Factors affecting the replication quality of micro metal gears produced by  $\mu$ -PIM." *Microsyst Technol*, 16:391–397.



- Venkataraman, B., and Sundararajan, G. (2000). "Correlation between the characteristics of the mechanically mixed layer and wear behaviour of aluminium, Al-7075 alloy and Al-MMCs." *Wear*, 245(1–2), 22–38.
- Vergne, C., Boher, C., Levailant, C., and Gras, R. (2001). "Analysis of the friction and wear behavior of hot work tool scale: Application to the hot rolling process." *Wear*, 250–251, 322–333.
- Yang, W. W., Yang, K. Y., Wang, M. C., and Hon, M. H. (2003). "Solvent debinding mechanism for alumina injection molded compacts with water-soluble binders." *Ceramics International*, 29(7), 745–756.
- You, W. K., Choi, J. P., Yoon, S. M., and Lee, J. S. (2012). "Low temperature powder injection molding of iron micro-nano powder mixture." *Powder Technology*, Elsevier B.V., 228, 199–205.
- Yuvaraja, C., and Sharma, K. V. (2009). "A study of transition wear behavior of alumina particle reinforced Al-6061 MMCs." *Journal of Reinforced Plastics and Composites*, 28(23), 2903–2909.
- Zauner, R. (2006). "Micro powder injection moulding." *Microelectronic Engineering*, 83(4–9 SPEC. ISS.), 1442–1444.



## LIST OF PUBLICATIONS AND CONFERENCES

Sl. No.	Title of the paper	Authors (in the same order as in the paper. Underline the Research Scholar's name)	Name of the Journal/ Conference, Vol., No., Pages	Month, Year of Publication	Category *
1.	Evaluation of Wear Behaviour of Metal Injection Moulded Nickel Based Metal Matrix Composite	<u>Veeresh Nayak C.</u> , Ramesh M R, Vijay Desai, Sudip Kumar Samanta.	Silicon, (Springer Publication) p1-11	March 2018	1
2	Fabrication of stainless steel based composite by metal injection moulding	<u>Veeresh Nayak C.</u> , Ramesh M Vijay Desai, Sudip Kumar Samanta.	Materials Today; Proceedings (Elsevier Publication) Vol., 5, No.,2 P 6805-6814	April 2018	1
3	Evaluation of Mechanical Properties for Nickel Based Steel Produced By Metal Injection Moulding and Sintered Through Conventional and Microwave Method	<u>Veeresh Nayak C.</u> , Ramesh M R, Vijay Desai, Sudip Kumar Samanta.	Chemical Engineering Transactions (AIDIC Publication) Vol.,66.	July 2018	1
4	Manufacturing of Near Net Shape Tungsten Based Component By Metal Injection Moulding (MIM) Sintering	<u>Veeresh Nayak C.</u> , Ramesh M R, Vijay Desai, Sudip Kumar Samanta.	The Proceedings of the Institution of Mechanical Engineers, Part B: Journal of Engineering Manufacture (Sage Publication)	Nov 2018 (Accepted)	1

	with Conventional and Microwave Method.				
5	Evaluation of physical properties of WC-CrC- Ni reinforced stainless steel composite prepared by Metal Injection Molding	<u>Veeresh Nayak C,</u> Ramesh M R, Vijay Desai, Sudip Kumar Samanta.	6 <sup>th</sup> International Engineering Symposium, Kumamoto University Japan.	March 1-3 ,2017	3
6	Fabrication of stainless-steel based composite by metal injection moulding.	<u>Veeresh Nayak C,</u> Ramesh M R, Vijay Desai, Sudip Kumar Samanta.	International Conference on Emerging Trends in Materials and Manufacturing Engineering, NIT Trichy, Tamilnadu, India.	March 10-12, 2017	3
7	Evaluation of wear behaviour of metal injection moulded nickel base metal matrix composite	<u>Veeresh Nayak C,</u> Ramesh M R, Vijay Desai, Sudip Kumar Samanta.	The Porous and Powder Materials Symposium and Exhibitions 2017, Kusadasi Izmir –Turkey	September 12-15,2017.	3
8	Studies on Wear Characteristics of Metal Injection Molded T15 Tool Steel Part at Different Temperatures	<u>Veeresh Nayak C,</u> Ramesh M R, Vijay Desai, Sudip Kumar Samanta.	International Conference on Advances in Materials and Processing: Challenges and Opportunities. IIT–Roorkee	30 Nov-02 Dec, 2017.	4

9	Examination for high-temperature wear and oxidation proprieties of nickel-based metal matrix composite fabricated by metal injection moulding.	<u>Veeresh Nayak C,</u> Ramesh M R, Vijay Desai, Sudip Kumar Samanta.	International Conference on Composite Materials and Structures. IIT-Hyderabad,	27-29th December 2017	4
10	Optimization of Metal Injection Moulded Process using Taguchi, Grey relational and Principal Component Analysis	<u>Veeresh Nayak C,</u> Manjunath Patel G.C, Ramesh M R, Vijay Desai Sudip Kumar Samanta.	Springer Int Publishing, Cham-Switzerland Book Chapter (Full Chapter accepted)	2018	5

\*Category: 1: Journal paper, full paper reviewed 2: Journal paper, Abstract reviews 3: Conference/Symposium paper, full paper reviewed  
4: Conference/Symposium paper, abstract reviewed 5: Others (including papers in Workshops, NITK Research Bulletins, Short notes etc.)

**Veeresh Nayak C**  
Research Scholar  
Name & Signature, with Date

**Dr. Ramesh M R**  
Research Guide  
Name & Signature, with Date

**Dr. Vijay Desai**  
Research Guide  
Name & Signature, with Date



## BIO-DATA

**Name:** VEERESH NAYAK C

**Father's Name:** Bheemaraya Nayak C

**Date of Birth:** 01-06-1986

**Nationality:** Indian

**Marital Status:** Married

### Address:

#### Permanent Address

S/o. **Bheemaraya Nayak C**

Post :Gandhal (Panchamukhi)

Via: Gunjahalli, Taluk: Raichur

Dist: Raichur, Karnataka

India.

**Mobile Number:** +919916262180

#### Present Address

Department of Mechanical Engineering

National Institute of Technology Karnataka

Surathkal-575025, Srinivasanagar,

Mangalore, Karnataka, India.

**E-mail id:** veru29@gmail.com

### Educational Qualification:

Qualification	College/school	University/Board	Year of Passing
<b>Ph.D.</b> Mechanical Engineering	National Institute of Technology Karnataka	NITK,Surathkal	Pursuing
<b>M. Tech</b> Manufacturing Engineering	National Institute of Technology Karnataka	NITK,Surathkal	2013
<b>B. Tech.</b> Mechanical Engineering	P.A College of Engineering Mangalore	VTU	2009
<b>DIPLOMA</b> Diploma in Tool and Die Making	Govt. Tool Room and Training Centre Kudalasangama- Bagalkot	GT&TC Bangalore	2006
<b>SSLC</b>	Govt. Junior Technical School -Bagalkot	KSEEB	2002

**Publication Details**

<b>Papers Published</b>	<b>Under Review</b>	<b>Conference</b>	<b>Workshops/ Symposium</b>	<b>Awards and Recognitions</b>
4	1	5	15	<ul style="list-style-type: none"><li>• MHRD Scholarship for pursuing M.Tech and Ph.D.</li><li>• DST-SERB sponsored for attending an international conference held at Turkey</li><li>• GATE qualified in 2011 and 2012.</li></ul>

I declare that the above information is true and correct to best of my knowledge.

*(VEERESH NAYAK C)*